A Study of Thermal and Catalytic Pyrolysis of Centimeter-scale Biomass Particles

by

Yawei Chen

A dissertation submitted in partial fulfillment
of the requirements for the degree of
Doctor of Philosophy
(Mechanical Engineering)
in The University of Michigan
2018

Doctoral Committee:

Professor Arvind Atreya, Chair
Professor Johannes W. Schwank
Professor Angela Violi
Professor Margaret Wooldridge

Yawei Chen

yawei@umich.edu

ORCID iD: 0000-0003-0007-220X

ACKNOWLEDGEMENTS

I would like to express my sincere thanks to those who have helped me a lot in finishing this thesis.

First of all, I would like to specially thank my advisor, Professor Arvind Atreya, for giving me the opportunity to join his research group and providing me with continuous support, guidance, and inspiration on the research. He is passionate about research and education, and cares about his students. I am really grateful to him for providing everything to finish my Ph.D. degree.

I would also like to thank Professor Johannes Schwank, Professor Angela Violi, and Professor Margaret Wooldridge for serving on my committee and providing insightful comments and feedbacks in shaping this dissertation. Professor Wooldridge also shared the lab equipment to support the research, and I own her a debt of gratitude.

I am indebted to the help from Ms. Liza Atreya, Ms. Michelle Barnett, Professor Kevin Pipe, and Professor Katsuo Kurabayashi for their support and coordination while Professor Atreya was on the medical leave. I am also grateful to Professor Claus Borgnakke and I had a wonderful experience with him working on the IAC projects.

I would like to thank Weiyu Cao and Kumar Aanjaneya, who are great friends and colleagues, for their generous help on my research work. I will always miss the valuable discussions and the joyful moments we had in the office and the lab. You are the next in line for receiving Ph.D., and I wish you the best in the future. I appreciate the help from Dr. Cesar Barraza Botet for his training on the gas chromatography.

I also want to thank the previous lab mates, Dr. Insu Lee and Dr. Pawel Olszewski, for their kind help and guidance when I first joined the lab. Special thanks to Harald Eberhart, the best glass blower in the world. He not only made the perfect glass devices for my experiments, but also gave me a lot of encouragement to keep moving forward. I am grateful for all the great time that I have spent with Harald.

I have been very fortunate to have extremely supportive friends while pursuing my Ph.D. degree. In no order of preference, I would like to thank: Xinlin Song, for sharing the same apartment with me for 3 years and cooking great food that I will relish forever; Zida Li, for his limitless will to help and the great time together in the school and restaurants; Leyou Zhang, Yina Geng, Zhanjia Zhang, and many others. I will always cherish all the great moments we had together and all the help I have received from them.

Finally, I would like to thank my parents, my brothers and sisters, and my wife, Jingyue Xi, for their encouragements and understanding. My family's love has been an enormous source of support, without which this Ph.D. journey would not have been possible.

I also want to acknowledge the financial support from the National Science Foundation, the Department of Energy, and the Rackham Graduate School.

TABLE OF CONTENTS

LIST OF FIGURES

Figure

LIST OF TABLES

Table

LIST OF APPENDICES

Appendix

LIST OF ABBREVIATIONS

A_i	pre-exponential constant (s^{-1})
B	permeability (m^2)
C	specific heat (J /kg/K)
C_p	specific heat at cons. pres.(J /kg/K)
d	pore size (m)
e	emissivity
E_i	activation energy (J/mol/K)
f	focal length (m)
h	heat transfer coefficient ($W/m^2/K$)
k_i	reaction rate (s^{-1})
L_2	semi-major axis (m)
M	molecular weight (kg/mol)
P	pressure (Pa)
P_0	ambient pressure (101,300 Pa)
P_t	tar partial pressure (Pa)
P_g	gas partial pressure (Pa)
Q	heat generation (W/m^3)
R	univ. gas constant (8.314J/mol/K)
R_e	equivalent radius (m)
S	mass generation ($kg/m^3/s$)
SVR	surface area to volume ratio (m^{-1})
t	time (s)
t_{con}	pyrolysis conversion time (s)

T	temperature (K)
T_f	furnace temperature (K)
T_g	gas temperature (K)
V	flow velocity (m/s)
Y	solid mass fraction

Greek letters

α, β, η	spheroidal coordinate
ξ, ϕ, ω	spheroidal coordinate
ϵ	aspect ratio
ε	porosity
ν	degree or extent of pyrolysis
Δh	heat of pyrolysis(J/kg)
λ	thermal conductivity (W/m/K)
μ	viscosity (kg/m/s)
ρ	density (kg/m^3)
σ	Stefan's constant (5.67×10^{-8}W/m^2/K)

Subscripts

a	virgin solid
c, c_2	char char generation reaction
g, g_2	gas generation reaction
is	intermediate solid
s	surface
t	tar
v	volatiles
w	initial virgin solid

ABSTRACT

Finding renewable alternatives to fossil fuels is one of the most important challenges of the twenty-first century. In this context, biomass is an important source of renewable energy. This thesis concerns the pyrolysis of centimeter-scale biomass particles, a process that is a key step in the thermochemical conversion of biomass resources to biofuels.

Biomass particles commonly have irregular shapes and sizes, which are critical parameters affecting heat and mass transfer rates during the pyrolysis process. To investigate the pyrolysis behavior of biomass particles of various shapes and sizes, a mathematical model was introduced and numerically solved to simulate the complex physical and chemical reactions during biomass pyrolysis. Prolate and oblate ellipsoids were chosen to represent the biomass particles of arbitrary and irregular geometries. Numerical simulations were validated against relevant literature and experimental data. The effect of the particle shapes and sizes on the mass loss, center temperature, pyrolysis duration, and the product yields were investigated.

In this study, the bio-oil directly produced from the pyrolysis of centimeter-scale biomass particles contains a large number of oxygenated compounds and does not have any hydrocarbon compounds. In order to improve the bio-oil quality, both the pre-treatment of the biomass and post-treatment of the pyrolysis vapors were investigated respectively in a fixed-bed furnace reactor.

Torrefaction is the thermal treatment of biomass particle before they are pyrolyzed. To investigate the effect of torrefaction temperature and time on wood

pyrolysis, centimeter-scale pine wood particles were first torrefied at 225 °C, 250 °C, 275 °C, and 300 °C for 15 min, 25 min, and 35 min. Then the torrefied wood particles were used as the feedstock for pyrolysis. Pyrolysis yields of liquid, gas, and char were calculated and found to be affected by the torrefaction conditions. The temperature profiles in the center of the particles were measured and, both the endothermic and exothermic reactions were observed and explained. Chemical analysis of bio-oil obtained from torrefied wood showed that no hydrocarbon species were detected after torrefaction treatment.

Zeolite cracking is a post-treatment technique of the pyrolysis vapor in a high-temperature catalyst environment. Pine wood particles were pyrolyzed in a vertical tube furnace at 500 °C followed by the upgradation of pyrolysis vapors using zeolite ZSM-5 at catalyst temperatures of 400-600 °C (steps of 50 °C). The catalyst was later regenerated to recover its acidity and activity. Pyrolysis oil collected before and after catalysis was characterized by measuring the yield, the water content, and the chemical composition of its organic content. The pyrolysis oil before catalysis was homogeneous and highly oxygenated and neither aromatic nor polycyclic aromatic hydrocarbons (PAH) were detected. Upon catalytic treatment, the yield of bio-oil was markedly reduced from 56.32% to 43.69% (catalyst temperature: 400 °C), and it decreased with increasing catalyst temperature. The change of water content was very small for different catalytic pyrolysis cases. Chemical analysis of the bio-oil showed that aromatic hydrocarbons and PAH were formed in significant amounts upon catalytic treatment. The content of acids and ketones was reduced after catalysis. The overall effect of the usage of regenerated catalyst on the pyrolysis products was not significant in the current study.

CHAPTER I

Introduction

1.1 Background

As very aptly stated in the book by Gupta et al., the world is currently faced with two significant environmental problems: global warming and air pollution [1]. Both of these are related to the large-scale use of fossil fuels and exacerbated by the increasing global populations and energy consumption per capita. In this context, it is of great significance to find alternatives to fossil fuels.

Major alternatives of the fossil fuels include nuclear energy and renewable energy. Nuclear energy now contributes about 11% of the world's electricity from about 450 power reactors [2]. Nuclear energy does not produce CO_2, nevertheless, it is not expected to grow much due to safety concerns and high costs of construction, operation, and waste disposal. Renewable energy consists of hydropower, wind and solar energy, geothermal energy, ocean energy, biomass, etc. Biomass is one of the most important alternative energy sources, and the production of biofuels from biomass is considered to be sustainable since carbon is recycled through the nature.

About 29% of the U.S. energy consumption in 2016 was to fulfill transportation needs [3]. In the U.S., one of the primary problems is to produce liquid transportation fuels from sustainable resources and biomass-derived biofuels is the only sustainable source of liquid fuels [4]. It is true that liquid biofuels produced from biomass cannot

Table 1.1: Summary of currently used and potential forest and agriculture biomass at $60 per dry ton or less in the U.S. under high-yield scenario assumption (Million dry tons).

Feedstock	2012	2017	2022	2030
Forest resources currently used	129	182	210	226
Forest biomass & waste potential	97	98	100	102
Agricultural resources currently used	85	103	103	103
Agriculture biomass & waste potential	244	310	346	404
Energy crops	0	160	487	670
Total currently used	**214**	**284**	**312**	**328**
Total potential	**340**	**568**	**932**	**1176**
Total high-yield (3%)[1]	**555**	**852**	**1245**	**1504**

fully replace fossil fuels in the foreseeable future. However, it can contribute to reducing CO_2 emission, diversifying energy sources, creating new jobs, and improving the economies in the rural areas. In fact, the Energy Independence and Security Act of 2007 (EISA) mandated the use of renewable fuels to reach 36 billion gallons per year by 2022 [5].

Biomass is inexpensive and abundantly available in the U.S. According to a recent report by the Department of Energy, 852 million dry tons of non-food biomass were available from forest and agricultural resources in 2017 [5]. As shown in Table 1.1, the projected yield of biomass resources, including forest wastes, agricultural residues and the energy crops, even reaches a total of 1504 million dry tons by 2030.

Biomass is a highly oxygenated material and the structure and chemical composition of biomass are very different from that of coal. Although complex in nature, biomass mainly consists of cellulose (40 - 50%), hemicellulose (25 - 35%), and lignin (16 - 33%) [6]. Biomass also contains a small amount of inorganic minerals which ends up as the ash after burning and organic contents which can be extracted by using polar solvents.

Biomass can be treated via many strategies to produce liquid fuels. Depending

[1]Under the high-yield scenario, energy crops are shown for 3% annual increase in yield.

on the processing methods, these methods may be broadly categorized into thermal, biological or catalytic. Of these, biomass conversion to bio-oil through pyrolysis is the most appropriate for developing a compact reactor used in remote locations because it can directly produce a liquid fuel which can be readily stored and transported.

1.2 Biomass Pyrolysis

Pyrolysis is the thermochemical decomposition of materials at elevated temperatures in the absence of oxygen or air, leading to the production a large number of chemical compounds. The word is derived from Greek words *pyro* "fire" and *lysis* "decomposition". Biomass pyrolysis is a complex process and the exact pyrolysis mechanism is still not definitive, even though a lot of literatures are available on biomass pyrolysis. In general, it involves many simultaneous and successive physical processes such as heat transfer to increase particle temperature, moisture evaporation, and chemical reactions such as initiation of pyrolysis reactions to form volatiles and char, secondary decomposition of large volatile molecular, etc. Material properties such as specific heat capacity, heat conductivity, density, porosity, and permeability change with temperature and the extent of pyrolysis.

Depending on the operating conditions, such as the heating rate, process temperature, vapor residence time, biomass particle size, etc., pyrolysis can be controlled by either kinetics or heat transfer. Paulsen et al. studied the role of sample dimension and temperature in cellulose pyrolysis and introduced the pyrolysis number (Py) and Biot number (Bi) to describe the pyrolysis behavior of biomass particles under different conditions [7]. In their work, the pyrolysis number is defined as the ratio of timescales for pyrolysis reaction kinetics and heat transfer. For internal conductive heat transfer, the pyrolysis number is represented as $Py = \dfrac{\lambda}{\rho C_p L^2 k}$, where λ, ρ, C_p, L, and k are thermal conductivity, density, heat capacity, characteristic length scale, and reaction rate, for biomass pyrolysis respectively. The pyrolysis number with exter-

nal convection time scale is Py=$\frac{h}{\rho C_p L k}$, with h representing convective heat transfer coefficient between biomass and the surroundings. The Biot number is defined as the ratio of conduction and convection time scales, Bi=$\frac{hL}{\lambda}$, which can be used to distinguish thermally thick and thin biomass particles. A low Biot number indicates that internal temperature gradients can be ignored and the particle is isothermal, while a high Biot number means that non-trivial temperature gradient exist inside the particle.

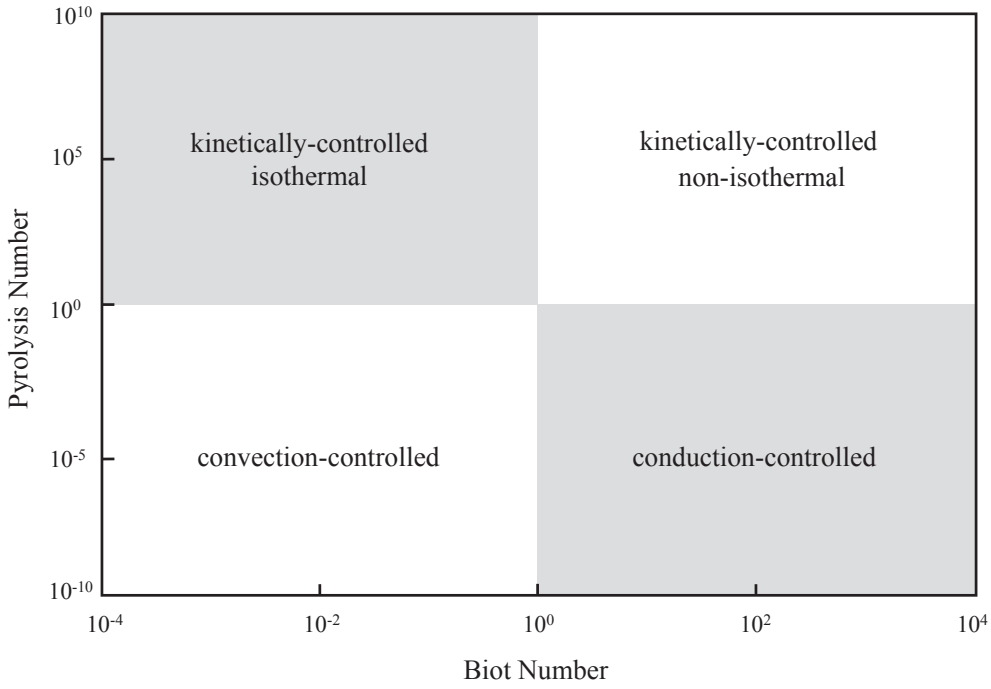

Figure 1.1: Reaction/transport map for biomass pyrolysis.

Figure 1.1 shows four pyrolysis zones based on the Pyrolysis and Biot number: a kinetically-controlled isothermal region where the temperature is uniformly distributed, a kinetically-controlled non-isothermal region where the biomass particle reaches the reaction temperature quickly with a significant temperature gradient, a convection-controlled region, and a conduction-controlled region. Finely ground biomass particles are commonly used in many fast pyrolysis reactors such as entrained flow reactors and fluidized-bed reactors to fulfill the requirements of rapid

heating and high mass transfer rates, resulting in kinetically controlled condition with a uniform temperature distribution in the entire particle [8]. Large particles are thermally thick and there is non-uniform temperature distribution during the pyrolysis process, leading to the condition where the process is mainly controlled by conduction or conduction and kinetics have comparable timescales.

Biomass is distributed over large and remote areas and it also has a low energy density. Besides, the cost of biomass harvesting and transportation from remote areas to a central processing facility is high and the transportation also contributes to green house gas emissions [9]. Reducing biomass particle size will increase the heat and mass transfer rates and reduce the secondary tar reactions, and thus most lab-scale studies on biomass pyrolysis have been carried out with particles in a narrow size range to fulfil the requirements of rapid heating. The particle sizes range from 200 μm for rotating cone reactors to 2 mm for fluidized beds [10]. Ablative reactors can take particles with sizes up to 20 mm, but it is not economically favorable due to its complex configuration [11]. On the other hand, experiments with mallee woody biomass concluded that there was a negligible effect of particle size on the yields of three lumped products (liquid, char, gas) after the size exceeds 1.5 mm [12]. A number of studies also suggest that bio-oil yield is not significantly affected by the particle size in a certain range [13, 14]. Considering that the size reduction of biomass particles becomes increasingly expensive as the size reduces due to the fibrous nature of biomass, reactors using large particles to achieve high yields and high quality of bio-oil would be advantageous.

1.3 Research Objectives and Thesis Outline

Clearly, the abundant biomass resources in Table 1.1 cannot be economically transported, dried, and ground to $\leq$2 mm in size. Thus, transportable, compact, energy-efficient, and inexpensive reactors must be developed to thermo-chemically process the

biomass on-site without finely grinding it. This thesis is a step toward this goal. The objectives of the research are to investigate the pyrolysis of centimeter-scale biomass particles by experiments and modeling to make biofuel a practical alternative.

Chapter I gives a brief introduction of biomass as an important source of renewable energy. It also talks about the pyrolysis principals and the limitations of currently available fast pyrolysis reactors. Objectives of the thesis are discussed.

Chapter II aims to investigate the pyrolysis of biomass particles of various shapes and sizes. In this chapter, two classes of shapes known as prolate and oblate ellipsoids are chosen to represent arbitrary and irregular geometries. A mathematical model of wood pyrolysis was introduced to describe the multiphase heat and mass transfer process in the porous media and a finite volume method based solver was developed to simulate the pyrolysis process. The numerical model was validated against experiments. Mass loss and center temperature profiles for different particles were presented and discussed. The effect of particle shapes and sizes on the pyrolysis duration and pyrolysis yields was explored based on the experimental and simulation results.

Chapter III investigates the effect of torrefaction on the pyrolysis of centimeter-scale pine wood particles. Experiments were conducted in a vertical tube furnace and the yields and compositions of bio-oil were measured. Biomass particles were torrefied at various temperatures and then used as feedstock for pyrolysis. The temperature in the center of the particle was measured using thermocouples and the mass loss rate of the biomass particle was also monitored during the pyrolysis process. The effect of torrefaction on the pyrolysis process was discussed.

Chapter IV studies catalytic cracking as an approach to deoxygenate bio-oil by passing bio-oil vapors through a zeolite catalyst bed at high temperature. A two-stage catalytic pyrolysis reactor was designed to evaluate the effect of catalyst temperature and regeneration on the pyrolysis products. The yields of liquid, gas, char, and coke were presented. The chemical composition of the organic phase in the bio-oil

was analyzed by GC-MS. The gaseous products were also collected and chemically analyzed.

Chapter V provides a summary of the thesis work. Recommendations for future work is also discussed.

CHAPTER II

Pyrolysis of Biomass Particles of Various Sizes and Shapes

2.1 Introduction

Basic knowledge of the pyrolysis behavior of centimeter-scale biomass particles is required for successful development of conversion processes and proper equipment design. The biomass feedstock is essentially a mixture of particles over a wide range of sizes and shapes, resulting in various particle surface area to volume ratios (SVR). SVR is critical for the heat and mass transfer inside the biomass particle, and ultimately affects the pyrolysis rate and pyrolysis products.

The influence of shapes and sizes of biomass particles on pyrolysis process and products has been investigated previously. Lu et al. [15] conducted an experimental and theoretical investigation by using three types of particles: flake-like, cylinder-like and near spherical. They concluded that both particle's shape and size affect the product yield, particle conversion time and mass loss rate etc. However, the number of particles shapes in this study is limited and not sufficient enough to cover all the possible geometries. Besides, the two-stage wood pyrolysis model does not predict the center temperature peak which is actually observed in experiments. Di Blasi et al. [13] studied the effect of particle size and density on the packed-bed pyrolysis of

wood, and they found that different physical properties of the samples affect the heat and mass transfer rate, and consequently affect the conversion time, but the effects on the yields and compositions of the lumped product classes are generally negligible. In this study, even though different sizes and shapes of particles were used, the overall shape remained unchanged since biomass particles were packed in a cylinder holder made of stainless steel mesh. Pious [16] investigated the effect of biomass size and aspect ratio on intra-particle tar decomposition during wood cylinder pyrolysis. The effect of particle shapes and sizes on the pyrolysis of biomass particles has also been studied by many other scholars both experimentally and theoretically [12, 17, 18, 19].

One of the most basic issues to be settled is: What should the geometry of the wood particles be for computations that would be representative of different shapes and enable correlating the experimental results? Baum and Atreya [20] developed a "quasi-steady" burning model in prolate and oblate coordinates to study the vaporization of solids. However, charring solids, which are practically more important, were not examined. Carmo and Lima [21] studied moisture diffusion inside oblate spheroidal solids. These studies indicate that prolate and oblate spheroids can be used to represent wood particles of various shapes and sizes. For aspect ratio (ϵ, the ratio of minor and major axes) equal to unity, both of the aforementioned ellipsoids represent spheres while for the limiting case of ($\epsilon \to 0$) the former reduces to a thin needle while the latter to a thin disk (see Figure 2.4). These smooth shapes are convenient for numerical computation and cover all possible particle shapes and SVR. It must be pointed out that these ellipsoids have smooth surfaces while wood particles found in forests are expected to have sharp and jagged edges. However, these edges are anticipated to be quickly pyrolyzed leaving behind smooth shapes for continued pyrolysis. The biggest advantage offered by these shapes is that only two parameters, namely L_2 (semi major axis) and ϵ determine the specific geometry. This results in a considerable simplification of the geometric description of infinitely different shapes

having varying degrees of irregularity while accounting for almost all possibilities.

2.2 Numerical Modeling

Biomass pyrolysis involves complex physical and chemical processes. To study the thermal and gravimetric behaviors of wood during pyrolysis process, many investigations of the reaction kinetics were conducted [22, 23, 24, 25]. One component models consider pyrolysis as a process of conversing wood to char, gas and tar. In multi-component models, the pyrolysis process is generally characterized by devolatilization of wood components, hemicellulose, cellulose and lignin. Park et al. [26] developed a multi-step model as schematically shown in Figure 2.1. This model is selected in current study because it accounts for the endo/exothermic behavior observed in the experiments and it also predicts the mass loss and temperature profiles very well. In this pyrolysis model, biomass decomposes to gas, tar, and intermediate solid. Tar experiences secondary decompositions into gas and char while the intermediate solid changes into char.

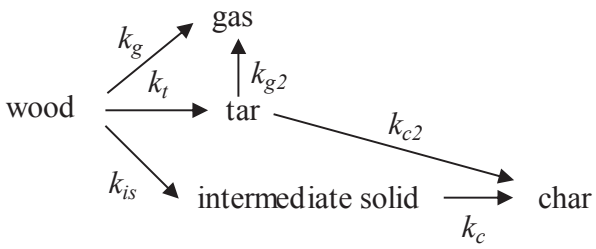

Figure 2.1: Reaction scheme for wood pyrolysis.

Major assumptions made in the mathematical model are:

- Volatiles and solid are in local thermal equilibrium, so the temperature and temperature gradients are the same for both.
- Shape of the charring solid remain constant during pyrolysis process, that is to say, there is particle shrinkage.

- Dry biomass particles are used, thus there is no water evaporation process.
- Volatile gases have ideal gas behavior.

2.2.1 Prolate and Oblate Spheroids

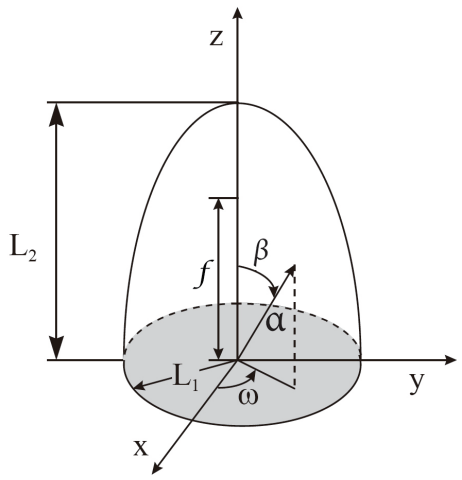

Figure 2.2: Characteristics of a prolate spheroid.

A prolate spheroid results from rotating a two-dimensional ellipse about the symmetry axis where foci are located (Figure 2.2). L_1 and L_2 are the lengths of the semi-major and semi-minor axes. α, β, and ω are three coordinate parameters. The prolate spheroidal coordinates are mapped to Cartesian coordinates through the following transformations [27].

$$\begin{aligned} x &= f \sinh\alpha \sin\beta \cos\omega \\ y &= f \sinh\alpha \sin\beta \sin\omega \\ z &= f \cosh\alpha \cos\beta \end{aligned} \tag{2.1}$$

where, f is the focal length, $0 \leq \alpha \leq \infty, 0 \leq \beta \leq \pi, 0 \leq \omega \leq 2\pi$. Surfaces of constant α form prolate spheroids while those of constant β generate hyperboloids of revolution.

By changing the coordinates with $\xi = \cosh\alpha, \eta = \cos\beta, \phi = \omega$, where, $1 \leq \xi \leq \infty, -1 \leq \eta \leq 1, 0 \leq \phi \leq 2\pi$, we have a new form of coordinate transformations which is easier to implement in numerical discretization.

$$\begin{aligned} x &= f\sqrt{(\xi^2-1)(1-\eta^2)}\cos\phi \\ y &= f\sqrt{(\xi^2-1)(1-\eta^2)}\sin\phi \\ z &= f\xi\eta \end{aligned} \tag{2.2}$$

The gradient operator is given by:

$$\vec{\nabla} = \frac{\hat{e}_\xi}{f}\sqrt{\frac{(\xi^2-1)}{(\xi^2-\eta^2)}}\frac{\partial}{\partial\xi} + \frac{\hat{e}_\eta}{f}\sqrt{\frac{(1-\eta^2)}{(\xi^2-\eta^2)}}\frac{\partial}{\partial\eta} + \frac{\hat{e}_\phi}{f\sqrt{(\xi^2-1)(1-\eta^2)}}\frac{\partial}{\partial\phi} \tag{2.3}$$

The divergence of a vector field $\vec{V}$ is

$$\begin{aligned} \vec{\nabla}\cdot\vec{V} = \frac{1}{f(\xi^2-\eta^2)}\Bigg[&\frac{\partial}{\partial\xi}\left(V_\xi\sqrt{(\xi^2-\eta^2)(\xi^2-1)}\right) \\ &+ \frac{\partial}{\partial\eta}\left(V_\eta\sqrt{(\xi^2-\eta^2)(1-\eta^2)}\right) \\ &+ \frac{\partial}{\partial\phi}\left(\frac{V_\phi(\xi^2-\eta^2)}{\sqrt{(\xi^2-1)(1-\eta^2)}}\right)\Bigg] \end{aligned} \tag{2.4}$$

The wood particle is assumed to be homogeneous and isotropic in this model, thus parameters are symmetric along the z-axis and the last term of Equation 2.3 and Equation 2.4 can be dropped. Details of oblate spheroid theory can be found in [27] and Appendix A.

The 3D illustration of prolate and oblate spheroids are shown in Figure 2.3. In 2D, prolate and oblate spheroids with various aspect ratio are demonstrated in Figure 2.4. As we can see, two parameters, which are semi-major axis (L_2) and aspect ratio ($\epsilon = L_1/L_2$), determine the specific geometry.

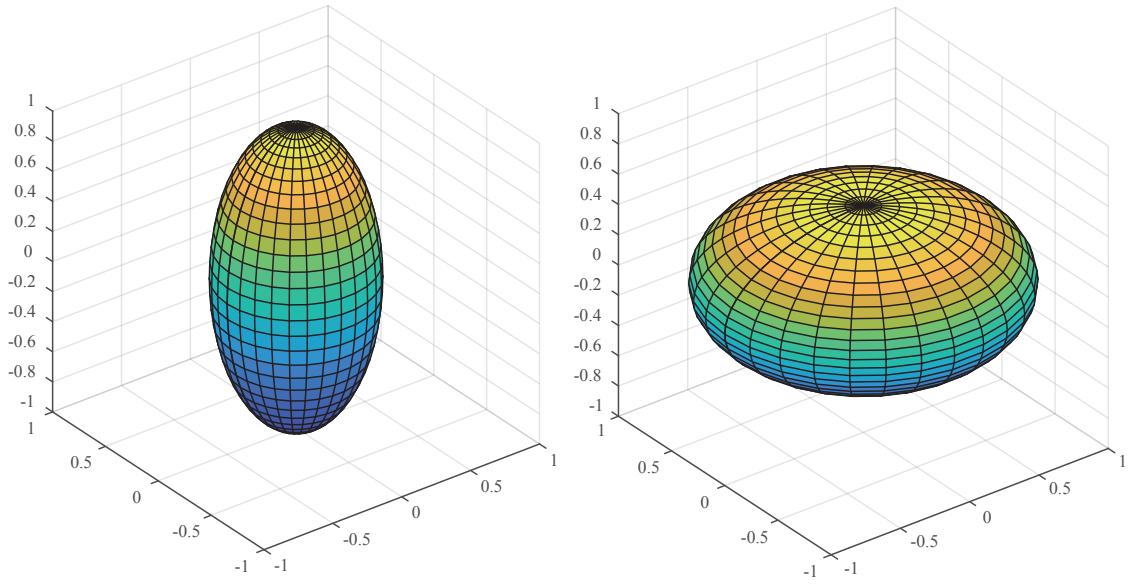

Figure 2.3: 3D illustration of prolate (left) and oblate spheroids (right).

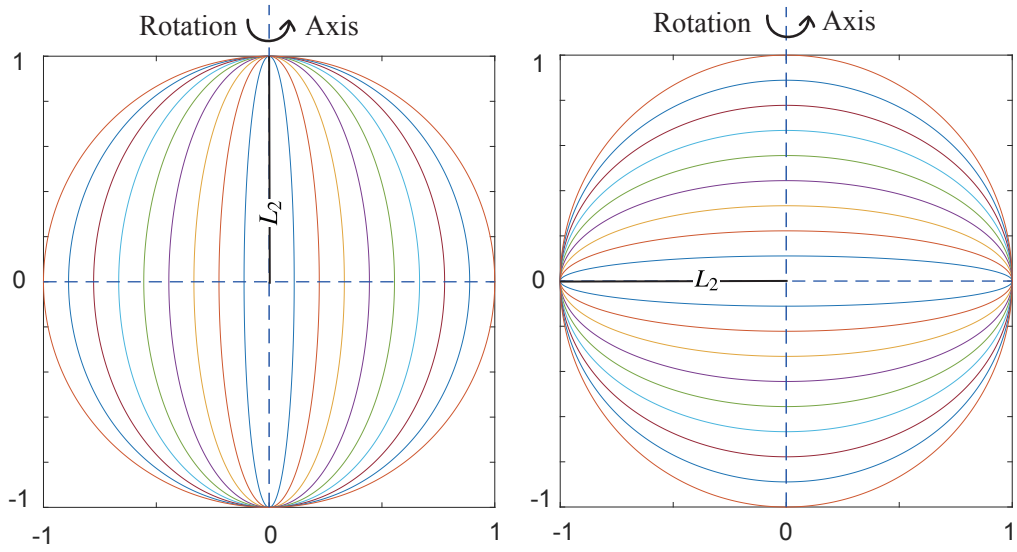

Figure 2.4: Prolate (left) and oblate spheroids (right) for different aspect ratios ϵ varying from 1/9 to 1. As $\epsilon \to 0$, the limiting case of a prolate is a needle while that of an oblate is a disc.

2.2.2 Conservation of Mass

The pyrolysis of virgin wood contains three consumption reactions which convert virgin wood to gas, tar and intermediate solids. Mass balances of these species are:

$$\frac{\partial \rho_a}{\partial t} = S_a = -(k_t + k_g + k_{is})\rho_a \tag{2.5}$$

$$\frac{\partial \rho_{is}}{\partial t} = S_{is} = k_{is}\rho_a - k_c\rho_{is} \tag{2.6}$$

$$\frac{\partial \rho_c}{\partial t} = S_c = k_c\rho_{is} + k_{c2}\rho_t \tag{2.7}$$

Reaction rate is assumed to follow the first-order Arrhenius equation as follows:

$$k_i = A_i \exp\left(-\frac{E_i}{RT}\right) \tag{2.8}$$

The gaseous flow inside the biomass particle takes place in the form of convection and diffusion. Convection is the flow under a pressure gradient and diffusion is driven by the concentration gradient. The diffusion process is difficult to model in details since multi-component diffusion occurs in the gas mixture during the pyrolysis process. To simplify the simulation, only convective mass flux is considered here since the effect of diffusion is negligible compared with convection [28].

Conservation of each gas phase component is expressed with terms representing mass change per unit volume, volatile flow through control volume boundaries and mass conversion in the volume due to pyrolysis reactions.

$$\frac{\partial(\varepsilon\rho_t)}{\partial t} + \vec{\nabla}\cdot\left(\vec{V}\rho_t\right) = S_t = k_t\rho_a - (k_{c2} + k_{g2})\rho_t \tag{2.9}$$

$$\frac{\partial(\varepsilon\rho_g)}{\partial t} + \vec{\nabla}\cdot\left(\vec{V}\rho_g\right) = S_g = k_g\rho_a + k_{g2}\rho_t \tag{2.10}$$

where, ε is the porosity calculated by $\varepsilon = 1 - \rho_s/\rho_w(1-\varepsilon_w)$. Here, ρ_s and ρ_w are the total solid and virgin wood densities, $\varepsilon_w = 0.4$ is the initial wood porosity [26].

The gaseous component flow velocity $\vec{V}$ is calculated by Darcy's law, which is an equation describing the a fluid flow through a porous medium. The law was originally formulated by Henry Darcy based on experimental results of water flow through sand, and later it was generalized to cover multiphase flow of water, oil, and gas in different porous media.

$$\vec{V} = -\frac{B}{\mu}\vec{\nabla}P \tag{2.11}$$

μ is the viscosity of volatiles. Permeability B is also needed for Darcy's law. It is a measure of the ability of a porous medium to allow fluid flows to pass through it. Permeability varies greatly during the pyrolysis process and the permeability is linearly interpolated between char and virgin wood weighted by the pyrolysis extent $\nu = 1 - (\rho_a + \rho_{is})/\rho_w$.

$$B = (1-\nu)B_w + \nu B_c \tag{2.12}$$

Total pressure is the sum of partial pressure of tar and gas which are assumed to be ideal gases.

$$P = P_t + P_g, \quad P_t = \frac{\rho_t RT}{M_t}, \quad P_g = \frac{\rho_g RT}{M_g} \tag{2.13}$$

where, M_t and M_g are molecular weights of tar and gas, R is universal gas constant.

Combining Equation 2.9 - Equation 2.13 gives the total gas-phase continuity equation including tar and gas.

$$\frac{\partial}{\partial t}\left(\frac{\varepsilon P}{T}\right) = \vec{\nabla}\cdot\left(\frac{BP}{\mu T}\vec{\nabla}P\right) + \frac{R}{M_t}S_t + \frac{R}{M_g}S_g \tag{2.14}$$

The partial pressure equations for tar and gas are described as below.

$$\frac{\partial}{\partial t}\left(\frac{\varepsilon P_t}{T}\right) = \vec{\nabla}\cdot\left(\frac{BP_t}{\mu T}\vec{\nabla}P\right) + \frac{R}{M_t}S_t \tag{2.15}$$

$$\frac{\partial}{\partial t}\left(\frac{\varepsilon P_g}{T}\right) = \vec{\nabla}\cdot\left(\frac{BP_g}{\mu T}\vec{\nabla}P\right) + \frac{R}{M_g}S_g \tag{2.16}$$

In prolate coordinate system, Equation 2.15 and Equation 2.16 become

$$\frac{\partial}{\partial t}\left(\frac{\varepsilon P_t}{T}\right) = \frac{1}{f^2(\xi^2-\eta^2)}\left[\frac{\partial}{\partial \xi}\left(\frac{BP_t}{\mu T}(\xi^2-1)\frac{\partial P}{\partial \xi}\right) + \frac{\partial}{\partial \eta}\left(\frac{BP_t}{\mu T}(1-\eta^2)\frac{\partial P}{\partial \eta}\right)\right] + \frac{R}{M_t}S_t \tag{2.17}$$

$$\frac{\partial}{\partial t}\left(\frac{\varepsilon P_g}{T}\right) = \frac{1}{f^2(\xi^2-\eta^2)}\left[\frac{\partial}{\partial \xi}\left(\frac{BP_g}{\mu T}(\xi^2-1)\frac{\partial P}{\partial \xi}\right) + \frac{\partial}{\partial \eta}\left(\frac{BP_g}{\mu T}(1-\eta^2)\frac{\partial P}{\partial \eta}\right)\right] + \frac{R}{M_g}S_g \tag{2.18}$$

2.2.3 Conservation of Energy

The heat transfer in the particle is controlled by three mechanisms, the heat conduction driven by temperature gradient, the convection by the gas flow through the porous particle, and the radiation among the pore surfaces. Radiative heat transfer occurs when there exists temperature differences in the pore surfaces. The radiation is important during pyrolysis process especially in the later stage when the pore size increases and the temperature is high.

To simplify the simulation, conductive and radiative heat transfer are considered together by using an effective thermal conductivity λ. It consists of the conductivity of virgin wood, char, and volatiles as well as the radiative heat transfer through the pores, as depicted below

$$\lambda = (1-\nu)\lambda_w + \nu\lambda_c + \varepsilon\lambda_v + 13.5\sigma T^3 d/e \tag{2.19}$$

where, σ is the Stefan-Boltzmann constant, e is the emissivity and d is the pore size.

The reaction heat is very important in modeling the endothermic and exothermic effect during pyrolysis process. In this model, the primary reactions from wood to gas, tar, and char are endothermic, and the secondary reactions are exothermic. The energy change in the controlled volume is governed by the thermal conduction, gas convection, and the heat generation from pyrolysis reactions. It is assumed that there exists a local thermodynamic equilibrium between gas and solid phase components.

$$(\rho_s C_s + \varepsilon\rho_v C_v)\frac{\partial T}{\partial t} + \rho_v C_v \vec{V}\cdot\vec{\nabla}T = \vec{\nabla}\cdot(\lambda\vec{\nabla}T) + Q \tag{2.20}$$

where, $Q = -(k_t \Delta h_t + k_g \Delta h_g + k_{is} \Delta h_{is})\rho_a - k_c \Delta h_c \rho_{is} - (k_{c2} \Delta h_c 2 + k_{g2} \Delta h_{g2})\rho_t$, $\rho_s C_s = (\rho_a + \rho_{is})C_w + \rho_c C_c$, and $\rho_v C_v = \rho_g C_{pg} + \rho_t C_{pt}$.

Replacing $\vec{V}$ with Equation 2.11 and rewriting the energy equation in prolate coordinate system gives us

$$
\begin{aligned}
(\rho_s C_s + \varepsilon \rho_v C_v)\frac{\partial T}{\partial t} = \rho_v C_v \frac{B}{\mu} \frac{1}{f^2(\xi^2 - \eta^2)} \left[\frac{\partial}{\partial \xi}(\xi^2 - 1)\frac{\partial P}{\partial \xi}\frac{\partial T}{\partial \xi} + \frac{\partial T}{\partial \eta}(1 - \eta^2)\frac{\partial P}{\partial \eta}\frac{\partial T}{\partial \eta} \right] \\
+ \frac{1}{f^2(\xi^2 - \eta^2)} \left[\frac{\partial}{\partial \xi}\left(\lambda(\xi^2 - 1)\frac{\partial T}{\partial \xi} \right) + \frac{\partial}{\partial \eta}\left(\lambda(1 - \eta^2)\frac{\partial T}{\partial \eta} \right) \right] \\
+ Q \qquad (2.21)
\end{aligned}
$$

2.2.4 Initial Conditions

At $t = 0$, the temperature of the particle is uniformly distributed at T_0 (300K). The pressure inside the particle is atmospheric (101,300 Pa). Density of wood is the same as dry wood and that of char and intermediate solid are zero. Inert gas is not included here to reduce the number of variables and make the model simpler. This simplification is reasonable since the mass of inert gas occupying the pore space initially is negligible in comparison to the mass of gas and tar generated during the reaction.

$$
\begin{aligned}
&T(\xi, \eta, 0) = T_0, \quad P(\xi, \eta, 0) = P_0 \\
&\rho_a(\xi, \eta, 0) = \rho_0, \quad \rho_{is}(\xi, \eta, 0) = 0, \quad \rho_c(\xi, \eta, 0) = 0 \qquad (2.22)
\end{aligned}
$$

2.2.5 Boundary Conditions

Symmetric conditions are assumed at the plane of symmetry, therefore the gradients of temperature and pressure equal to zero.

$$\frac{\partial T(\xi,\eta=1,t)}{\partial \eta}=0, \quad \frac{\partial T(\xi,\eta=0,t)}{\partial \eta}=0, \quad \frac{\partial T(\xi=1,\eta,t)}{\partial \xi}=0$$
$$\frac{\partial P(\xi,\eta=1,t)}{\partial \eta}=0, \quad \frac{\partial P(\xi,\eta=0,t)}{\partial \eta}=0, \quad \frac{\partial P(\xi=1,\eta,t)}{\partial \xi}=0 \tag{2.23}$$

The pressure at the particle surface is atmospheric and the ratio of gas and tar is obtained by numeric extrapolation of the volatile composition close to the surface. This type of condition is simple and assumes that surrounding inert gas would not flow into the wood sphere during the reaction. For low temperature pyrolysis where inert gas may diffuse backward to the particle, this model should not be used and diffusion terms need be included for each species in Equation 2.9 and Equation 2.10.

$$P(\xi=\xi_s,\eta,t)=P_0 \tag{2.24}$$

Thermal flux through the surface of the particle is determined by convective and radiative heat transfer. Reaction heat is not included since there is no heat accumulation at the interface. Convective heat transfer from the gases is also not presented due to the fact that these gases merely cross the boundary without adding or removing any heat.

$$\frac{\lambda}{f}\sqrt{\frac{\xi^2-1}{\xi^2-\eta^2}}\frac{\partial T_s}{\partial \xi_s}=h(T_g-T_s)+\sigma e_s(T_f^4-T_s^4) \tag{2.25}$$

where, T_s, T_g and T_f are the temperatures of the particle surface, gas and furnace wall respectively. The surface emissivity e_s is calculated by

$$\begin{cases} e_s=e_w & T_s<450K \\ e_s=e_w+\dfrac{T_s-450}{550-450}(e_c-e_w) & 450\geq T_s<550K \\ e_s=e_c & T_s\geq 550K \end{cases} \tag{2.26}$$

The kinetic parameters for wood pyrolysis and the physical properties of biomass particles can be found in literature [26]. Conservation equations for the oblate spheroids can be found in Appendix A.

2.2.6 Numerical Procedure

The computational domain is illustrated in Figure 2.5 where the nodal points and lines of constant ξ and η are presented. Finite volume method (FVM) is applied to solve the mass and energy conservation equations. Temperature and pressure equations are coupled with each other, but since they cannot be solved together due to the presence of non-linear terms, they are solved alternately and iterated to obtain consistency between pressure and temperature at each time step. The convection term in the Equation 2.21 is discretized by upwind scheme to enhance solution stability. Details of the numerical discretization can be found in Appendix B.

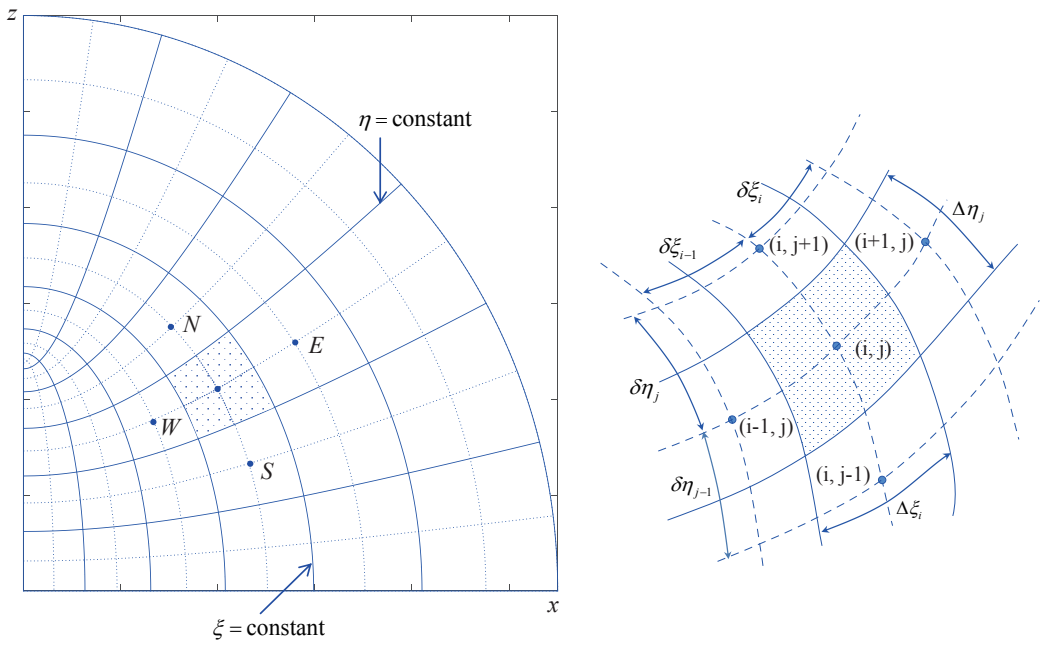

Figure 2.5: Grid index stencil for control volume method used in this work.

Procedures of numerical modeling are illustrated in Figure 2.6. In the initialization stage, all the relevant parameters that define this problem are read into computer

memory, including the geometry, mesh size, kinetics, initial and boundary conditions, etc. Then, the material properties, such as the heat conductivity, specific heat capacity, permeability, and porosity, are calculated for the current time step. Once the reaction rate and heat generation are obtained, the temperature and pressure fields are solved using FVM and iterative method. Then, temperature and pressure fields are updated with the latest value. The above processes are repeated till the end of the pyrolysis process.

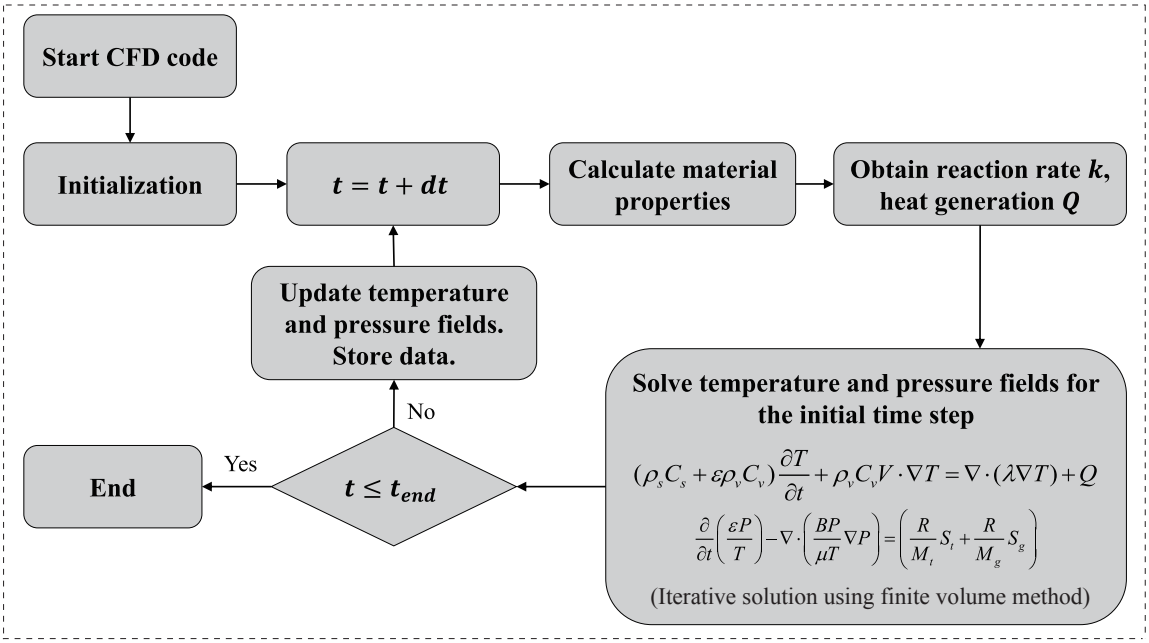

Figure 2.6: Numerical procedure to solve the mass and energy conservation equations.

2.2.7 Simulation Cases

Furnace temperature was set at 783 K and gas temperature is 720 K. In order to examine the effects of particle shapes and sizes on the pyrolysis of wood particles, two sets of simulations were performed for both prolate and oblate spheroids.

1. Keeping semi-major axis L_2 constant (L_2: 0.5cm, 1.0cm, 1.5cm, 2.0cm) while varying aspect ratio ϵ from 1/9 to 9/9 (with steps of 1/9) for each L_2.

2. Keeping equivalent radius R_e constant (R_e: 0.5cm, 1.0cm, 1.5cm, 2.0cm) while varying aspect ratio ϵ from 1/9 to 1 (with steps of 1/9) for each R_e.

Here, equivalent radius (R_e) is the radius of a sphere with the same volume or mass as the non-spherical particle. Details of the above variations for oblate spheroids are shown in Figure 2.7 and Figure 2.8.

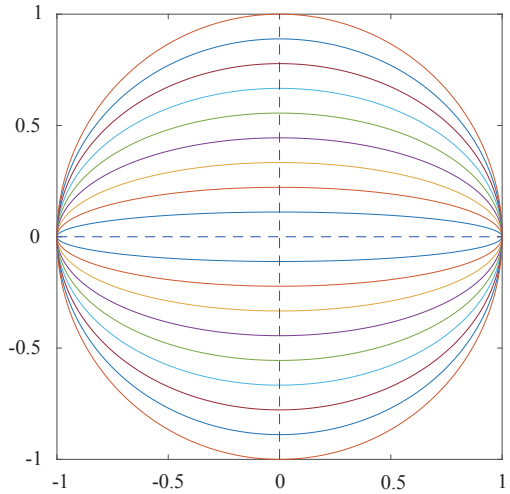

Figure 2.7: Keep semi-major axis L_2 constant while changing aspect ratio ϵ from 1/9 to 1. L_2 is changed from 0.5cm to 2.0cm with steps of 0.5 cm. L_2 =1.0 cm in this figure.

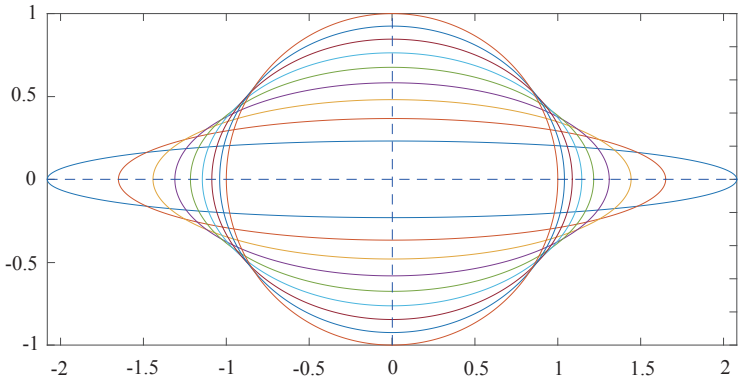

Figure 2.8: Keep equivalent radius R_e constant while changing aspect ratio ϵ from 1/9 to 1. R_e is the radius of a sphere with the same volume or mass as the aspherical particles. R_e is changed from 0.5cm to 2.0cm with steps of 0.5 cm. R_e =1.0 cm in this figure.

2.3 Experiment

Pyrolysis experiments were carried out under atmospheric pressure in a tube furnace as shown in Figure 2.9 and details can be found in [29]. The tube (length: 558 mm, ID: 106 mm) is made from mullite and the heating zone is 300 mm long. Argon was used to purge the furnace and carry away pyrolysis vapors. The mass flow rate of argon was controlled by a sonic orifice and set at 0.21 g/s. Particle mass was monitored by the electronic balance and temperature was measured by K-type thermocouples. Maple wood particles of various shapes and sizes were used and their geometrical parameters are listed in Table 2.1. All the wood particles were dried in an oven at 90°C for 12 hours to remove moisture and subsequently stored in an airtight container. Furnace temperature was set at 783 K (510°C) and the measured gas temperature near the wood particles was 743 ± 20 K (470 ± 20°C).

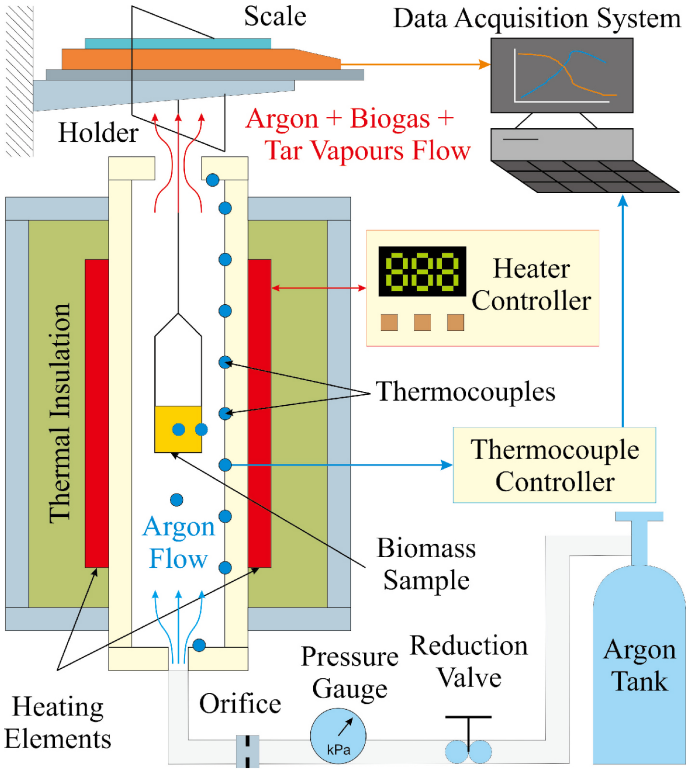

Figure 2.9: Schematic of the experimental apparatus.

Table 2.1: Shapes and sizes of maple wood particles.

Shape	Nominal Dimension (mm)
Spheres: D	10, 15, 20
Cubes: L	10, 15, 20
Cylinders: D×H	10×20, 15×20, 20×20
Cuboids: L×W×H	10×10× 5, 15×10× 5, 20×10×10, 20×20×15

2.4 Results and Discussion

2.4.1 Verification of Numerical Model

To validate the numerical methodology used in this work, Figure 2.10 demonstrates a comparison between the numerical results obtained in the current study and previous work [26] for wood pyrolysis at 783 K. As can be seen, good agreement was obtained for profiles of solid mass fraction, center temperature, and center pressure. It is also necessary to mention that prolate spheroid is not a sphere, and the aspect ratio ϵ can never equal or be larger than 1. Thus the current model use prolate and oblate spheroids with aspect ratio $\epsilon = 0.999$ to approximate a sphere particle.

The pyrolysis duration is defined based on the temperature profile. It is the time period required for the center temperature to reach the peak. After the pyrolysis duration, the pyrolysis process completes and the mass profile stops changing.

2.4.2 Effect of Particle Shape and Size on the Solid Mass Fraction and Center Temperature

As mentioned earlier, two types of numerical simulations were performed to document the effect of shape and size on wood pyrolysis. In one set of calculations, the major axis length is kept constant while aspect ratio is varied, whereas in the second one, the equivalent radius is kept constant (i.e., volume) and the major and minor axes are determined according to aspect ratio. A sweep of equivalent radius

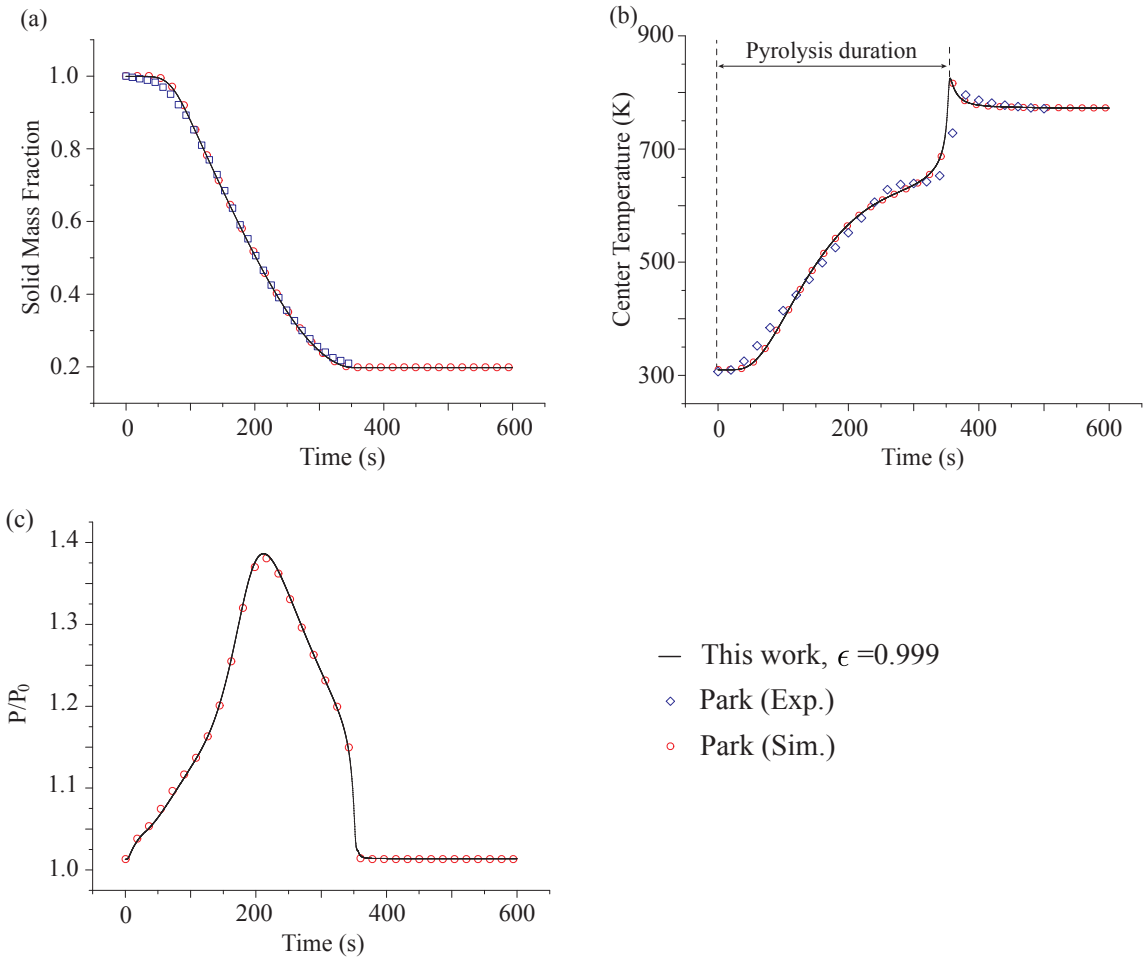

Figure 2.10: Comparison of results from the current numerical model (continuous line, ϵ=0.999, L2=1.27cm) with the results obtained by Park et al. [26] (red circles: simulation, blue diamond: experiment) for pyrolysis of a spherical wood particle of 1.27 cm radius. (a): solid mass fraction; (b): center temperature; (c): ratio of center pressure and ambient pressure.

enables the change in the size of particles and a sweep of aspect ratio gives different shapes, thus allowing us to decouple the effects of shape and size. In the interest of brevity, only the profiles of prolate particles with equivalent radii of 1.0 and 1.5 cm are presented.

The solid mass fraction is calculated as $Y = m/m_0$, where m is the particle mass at a particular instant in the pyrolysis process and m_0 is the initial particle weight. Figure 2.11(a) and Figure 2.11(b) depict the solid mass fraction of prolate particles of

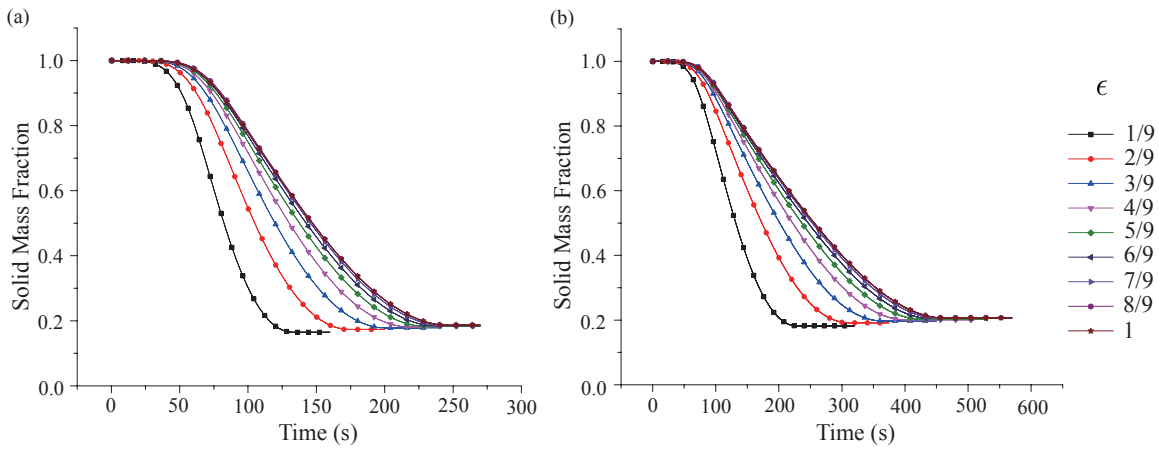

Figure 2.11: Mass loss profiles for different prolate particles. (a):R_e = 1.0 cm; (b):R_e = 1.5 cm.

equivalent radius 1.0 cm and 1.5 cm respectively, and the aspect ratios change from 1/9 to 1. The mass loss profiles of oblate particles of equivalent radius 1.0 cm and 1.5 cm are shown in Appendix A. In all cases, a mild weight loss rate is observed at the beginning, then the solid mass fraction decreases rapidly and the rate of weight loss remains approximately constant over a long time where the majority of the weight loss occurs, finally the solid mass fraction changes progressively slowly and gradually becomes constant. It can also be observed from Figure 2.11(a) and Figure 2.11(b) that mass loss profiles vary significantly with aspect ratios when the solid volume is fixed and pyrolysis takes less time to complete for the solids with smaller size. Specifically, decreasing aspect ratio makes wood decompose faster and there is also a smaller final char fraction; while increasing particle size causes wood particles to decompose increasingly slowly and leads to a higher final char fraction. Particles of smaller aspect ratio like needles or disks, or particles of small sizes, enable mass transfer over shorter length scales and higher heating rates which ultimately lead to a quick wood devolatilization.

Temperature profiles at the center of prolate and oblate wood particles during pyrolysis are shown in Figure 2.12 and Appendix A. The center temperature initially increases almost linearly due to heat transfer via conduction. A plateau then appears

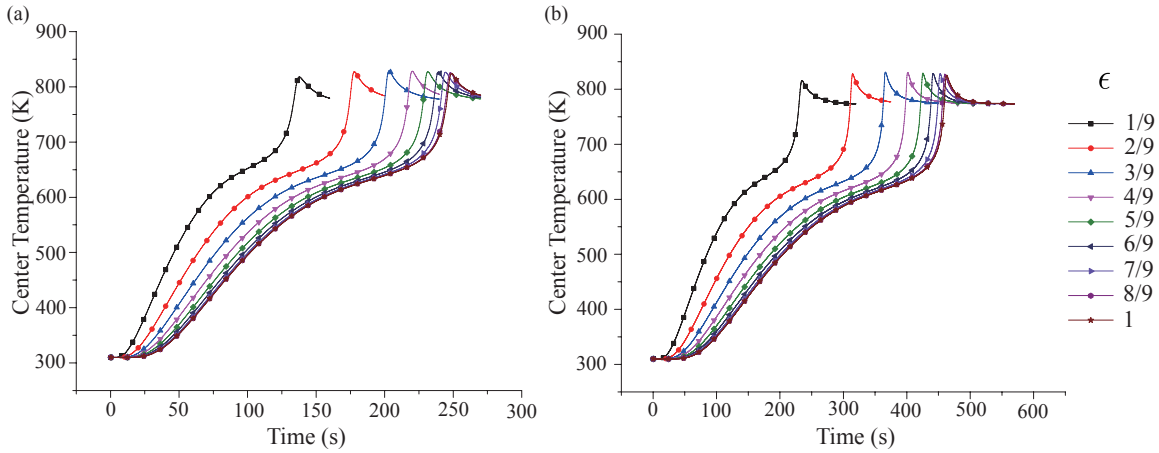

Figure 2.12: Center temperature profiles for different prolate particles. (a):$R_e = 1.0$ cm; (b):$R_e = 1.5$ cm.

in the range of 600-700 K, indicating the occurrence of endothermic reactions of wood decomposing to gas, tar and intermediate solid. Further on, it undergoes a sharp increase and exceeds the furnace temperature because of exothermic reactions. Finally, the temperature stabilizes and a thermal equilibrium is attained within the furnace. The temperature plateau and overshooting were also observed in experiments, and two theories were proposed to explain the phenomena and the details can be found in Chapter III. Temperature profiles shown in Figure 2.12(a) and Figure 2.12(b) reveal that as we decrease ϵ of a particle or reduce its size, the center temperature peak shifts to the left, indicating higher temperature increase rates. This occurrence is consistent with observations in mass loss profiles and expectations of higher heating rates for smaller particles. For particles of the same R_e or volume, reducing the aspect ratio means an increase of surface area, allowing more heat to be received from the furnace and ultimately resulting in a higher heating rate, thus the particles will be heated faster and decompose quickly.

2.4.3 Effect of Surface to Volume Ratio on Pyrolysis Duration

Wood conversion takes place as a result of a strong interaction between chemistry and transport phenomena at the levels of the single particle and the reaction

environment [25], and how long a particle should be exposed to the external heat flux to accomplish pyrolysis procedure and produce pyrolysis gases is an important parameter for designing a pyrolysis reactor. Here, pyrolysis duration (t_{con}) is used to characterize the conversion time of a single wood particle. To demonstrate the effect of SVR of a particle on the pyrolysis conversion time, Figure 2.13 summarizes the results of all the simulation cases for both prolate and oblate ellipsoids which have R_e of 0.5 cm, 1.0 cm, 1.5 cm, 2.0 cm and ϵ ranging from 1/9 to 1. As is unmistakably apparent, the pyrolysis duration is significantly affected by SVR and particles with larger SVR have smaller conversion time. This is not hard to understand since larger SVR implies that the wood particles will be heated up faster, and thus decompose quicker.

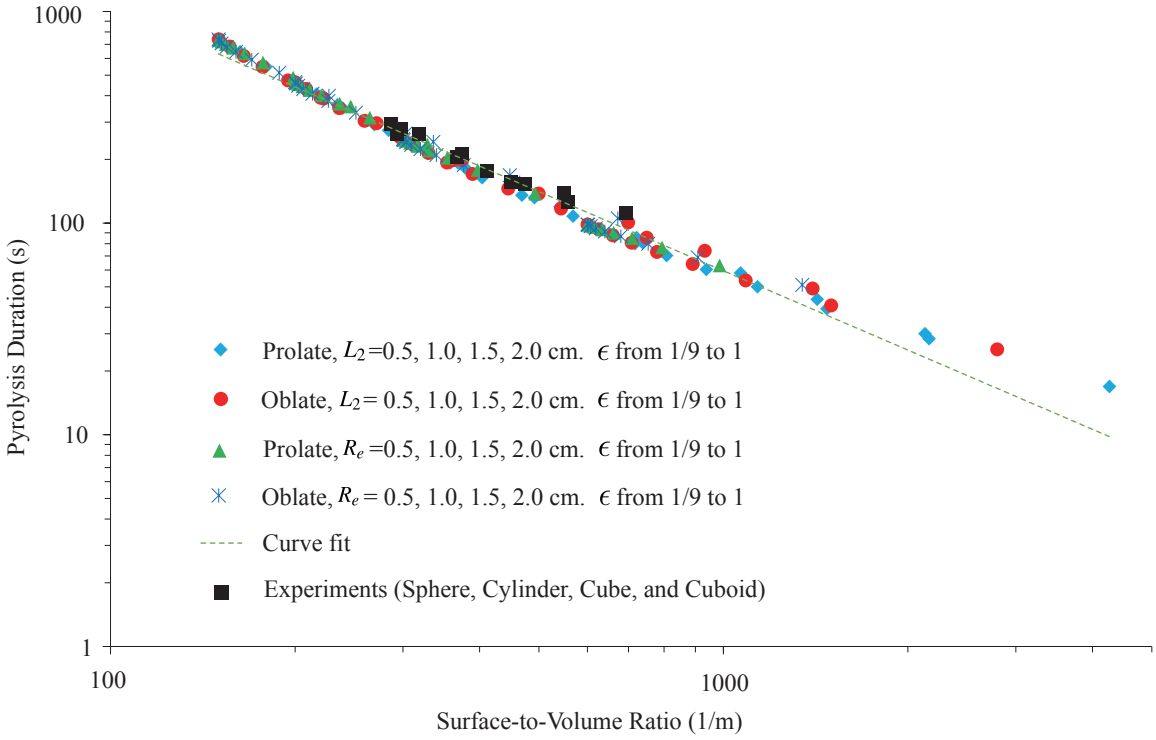

Figure 2.13: Effect of surface-to-volume ratio on the pyrolysis duration of a single wood particle.

A remarkable result is that pyrolysis durations for both ellipsoids collapse onto one curve. A power-law based curve fit of the data (excluding the experimental data)

gives the following correlation with a notably good R-squared value (0.984):

$$\ln(t_{\text{con}}) = -1.243 \times \ln(\text{SVR}) + 12.676 \tag{2.27}$$

When the experimental data is superimposed on this curve, it agrees extraordinarily well with the simulation results. Such a correlation function can serve as an immensely powerful tool to predict pyrolysis duration of wood particles having arbitrary shapes and sizes. The development of biomass conversion processes and the design of pyrolysis reactors require a good understanding of the physical and chemical reactions during the thermo-chemical decomposition process, and mathematical simulation represents a useful tool to understand some of these processes. This model can be used to predict the pyrolyzate production rate for an ensemble of different size and shape biomass particles at various heating rates, correlate the data and generalize the results. It is necessary to mention that such a correlation is a function of the furnace conditions, and both the simulated and the experimental data have been obtained for a furnace temperature of 783 K. If the furnace temperature is changed, a different correlation function is to be expected.

2.4.4 Effect of Particle Aspect Ratio on Pyrolysis Duration

Another important parameter characterizing a spheroidal particle is ϵ (aspect ratio), which is defined as the ratio of the minor axis and major axis. Figure 2.14 illustrates the relation between ϵ and pyrolysis duration for prolate particles with R_e equals 0.5 cm, 1.0 cm, 1.5 cm, and 2.0 cm. As can be observed, particle shape and size have a strong influence on the pyrolysis duration. Results for oblate wood particles can be found in Appendix A. For a given ϵ, with the increase of particle size, the pyrolysis duration will increase correspondingly. Besides, the pyrolysis duration almost doubles when the ϵ changes from 1/9 to 1 for prolate solids of different R_e.

Figure 2.14 also presents the effect of ϵ on conversion time ratio, which is defined

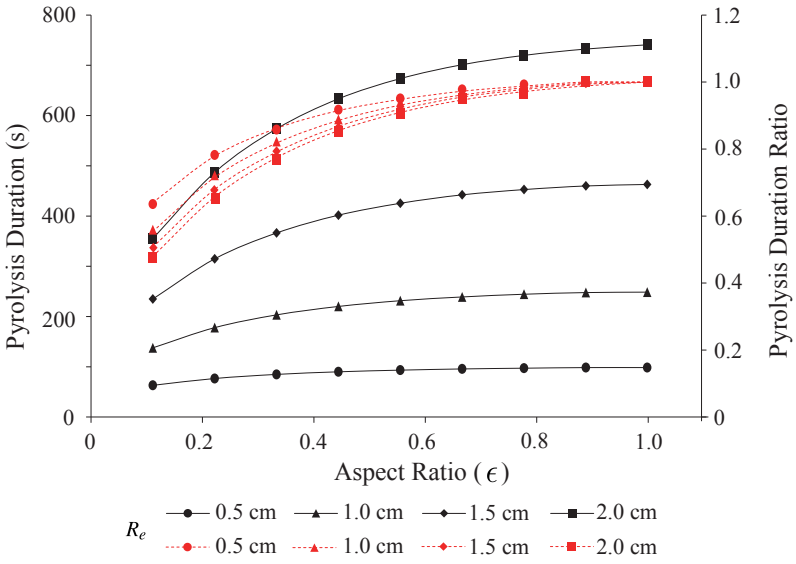

Figure 2.14: Effect of aspect ratio on the pyrolysis duration of prolate wood particles. $R_e = 0.5$ cm, 1.0 cm, 1.5 cm and 2.0 cm. Line: pyrolysis duration; Dashes: pyrolysis duration ratio.

as the ratio between the pyrolysis duration of a prolate particle and that of an equivalent sphere (a sphere having R_e as its radius). For all R_e, pyrolysis duration ratio is the lowest for $\epsilon = 1/9$ and monotonically increases to 1 as ϵ increases to 1. This can be explained based on the fact that for lower ϵ, the particle is highly dissimilar as compared to its equivalent sphere and as ϵ increases, the particle becomes progressively similar to its equivalent sphere. The limiting case is $\epsilon = 1$ when the particle and its equivalent sphere are exactly the same, thus having exactly the same pyrolysis duration which yield a pyrolysis duration ratio of 1. It is also interesting to notice that prolate ellipsoid of R_e of 0.5 cm has the largest pyrolysis duration for each ϵ, but the difference (as compared with particles having different R_e) grows increasingly less prominent for higher R_e, as we can see from the fact that the prolate solids of 1.5 cm and 2.0 cm equivalent radius share an approximately same profile. The change of pyrolysis duration with aspect ratio can also be explained by Figure 2.14. While maintaining R_e (i.e. the volume) of a wood particle constant, increasing aspect ratio means the reduction of SVR which reaches the minimum when aspect ratio becomes

1, hence causing slower heating of the particle and longer pyrolysis duration.

2.4.5 Effect of Particle Sizes and Shapes on Product Yields

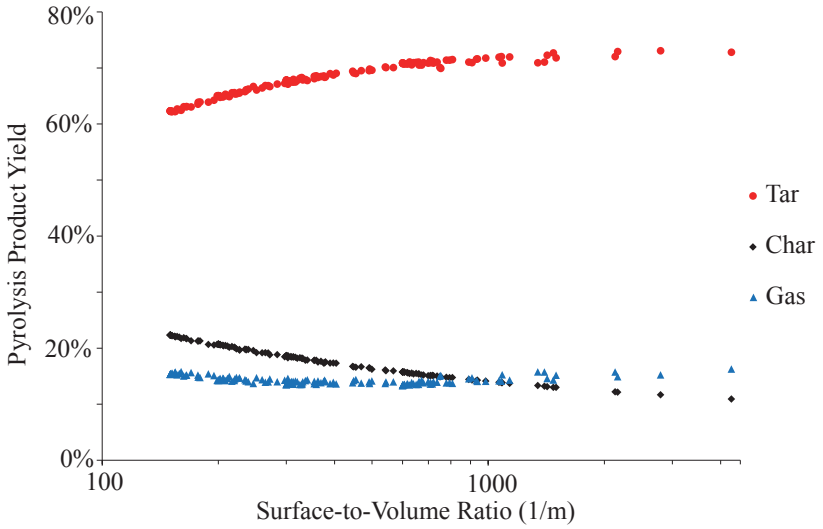

Figure 2.15: Variation of pyrolysis product yield for different surface-to-volume ratio. Data is obtained from the same modeling cases as Figure 2.13.

Figure 2.15 demonstrates the effect of SVR on the yields of three classes of lumped pyrolysis products, namely char, tar, and gas. Increasing SVR enhances the production of tar and decreases the yield of char, while the yield of gas is not significantly affected. Particle size affects the yields of pyrolysis products by changing the temperature gradients and the residence time of volatile vapors inside the hot wood particles. The discussion in the preceding segment concludes that pyrolysis duration decreases with increasing SVR and the correlation can be explained by a power-law based function. For particles with higher SVR, decomposition is quicker and the time taken for tar to transport through hot porous solids is shorter and the secondary tar decomposition is weakened, consequently resulting in an increase of tar yield. Slow pyrolysis favors char production, therefore lower SVR leads to more char yield by slowing down the heating rate of wood particles. As shown in Figure 2.1, gas production takes place via two routes: (1) Direct decomposition of the virgin wood; (2) Secondary decompo-

sition of tar. Increasing SVR causes faster heating of wood particles, thus more gas will be produced by the first route but less via the secondary tar decomposition (as explained above). These two effects neutralize each other and this can be one of the reasons why the yield of gas is not significantly affected by SVR.

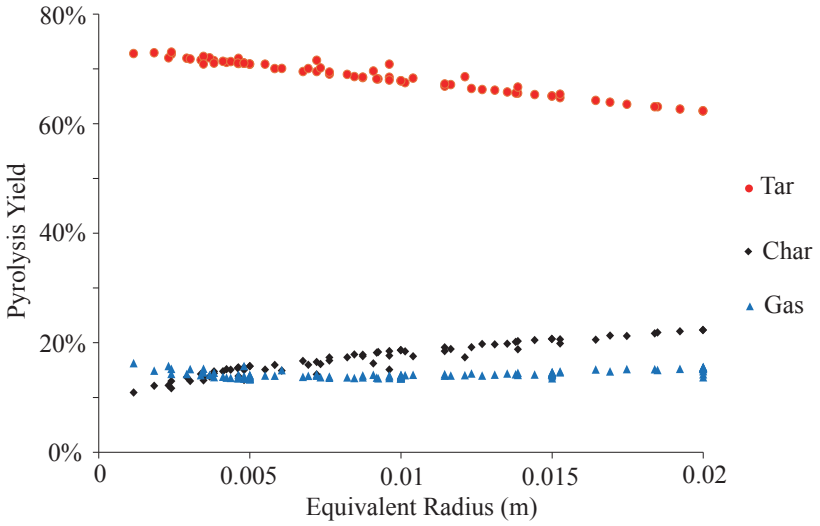

Figure 2.16: Predicted product yield for various equivalent radius R_e. Data is obtained from the first set of simulations, that is, by keeping the semi-major axis of prolate and oblate constant (L_2: 0.5cm, 1.0cm, 1.5cm, 2.0cm) and changing the aspect ratio from 1/9 to 1.

Particle size affects the yield of pyrolysis product by creating temperature gradients and changing the residence time of volatile vapors inside the wood particle. To understand the relation existing between particle size and pyrolysis products, the yields of char, tar and gas are plotted against the equivalent radius of various prolate and oblate spheroidal wood particles in Figure 2.16. Pyrolysis yields of tar and char vary almost linearly with increasing equivalent radius, and the change of gas yield is not significant. This trend is consistent with the discussions above and could be explained as follows. Large particles are heated more slowly and have longer conversion time than smaller ones. Besides, tar will have longer diffusion path in large particles and needs more time to escape, thus the secondary tar decompositions are enhanced. All of these reasons contribute to the reduction of tar and increase of char when large

particles are used for pyrolysis.

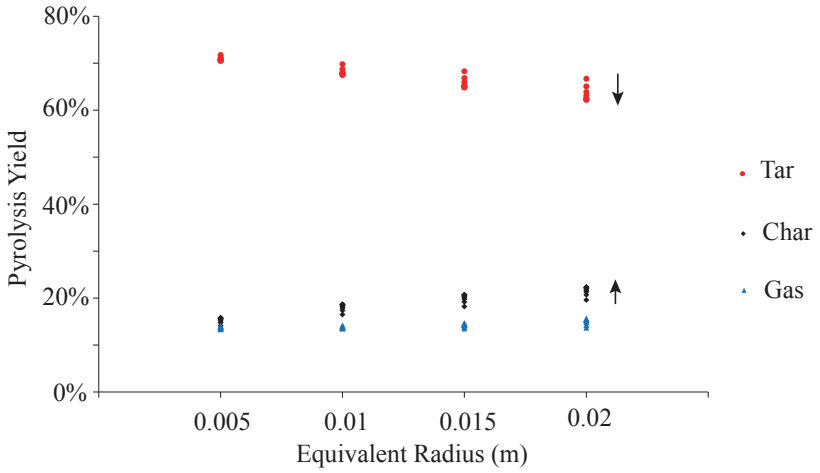

Figure 2.17: Effect of aspect ratio ϵ on the pyrolysis yield of prolate wood particles. Data is obtained from the first set of simulations, that is, by keeping the semi-major axis of prolate constant (L_2: 0.5cm, 1.0cm, 1.5cm, 2.0cm) and changing the aspect ratio ϵ from 1/9 to 9/9. The direction of arrow indicates the increase of aspect ratio.

The aspect ratio is an important parameter characterizing the shape of a spheroidal solid, and it will affect product yields by changing the heat and mass transfer processes during pyrolysis. Figure 2.17 illustrates the change of pyrolysis product yield with various prolate aspect ratio under different equivalent radius. As shown in Figure 2.17, particles having geometry close to a sphere has a larger char yield and smaller tar yield, and gas is not remarkably affected. For prolate solids with fixed volume, decreasing aspect ratio increases the surface/volume ratio and makes biomass particle thinner, therefore the particles will be heated faster and the volatiles will be released sooner. On the other hand, the effect of shape on pyrolysis yield is also limited by particle sizes. Figure 2.17 indicates that the influence of prolate aspect ratio on pyrolysis yields when the equivalent radius is 0.005 m is not as significant as the effect when the equivalent radius is 0.02 m. Generally, small particles are heated much more rapidly than large ones, thus the conversion time is small enough to reduce the impact from particle shape. Biomass particles in fluidized bed reactor have a wide variety of shapes and sizes, thus each particle has an individual pyrolysis pro-

cess. On the other hand, the effect of shapes on pyrolysis products is not remarkable when particle size is small enough. To summarize, assuming biomass particles to be a sphere in numerical simulation is still reasonable when particle sizes are small, one needs to be careful with this simplification when particle size becomes large.

2.5 Conclusion

In this work, pyrolysis of wood particles of various shapes and sizes was studied experimentally and theoretically. Prolate and oblate theories were applied to solve the two stage pyrolysis model and simplify the geometrical description of particles of infinite shapes and sizes. Particle sizes and shapes affect heat and mass transfer processes thus affecting wood pyrolysis. There exists a power law based correlation function between pyrolysis duration and surface/volume ratio and such a relation was also verified by experiment. Pyrolysis conversion time was found to be affected by surface/volume ratios, and increasing surface/volume will make wood decompose faster and decrease conversion time. Biomass particles of large surface/volume ratios tend to have a higher yield of tar and a less yield of char, but gas product is not significantly impacted.

CHAPTER III

The Effect of Torrefaction on the Pyrolysis of Centimeter-scale Biomass Particles

3.1 Introduction

The bio-oil that is produced from pyrolysis process has a very complicated composition, which is not only affected by the material properties of the biomass feedstock, but also by conditions in which the process is conducted (reactor temperature, heating rate, pressure, carrying gas flow rate, etc.). More than 300 organic compounds have been reported in bio-oil as a result of pyrolysis process and they belong to a variety of chemical function groups such as sugars, acids, aldehyds, ketones, phenols, esters, ethers, furans, nitrogen and sulfur compounds, and other compounds [11].

Bio-oil contains a large amount of oxygen ($\sim 40\%$) and has large water fraction; these lower its energy content. Also the presence of carboxyl groups (COOH) makes it highly acidic (pH$\sim$2) and corrosive and thus difficult to store [6]. Another problem related to bio-oil is its aging effect. Pyrolysis vapors contains many oxygenated organic compounds with a wide range of molecular weights. During the process of rapid cooling or quenching of the pyrolysis vapor from the pyrolysis temperature, the condensates are not in thermodynamic equilibrium [30, 31]. So the chemical composition as well as the physical properties of the bio-oil will change toward thermodynamic

equilibrium during the storage process. All these constraints need to be solved to achieve practical usage of bio-oils.

A potential method to reduce the oxygen content and improve bio-oil quality is to decompose the biomass in a relatively low temperature range of 225-300 °C, a process known as torrefaction [32, 33, 34]. O/C ratio of the wood decreases during torrefaction, causing the energy density of the torrefied wood to increase compared with untreated wood [35, 36]. Additionally, after torrefaction, biomass has hydrophobic characteristics that makes storage of torrefied biomass more convenient [37, 38]. Furthermore, the reactivity and grindability of woody biomass are also enhanced after torrefaction [39, 40]. These characteristics benefit further processes such as combustion, gasification, and fast pyrolysis.

There has been a fair amount of research on pyrolysis of torrefied wood, and torrefaction is considered as an effective pretreatment strategy for fast pyrolysis to produce high quality bio-oil [41, 42]. However, studies regarding pyrolysis of torrefied wood were rarely done on centimeter-scale biomass particles, and dynamic changes of temperature and solid mass fraction were seldom reported [43, 44]. The objective of this study is to investigate the effect of torrefaction on pyrolysis of centimeter-scale pine wood particles. This influence was analyzed in terms of the pyrolysis process, product yields and the chemical composition of the bio-oil obtained. Temperature and weight loss measurements were also made.

3.2 Materials and Methods

3.2.1 Materials

Pine wood particles with a dimension of 0.75 × 0.75 × 3 inches (19.1 × 19.1 × 76.2 mm) was used as the feedstock. These wood particles were dried in an oven at 105 °C for 12 hours before the pyrolysis experiments to remove free moisture,

and subsequently stored in an airtight container. Measured properties of pine wood samples are given in Table 3.1. The elemental composition was analyzed by Atlantic Microlab, Inc., the ash content was measured by EMSL Analytical, Inc., and the volatile matters and fixed carbon content were determined by a Perkin-Elmer TGA-7. The Biot number of the particle in the furnace is about 10 and the pyrolysis number is about 0.01[1]. Thus it falls in the conduction-controlled region in Figure 1.1.

Table 3.1: Proximate and elemental analysis of pine wood sample (wt.%, on dry basis).

Proximate Analysis	
Volatile Matters	84.65 ± 1.64
Fixed carbon	15.22 ± 1.64
Ash	0.13 ± 0.00
Elemental Analysis	
C	47.17 ± 0.05
H	6.07 ± 0.01
N	0.13 ± 0.00
O[2]	46.63 ± 0.06

3.2.2 Experiments Setup and Procedures

Pyrolysis experiments were carried out under atmospheric pressure in a tube furnace shown in Figure 3.1, which was modified from the previous setup (Figure 2.9). The tube (length: 460mm, ID: 57mm, OD: 64mm) was made from mullite and the total heated zone was 300 mm. Nitrogen (N_2) was used to purge the furnace and carry away the pyrolysis gases. The N_2 mass flow rate was 0.05g/s and controlled by a sonic orifice and a pressure gauge.

[1]The following approximate properties are used for calculation: $\lambda = 0.15W/mK$, $\rho = 430kg/m^3$, $C_p = 2.5kJ/kgK$, $L = 0.0762m$, $k = 0.0025s^{-1}$. The exact value may be different.

[2]Calculated by difference

A wire holder made from stainless steel was used to hold the wood sample to ensure the radiation from the furnace can directly reach the sample. After the furnace temperature became stable, wood was put in the holder and first positioned at the cooling zone of the reactor for 2 minutes, allowing the nitrogen to purge the air that may have leaked in when biomass was fed; then it was immediately inserted into the heating zone of the furnace.

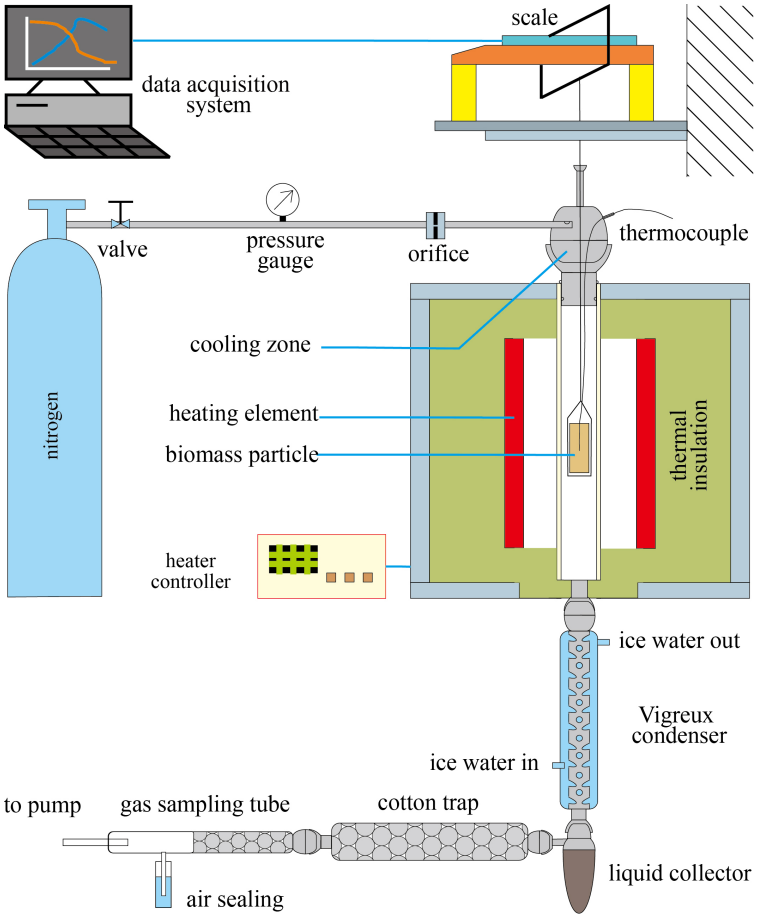

Figure 3.1: Schematic of the experiment apparatus.

Pyrolysis vapors exited the furnace and entered a condensation system consisting of a jacketed Vigreux condenser cooled by ice-water (where majority of the liquid was collected and chemically analyzed), a cotton wool filter tube and a gas sampling tube. All the experiments were conducted at 520 °C. In each case, two separate experiments were conducted for the same conditions. One was used for bio-oil production and

temperature measurement; the other one was used for continuous measurements of weight loss. The liquid yield was calculated by weighing all the condensable products trapped in the condensation system. Char was measured as the final solid mass fraction. The amount of gas was determined by the difference between the weight of biomass and that of char and liquid.

The setup was also used for wood torrefaction. N_2 flow was adjusted to 0.038 g/s and condensers were removed. After the furnace was heated to the desired temperature (225 °C, 250 °C, 275 °C or 300 °C) and reached a steady state temperature, dry wood was inserted into the reactor center and torrefied for different times (15 min, 25 min, and 35 min). These torrefied wood samples are denoted by T_X_Y, where X is the torrefaction temperature and Y is torrefaction time. The weight loss (Y_L, wt.%) of pine wood after torrefaction was determined by $Y_L = 100 \times (1–m_t/m_0)$, where m_0 is the initial mass of pine wood and m_t is the residual mass after torrefaction.

3.2.3 Characterization of Pyrolysis Products

Quantification analysis of the liquid was performed by a Shimadzu GC/MS – QP 2010 with a DB-5 capillary column (30 m × 0.25 mm × 0.25 µm). Helium was used as carrier gas. Column was programmed to stay at 40 °C for 4 min, increase to 235 °C at 5 °C/min and held at this final temperature for 5 min. Pyrolysis liquid was dissolved in acetone (10 wt.% pyrolysis liquid) and a volume of 0.5 µL was injected in split mode (split ratio was 50:1). Injection and GC-MS interface temperature were 235 °C. The mass spectrometer was operated in scan mode with a mass range (m/z) of 40 to 400. Compound identification was based on comparison with the NIST library [45].

3.3 Results and Discussion

3.3.1 Torrefaction of Pine Wood

During torrefaction, biomass loses weight by thermal degradation of hemicellulose and cellulose at elevated temperatures, so the weight loss can be used to characterize the intensity of torrefaction processes. Table 3.2 summarizes the weight loss of pine wood after torrefaction under different conditions. As we can see, the sample weight loss is greatly dependent on the torrefying conditions. With the increase of reaction temperature and time, the weight loss changes from 0.72% to 23.88%. It's also interesting to note that the weight experiences little change when wood is torrefied at 225 °C and 250 °C. However, the weight loss increases sharply after 275 °C and a very large weight loss, 23.88%, is observed at the temperature of 300 °C, indicating severe decomposition has occurred.

Table 3.2: Weight loss of pine wood under various torrefaction conditions (wt.%).

Torrefaction Conditions	225 °C	250 °C	275 °C	300 °C
15 min	0.72	1.45	3.99	9.82
25 min	1.39	3.06	8.11	19.65
35 min	1.75	4.26	11.46	23.88

Temperature is a key factor affecting the wood decomposition. To better understand what is going on during torrefaction, the center temperature variation of the wood block is plotted in Figure 3.2. The indicated furnace temperature settings are generally about 5 °C higher than the steady state center temperature because of N_2 convection in the furnace tube. For 275 °C and 300 °C cases, the measured peak temperatures exceed the equilibrium temperature by about 3 °C and 11 °C respectively, indicating exothermic reactions which are caused by char formation and transformation. These torrefied wood samples were used to produce bio-oil. Charring during torrefaction is expected to reduce the carbon content of bio-oil.

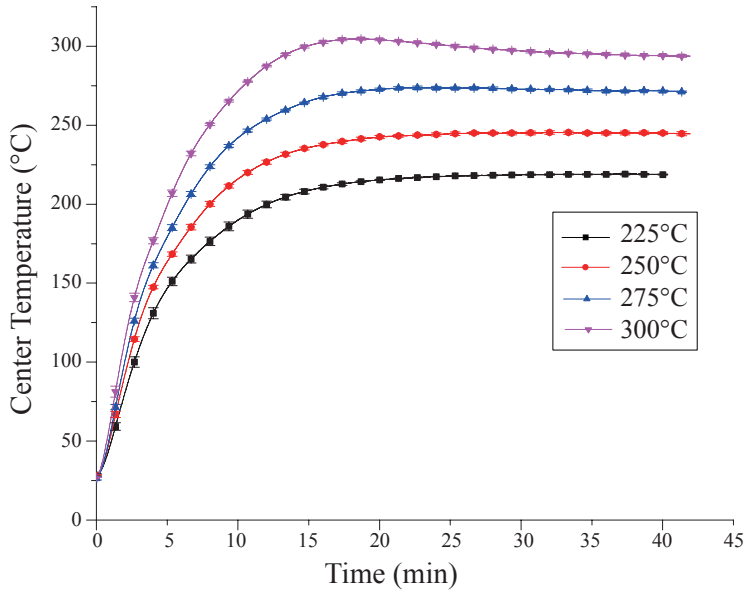

Figure 3.2: Center temperature profiles of pine wood particle during torrefaction processes. Torrefaction temperatures are 225 °C, 250 °C, 275 °C and 300 °C.

3.3.2 Pyrolysis Yield

The product yield is highly related to the torrefaction processes, as we can see from Table 3.3, where the yields of three pyrolysis products, liquid, char and gas, are listed. At the temperature of 225 °C and 250 °C, impact of torrefaction on pyrolysis products yield is almost negligible, which is in agreement with the results demonstrated in previous sections. Nevertheless, pyrolysis of pine wood torrefied at 275 °C and 300 °C implies that the total liquid yield drops and the yield of char rises with the increase of torrefaction temperature and time.

Specifically, Table 3.3 shows that the liquid yield changes between 53.12% and 38.01% under different torrefaction conditions, and the char yield varies between 22.07% and 32.46%. Gas yield is also enhanced as the torrefaction severity increases. This agrees with [37] and [46], who indicated that several organic condensable volatiles such as acetic acid, furfural and formic acid were formed, resulting in the decrease of condensable components during fast pyrolysis experiments. Besides, the carbonization of wood during torrefaction contributed to the increasing char yield. Pyrolysis

Table 3.3: Product yields from pyrolysis of torrefied wood (wt. % based on torrefied wood). Char yield based on dried wood is also calculated and listed in the bracket.

Run #	Torrefaction Conditions		Products Yield		
	Temperature (°C)	Time (min)	Liquid	Char	Gas
1	Raw biomass		53.12	22.07	24.81
2	225	15	54.09	22.41 (22.25)	23.50
3	225	25	53.57	22.38 (22.07)	24.05
4	225	35	53.26	22.23 (21.84)	24.51
5	250	15	53.57	22.52 (22.19)	23.91
6	250	25	52.95	22.96 (22.26)	24.75
7	250	35	52.18	23.18 (22.19)	24.46
8	275	15	51.58	23.12 (22.20)	25.30
9	275	25	48.92	25.28 (23.23)	25.80
10	275	35	47.64	26.34 (23.32)	26.02
11	300	15	50.70	24.72 (22.29)	24.58
12	300	25	43.63	29.64 (23.82)	26.73
13	300	35	38.01	32.46 (24.71)	29.53

of centimeter-scale pine wood particles reveals that the product yields remain almost the same for wood torrefied at 225 °C and 250 °C, but there exists a significant change when feedstock is torrefied at 275 °C and 300 °C. To find similarity between different torrefied conditions, it's worthwhile to compare the char yield based on the dried wood. In this case, char yield changes slightly from 22.07% (using raw materials) to 24.71% (using torrefied wood at 300 °C for 35 min), implying the effect of torrefaction on the overall char yield based on dried wood is not significant, and such a char yield is mostly determined by the pyrolysis conditions.

3.3.3 Profiles of Solid Mass Fraction

The solid mass fraction is defined in subsection 2.4.2. It is the ratio of measured sample weight during the experiments and the initial sample weight. Figure 3.3 shows the solid mass fraction profiles of various torrefied wood during pyrolysis. The corresponding measured particle center temperature is shown in Figure 3.5. In all

cases, a mild weight loss rate is observed at the beginning, indicating hemicellulose starts to decompose at low temperature. As temperature increases, the solid mass fraction decreases rapidly and the rate of weight loss remains approximately constant over a wide zone where the majority weight loss occurs. After the decomposition of most of hemicellulose and cellulose, the solid mass fraction changes slowly due to the pyrolysis of leftover lignin and finally becomes constant at the completion of wood pyrolysis.

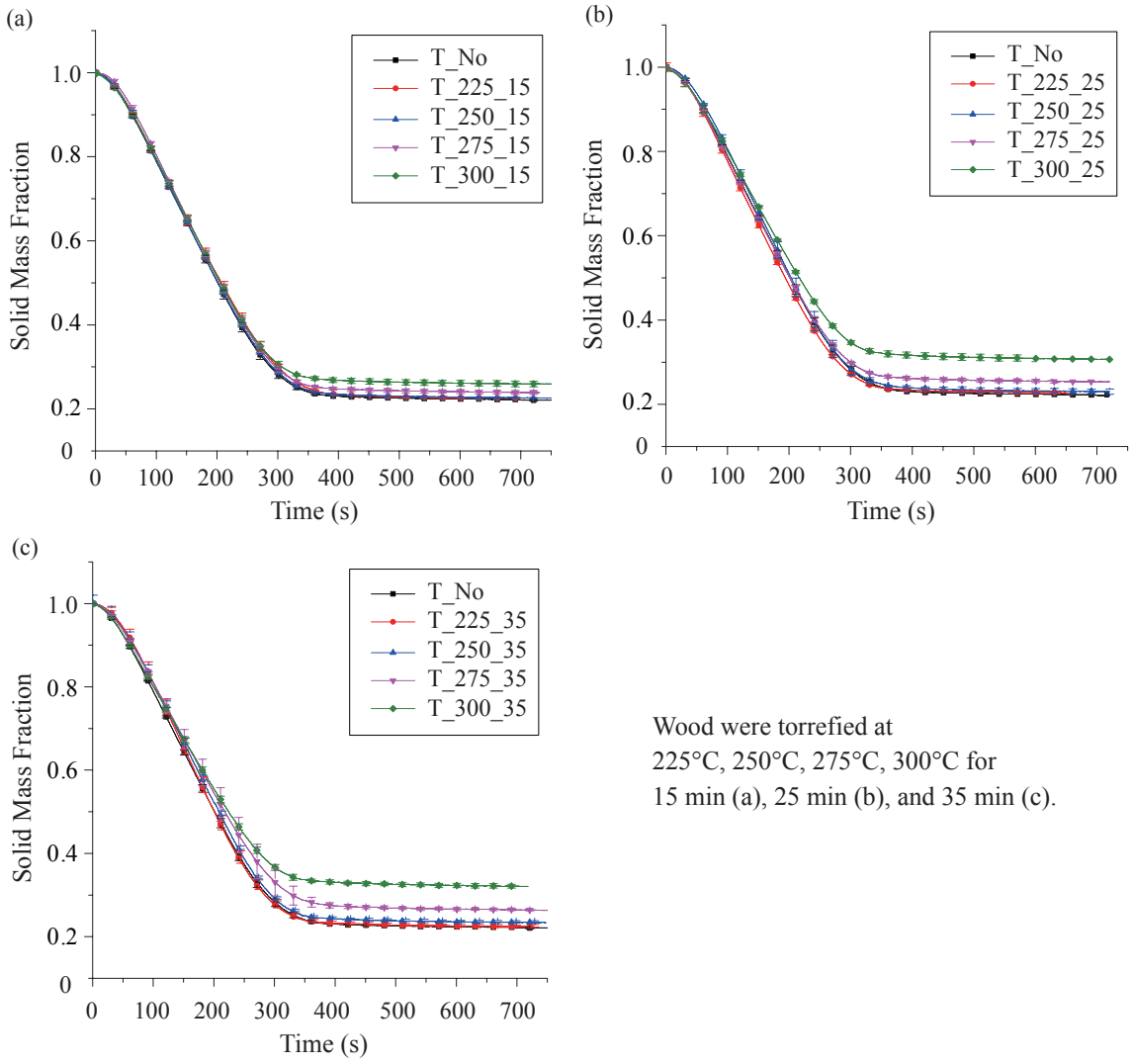

Figure 3.3: Solid mass fraction profiles of torrefied wood samples during pyrolysis processes.

In the same manner as the results shown in subsection 3.3.1, where there exists a

small difference between 225 °C and 250 °C, torrefaction at 225 °C and 250 °C also exerts a negligible influence on the weight loss features. However, after being torrefied at 275 °C and 300 °C, pine wood exhibits totally different profiles of solid mass fraction, as characterized by a lower weight loss rate and a higher leftover fraction as the torrefaction time increases. This phenomenon is not obvious in Figure 3.3(a) where torrefaction time is only 15 minutes, but it becomes clear when the torrefaction time is increased to 25 min and 35 minutes, especially for the 275 °C and 300 °C cases (Figure 3.3(b) and Figure 3.3(c)).

The conversion time, which is defined as the time when 95% of the total volatile matters is released, is presented in Figure 3.5. It varies between 300s and 330s and does not change too much with torrefaction conditions even in the cases where wood undergoes severe torrefaction at 300 °C. Di Blasi [13] reported the conversion time varied by a factor of ~ 2 between wood particle pyrolysis and wood block pyrolysis, which implies that particle size had a significant effect on the conversion time of wood pyrolysis. This is easy to understand since smaller particles are heated faster and the volatiles will be released sooner. In our study, however, the influence of torrefaction on the conversion time of large particle pyrolysis was not significant.

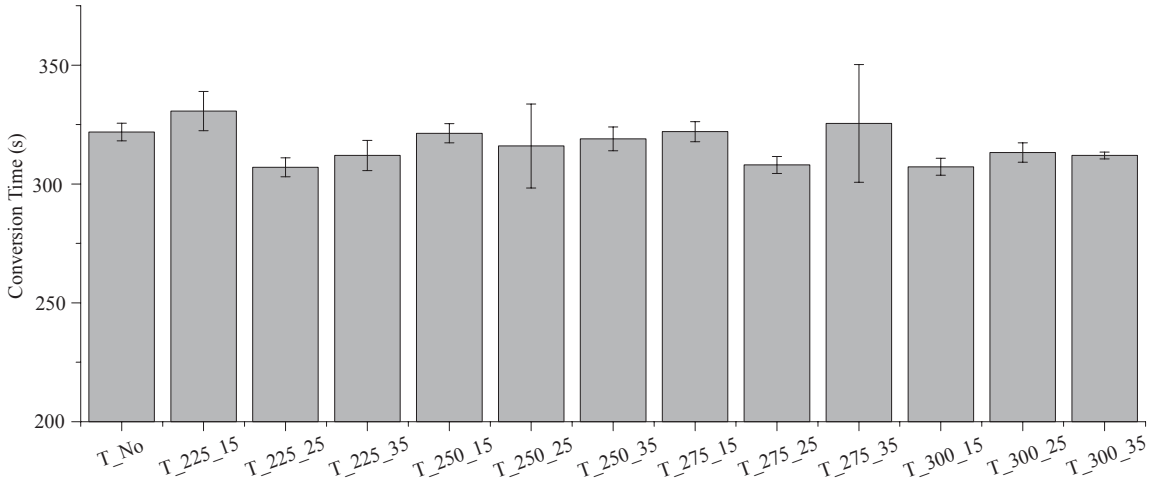

Figure 3.4: Conversion time of pyrolysis for wood samples torrefied under various conditions.

3.3.4 Profiles of Center Temperature

Temperature profiles at the center of pine wood during pyrolysis are shown in Figure 3.5. It's necessary to mention that wood was first placed in the cold zone of the reactor for a short time where the temperature gradually increased to 65 °C $\sim$ 80 °C before the wood was inserted into the hot reaction zone where the temperature was recorded. Pyrolysis of thermally thick wood particles has been studied by many investigators [13, 26, 47] and generally there exist four stages in the temperature profile during the pyrolysis process, which are also observed in this study. As we can see from Figure 3.5, the temperature rises almost linearly in the first stage. In the second stage, a temperature plateau appears. Then the temperature increases sharply and exceeds the furnace temperature. Finally, the center temperature drops and becomes stable, attaining thermal equilibrium with the furnace.

Torrefaction alters the composition and properties of biomass mostly by breaking down the reactive hemicellulose and decomposing cellulose, thus reducing hygroscopicity. However, for the pyrolysis of centimeter-scale pine wood particles, no marked difference was observed on the center temperature profile even though wood particles lost a significant amount of weight after severe torrefaction. Unlike fine particles which could be heated uniformly to furnace temperature instantly, centimeter-scale wood particles are thermally thick. During pyrolysis of thermally thick particles, the temperature is controlled by the energy variation in the control volume through thermal conduction, gas flow convection and heat generation from pyrolysis reactions. After torrefaction, wood particles become more porous and the structures of hemicellulose and cellulose are damaged, which might lead to the decrease of overall thermal conductivity and a lower heat transfer rate. On the other hand, the specific heat capacity of wood may also drop since torrefaction is in favor of char formation and char has a lower heat capacity than virgin wood, thus wood would be heated up faster. These two aspects explain why there is no difference in the center temperature

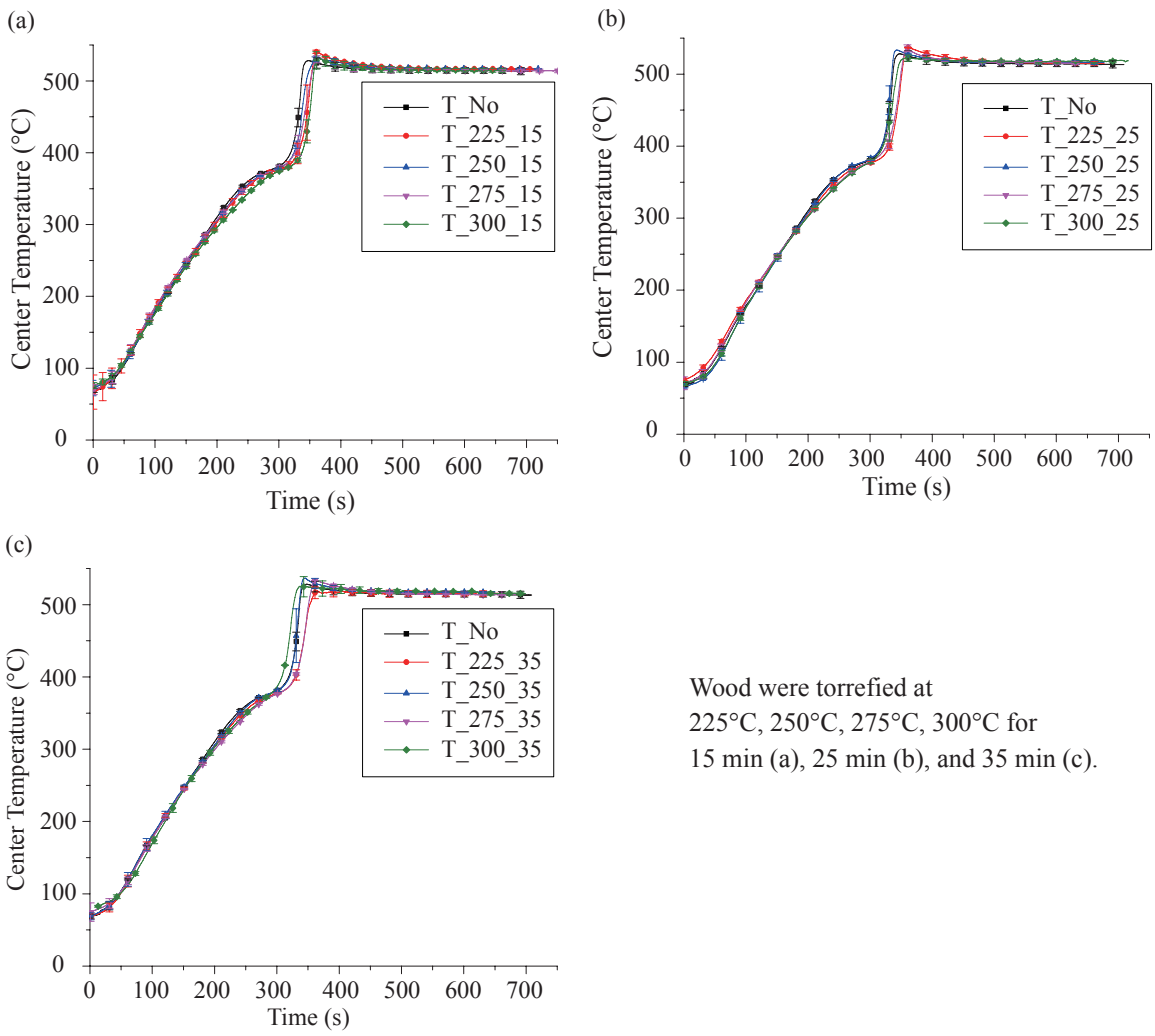

Figure 3.5: Center temperature profiles of torrefied wood samples during pyrolysis processes.

profile during the first stage where temperature increases mainly because of thermal conduction. As seen in Figure 3.5, temperature increases sharply at the end of pyrolysis while the mass profile stays almost constant, thus the exothermic reactions are not contributed by the lignin decomposition. Instead, the exothermic conversion of intermediate solid to char is responsible for the center temperature peak. The fact that the center temperature peak is not significantly affected by torrefaction implies that the char formation process during pyrolysis is not affected by torrefaction.

Basile et al. [48] studied the thermal effects during biomass pyrolysis and con-

cluded that the secondary volatile-solid reactions are responsible for the exothermic behavior. Increasing particle size will enhance the secondary decomposition of volatiles and increase the char yield, thus exothermic behavior becomes more obvious. It should be stated that for all the cases, the mass fraction remains almost constant when the aforementioned sharp peak in temperature is observed. This leads to the inference that the large heat release does not come from chemical reactions requiring high mass transfer rates. The phase transformation of solid from the amorphous state to the crystalline state is generally associated with an energy release [49, 50], which could possibly result in an increase of temperature. Thus it is suspected that the conversion of intermediate solid to char is actually the change of carbon solid from high free energy amorphous structure to a low free energy stable structure. Nevertheless, this hypothesis requires further experimental and thermodynamic analysis.

The heat of reaction during the biomass pyrolysis comes from two sources, the endothermic reaction that absorbs heat to convert virgin wood to volatiles and intermediate solid, and the exothermic reactions of secondary decompositions. Both reactions occur simultaneously during the pyrolysis process. When the particle temperature is relatively low and the virgin wood is not fully decomposed, endothermic reactions are dominant and the overall heat of reaction is positive. As the temperature increases, exothermic reactions are enhanced. The reaction heat could even become negative at high temperatures in some cases, leading to the possibility of thermal runaway or thermal explosion [51]. Thermal explosion describes a process accelerated by increased temperature and the exothermic reaction goes out of control: the reaction rate increases due to an increasing temperature, causing a further rapid increase in temperature and hence a further increase in the reaction rate. This phenomenon may also cause the temperature in the center to be greater than the surface temperature at the end of the pyrolysis process. The heat that is released from exothermic reactions can be carried away by thermal conduction and gas convection. It is difficult for the

heat to build up inside the biomass particle, with the exception of the center, where the thermal condition is adiabatic and heat is easier to accumulate. Thus, thermal explosion is more likely to take place in the central portion of the particle. This statement is further supported by [52], which argues that the temperature profile in the particle center has an obvious sharp increase while that in the other locations is smooth.

3.3.5 Pyrolysis Products Characterization and Quantification

To further understand the effect of torrefaction on centimeter-scale pine wood pyrolysis, the compositions of bio-oil were characterized by GC-MS and about 70 chemical components were identified by searching the NIST library. The changes of functional group compositions in bio-oil at different torrefaction conditions are shown in Figure 3.6 where chemicals are classified into 9 categories, namely ketones, acids, guaiacols, laevoglucose, aldehydes, phenols, furans, catechol and others. Table 3.4 provides additional details about the major compounds. Of all the chemical functional groups, ketones contribute to the largest amount of chemicals in the bio-oil, ranging from 30 - 36 area%, followed by acids and guaiacols. The differences of chemicals content between various conditions are generally small, and it seems that torrefaction mainly alters the quantities of same bio-oil components instead of creating new chemical species such as hydrocarbons which are important for transportation fuels. However, the amount of acids especially that of acetic acid, is obviously deceased after wood was torrefied under 275 °C and 300 °C, indicating torrefaction is helpful in reducing the acidity of bio-oil. Besides, phenols from pyrolysis of torrefied pine wood increase to 6.08 area % compared with a value of 4.14 area % when there's no torrefaction impact. The amount of guaiacols also decreases with increase of torrefaction intensity. Figure 3.6 and Table 3.4 also imply that torrefying pine wood at 225 °C and 250 °C has little influence on the pyrolysis products.

Table 3.4: Main species in bio-oil obtained from the pyrolysis of pine wood particles as determined by GC/MS peak areas (%).

Compounds	Raw Biomass	225 °C			250 °C			275 °C			300 °C		
		15min	25min	35min	15min	25min	35min	15min	25min	35min	15min	25min	35min
2-Amino-1,3-Propanediol	1.57	1.25	1.75	1.59	1.72	1.67	1.76	1.62	1.56	1.49	1.5	1.51	1.34
2,3-Butaanedione	3.37	2.69	2.84	2.18	2.88	2.68	4.11	2.71	2.41	2.78	2.51	2.61	2.36
Acetic acid	13.46	14.23	13.86	13.22	13.12	12.98	12.86	13.74	12.44	11.71	11.83	11.17	10.70
2-Propanone, 1-hydroxy-	11.06	10.26	10.63	10.18	10.60	11.29	11.64	11.19	10.54	10.91	12.00	12.50	10.83
Acetic acid, methyl ester	3.64	3.34	3.74	3.71	3.75	3.75	4.06	3.82	3.54	3.41	3.70	3.72	3.12
Succindialdehyde	2.28	2.09	2.24	2.33	2.15	2.15	2.35	2.24	2.10	2.21	2.11	2.23	2.38
Pyruvic acid, methyl ester	2.93	2.67	3.00	2.81	2.94	2.92	3.10	3.11	2.79	2.75	3.05	2.51	2.57
1H-Imidazole,4,5-dimethyl-	3.28	2.90	3.38	3.07	3.22	3.08	3.32	3.26	3.08	3.34	2.86	3.00	3.04
Butanal,2-ethyl-	2.19	2.17	2.24	2.32	2.21	2.24	2.15	2.44	2.29	2.23	2.29	2.44	2.19
2-Propanone, 1-(acetyloxy)-	1.21	1.13	1.21	1.22	1.13	1.07	1.17	1.37	1.12	1.14	1.33	1.22	1.12
2(5H)-Furanone	1.81	1.19	1.33	1.77	1.73	1.74	1.8	1.83	1.97	1.84	1.79	1.08	1.77
2-Hydroxy-2-cyclopenten-1-one	3.09	2.85	3.11	3.13	3.13	3.03	3.23	3.24	3.24	3.17	3.05	3.09	3.09
Furfural, 5-methyl-	1.49	1.64	1.55	1.52	1.38	1.59	1.56	1.71	1.82	1.61	1.76	1.78	1.88
Corylone	1.91	1.82	1.82	1.95	1.95	1.93	2.02	2.08	1.96	2.29	2.04	2.33	2.47
Phenol, 2-methyl-	0.94	1.11	0.87	1.11	1.06	1.00	1.01	1.09	1.13	1.27	1.16	1.15	1.53
Phenol, 3-methyl-	1.29	1.61	1.32	1.16	1.31	1.39	1.41	1.37	1.35	1.76	1.50	1.76	1.79
Phenol, 2-methoxy-	2.69	2.80	2.72	2.65	2.75	2.88	2.99	2.90	2.67	3.22	2.95	3.24	3.00
Cyclopropyl carbinol	2.08	2.03	1.93	2.19	2.05	2.14	2.02	2.18	2.98	2.78	1.86	1.92	1.85
4-Methyl-2-oxo-pentaneitrile	1.84	1.72	1.74	1.66	1.86	1.92	2.16	1.88	2.18	2.25	2.03	2.19	2.06
Creosol	4.05	4.13	3.90	3.89	5.21	4.18	4.34	4.29	4.05	4.77	4.35	4.81	4.55
2,3-Anhydro-d-mannosan	1.45	1.42	1.56	2.18	1.60	1.88	2.40	1.79	1.60	1.59	1.67	1.94	2.11
Phenol, 4-ethyl-2-methoxy-	1.54	1.53	1.23	1.55	1.47	1.39	1.51	1.51	1.37	1.69	1.28	1.51	1.88
2-Mehoxy-4-vinylphenol	1.49	1.47	1.53	1.69	1.53	1.69	1.47	1.53	1.20	1.27	1.11	1.05	0.81
Phenol, 2-methoxy-4-propenyl-	2.35	2.21	2.19	2.15	2.27	2.12	2.00	1.88	1.36	1.29	0.98	0.74	0.59
1,6-anhydro-β-D-Glucose	5.23	6.80	6.57	6.44	5.81	6.86	5.69	5.24	7.25	7.42	6.65	5.90	9.15

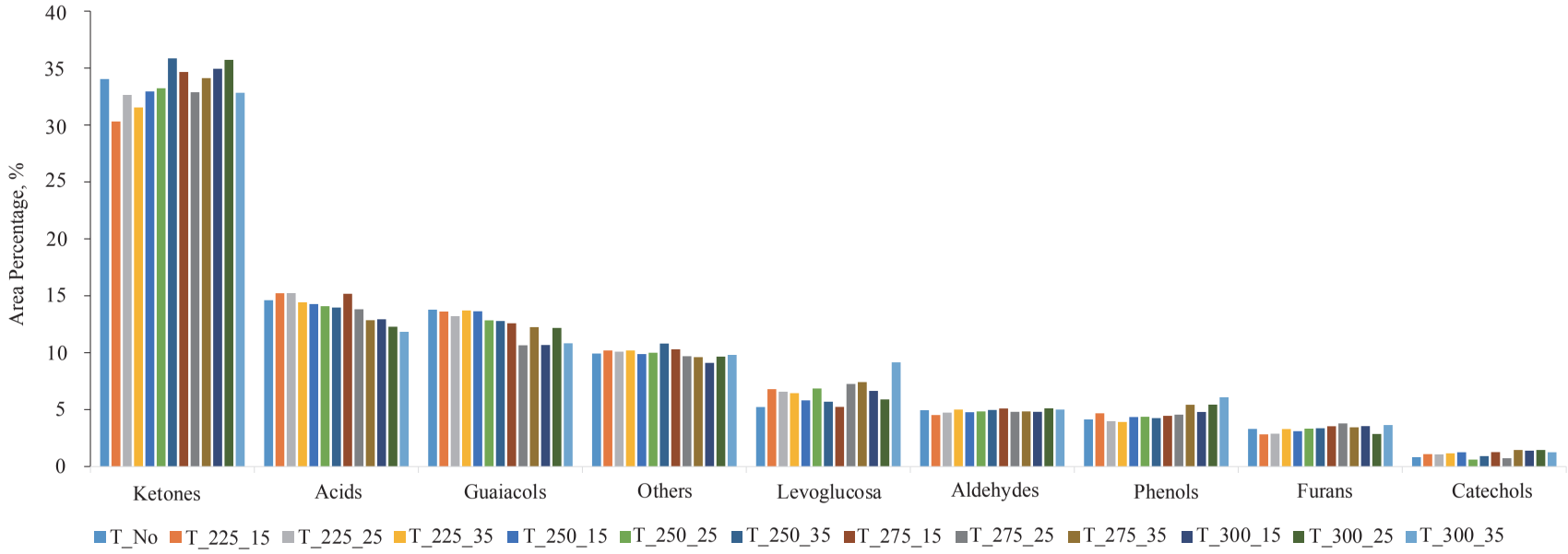

Figure 3.6: Variation of function groups in bio-oils produced from pyrolysis of torrefied wood.

Both Meng [41] and Ren [42] stated that pyrolysis of torrefied biomass gave quality-improved products and recommended torrefaction as a potential pretreatment for bio-oil production. However, this study with centimeter-scale pine wood particles shows that the effect of torrefaction on the product of pyrolysis is small. The reason accounting for the difference between the work of Meng [41], Ren [42] and ours may come from the size of biomass particles used as feedstock. There will be temperature gradient inside a particle during heating process and this phenomenon will be enhanced when the particle size becomes larger. As can be seen from Figure 3.2 when wood is torrefied at 275 °C, the center temperature is lower than 250 °C for the first 10 min, then it increases gradually to 275 °C, which means wood is actually heated at low temperature for a long time because of the slow heating processes. Since we already showed that torrefaction at low temperatures such as 225 °C and 250 °C has little effect on pyrolysis of centimeter-scale wood particles, the slow heating at 275 °C or 300 °C may not benefit the wood as expected.

Torrefaction can modify the composition and structure of biomass and produces torrefied wood with less hemicelluloses and more cellulose and lignin residues. Torrefied wood generally has an increased carbon content and decreased oxygen content, and this is easy to understand considering the fact that wood will become char if torrefied for infinite time. Even though this study also implies that torrefaction can be used as a pretreatment of biomass for bio-oil production since the content of acid does decrease, we should also realize that the improvement of bio-oil quality is achieved with the sacrifice of bio-oil yield.

3.4 Conclusion

Pyrolysis of torrefied wood provides potential for high quality bio-oil synthesis. In this chapter, the effect of torrefaction on pyrolysis of centimeter-scale pine wood was studied experimentally. Weight loss of pine wood after torrefaction experiences little

change at 225 °C and 250 °C but increases significantly at 275 °C and 300 °C, indicating that severe decompositions occur at high torrefaction temperature. Exothermic reactions start to occur when wood is torrefied at 275 °C and 300 °C, and this may be related with char formation and transformation. Pine wood exhibits a lower weight loss rate and a higher leftover char fraction during the pyrolysis process after wood is torrefied at 275 °C and 300 °C, and the effect of torrefaction on center temperature profile is not significant which may be because of the changes in wood properties after torrefaction. Besides, the conversion time of large particle pyrolysis was not remarkably affected by torrefaction; instead, it is related to the size of the biomass particle. Product yields are highly related to the torrefaction processes, and liquid yield decreases with increasing torrefaction intensity while char yield increases. Based on GC-MS analysis, the chemical composition of bio-oil produced from pyrolysis of torrefied wood shows a decrease of acid content, but overall the effect of torrefaction was not remarkable when large biomass particles are used for pyrolysis, and new species are not detected. It appears that the mechanism of torrefaction processes needs to be further studied with regards to hemicellulose, cellulose and lignin. Other techniques such as catalytic pyrolysis need to be investigated to optimize pyrolysis product from centimeter-scale wood particles.

CHAPTER IV

Catalytic Pyrolysis of Centimeter-scale Biomass Particles

4.1 Introduction

Catalytic pyrolysis is an effective technique to enhance the properties of bio-oil by removing oxygenated compounds as H_2O, CO, and CO_2. Based on the operating conditions, catalytic upgrading genereally takes place via either hydrodeoxygenation (HDO) or zeolite cracking. HDO is a hydrogenolysis process that removes oxygen from bio-oil by cleaving carbon-oxygen bonds with hydrogen in the presence of a catalyst [53]. CO_2 and H_2O are produced during this process, partially eliminating oxygen from the final product. Nevertheless, HDO is not a feasible process to utilize the biomass distributed in vast and remote locations as it requires large quantities of hydrogen at high pressures (70 to 300 bar). The second approach to deoxygenating bio-oil is catalytic cracking which is performed by passing bio-oil vapors through high temperature catalyst beds such as zeolites or mixing catalysts with fine biomass particles in fluidized bed reactors. As opposed to hydrodeoxygenation, catalytic cracking is conducted under atmospheric pressure without adding hydrogen and it gives a high energy density product with substantial aromatic content [54].

Zeolites are aluminosilicate minerals with microporous structures. Extensive work

has been carried out on using zeolites to upgrade bio-oil into hydrocarbon fuels. Huang et al. [55] developed a two-stage catalytic pyrolysis reactor into convert pine sawdust to advanced biofuel over HZSM-5. By characterizing the physical properties of bio-oil, such as water content, density, viscosity, pH, and higher heating value (HHV), they demonstrated that HZSM-5 was beneficial in achieving low viscosity and high HHV bio-oils. Muley et al. [56] conducted catalytic upgrading of pinewood sawdust using an induction heating reactor. In their work, three different catalyst-to-biomass ratios were studied and the effect of catalyst bed temperature was also investigated. It was found that higher-quality bio-oil, with increased yield of aromatic hydrocarbons and reduced oxygen content, was obtained with an induction heating reactor as compared to one with conventional heating. Williams and Nugranad [57] compared the products from non-catalytic and catalytic pyrolysis of rice husk and concluded that the effect of the catalyst was the conversion of oxygen in the pyrolysis oil to H_2O, CO and CO_2 at various temperatures. The catalyzed bio-oils had markedly higher content of single ring hydrocarbons and PAH than non-catalytic biomass pyrolysis oils, and concentration of the aromatic and polycyclic species increased with increasing catalyst temperatures. Yildiz et al. investigated the effect of successive catalyst regeneration on the fast pyrolysis of pine wood [58]. Stefanidis studied fifteen different catalysts for the in-situ upgrading of biomass pyrolysis vapors [59]. Many other catalysts like MgO [60], NiO/AC [61], K_2CO_3 [62], γ-Al_2O_3 [63], ZnO [64], CaO [65] and transition metal-modified ZSM-5 zeolites [66] have also been used in catalytic cracking to upgrade pyrolysis oil to advanced hydrocarbon fuels.

Zeolite catalysts show promising performance in the deoxygenation of bio-oil. However, most studies on catalytic pyrolysis have focused on small particles where the heating up of the biomass can be assumed to be instantaneous. The conditions encountered in industrial process are different as thermally thick particles are often used [67]. In Chapter III, the thermal treatment of the feedstock by torrefaction was

not sufficient enough to provide novel species in the bio-oil from biomass pyrolysis, it is therefore of significant interest to investigate the catalytic pyrolysis of centimeter-scale wood biomass particles by passing the pyrolysis vapors through the hot catalyst. In this chapter, the effect of catalyst temperature and catalyst regeneration on pyrolysis products is also investigated.

4.2 Materials and Methods

4.2.1 Materials

The same pine wood particles as described in Chapter III were used as feedstock for catalytic pyrolysis. The catalyst, ZSM-5 column (SiO_2/Al_2O_3 molar ratio = 38) with a diameter of 1 mm, was purchased from ACS Materials and prepared to have a length of 3 $\sim$ 5mm. The catalyst was calcined at 550 °C in the presence of air for 5 hours before being used.

4.2.2 Experiment Apparatus

Experiments were carried out in the two stage pyrolysis system as shown in Figure 4.1. It was modified from the one used in the previous chapter. The system consists of a pyrolysis reactor, a catalyst bed, a condensation system, and a gas collection unit. The catalyst bed is 23 mm in diameter and 100 mm in height and the temperature is controlled by the heating tape. It is connected to the pyrolysis reactor so that the pyrolysis gases are passed directly to the heated catalyst for further cracking. ZSM-5 catalyst is supported by a stainless steel mesh in the catalyst bed and 28 g of catalyst is loaded in each test (total height of catalyst is around 80 mm). The temperatures of the pyrolysis reactor and catalyst bed are monitored by K-type thermocouples. The condensation system includes a jacketed condenser cooled by ice water (where 80-85% of the liquid was collected and chemically analyzed) and a

cotton wool filter. After going through a gas sampling tube, the uncondensed gas was collected in a Tedlar sampling bag. Nitrogen was used as the carrying gas with a mass flow rate of 0.05 g/s.

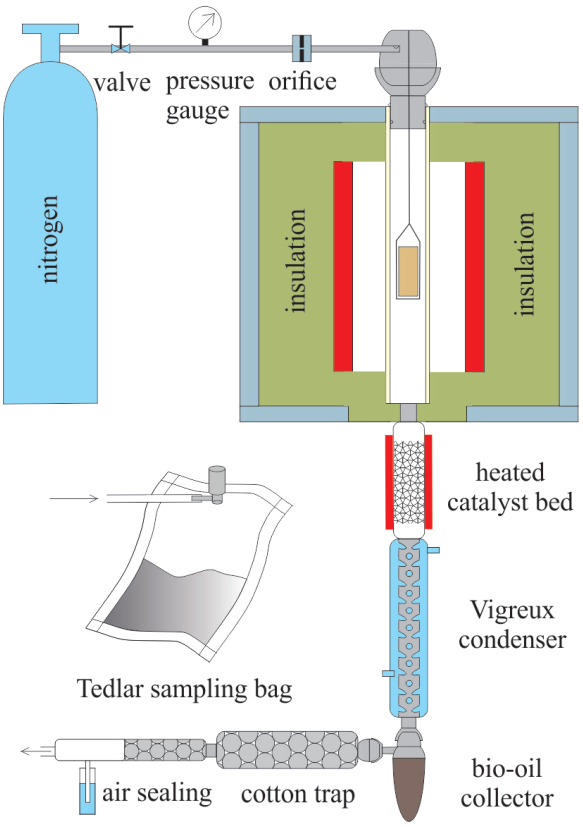

Figure 4.1: Schematic of the experiment apparatus.

The temperature of the pyrolysis reactor was maintained at 500 °C for all the experiments, and the catalyst temperature was set to 400 °C, 450 °C, 500 °C, 550 °C, and 600 °C for various cases. After the furnace and catalyst bed were heated to the desired temperatures and reached a steady state, the biomass particle, which was held in a steel wire holder, was first put at the colder zone of the furnace for two min to allow the nitrogen to purge the air that may have leaked in while feeding in the biomass; then it was immediately inserted to the center of the furnace for the chemical reactions to begin. An experiment without the catalyst bed was also carried out to act as the baseline for comparison purposes. In each case, six particles (∼72

g) were used for pyrolysis to ensure there was enough liquid collected. To investigate the effect of catalyst regeneration on biomass pyrolysis, the catalyst was regenerated by heating at 550°C for 5 hours in the presence of air. Then the regenerated catalyst was used again for pyrolysis and the catalyst bed temperature was set at 500 °C. The liquid yield was calculated by weighing all the condensable products trapped in the condensation system. Char yield was measured by weighing the remaining solid after experiment. The weight increase of catalyst bed accounted for the yield of catalyst coke, and gas yield was determined by mass balance. In order to limit experiment error, each case was performed twice and averaged values have been reported.

4.2.3 Characterization of Pyrolysis Products

The liquid derived from catalytic pyrolysis contains two distinct layers: an aqueous layer and an organic layer, and they were further separated using dichloromethane with a mass ratio of 4: 1 between pyrolysis liquid and dichloromethane. The water content in both phases was analyzed by Mettler DL 35 Karl Fischer titrator. The organic phase of the bio-oil was then dissolved in methanol with a mass ratio of 1:4, and characterized by the Shimadzu GC/MS-QP 2010. Configuration of the GC-MS was discussed in subsection 3.2.3. A volume of 1 μL liquid sample was injected in split mode (split ratio 20:1).

The gas collected in the Tedlar bag was identified and quantified using packed column gas chromatography (GC). Hydrocarbons from C_1 to C_3 were analyzed using a Perkin Elmer Autosystem with flame ionization detector (FID) and a Varian CP-AL_2O_3/Na_2SO_4 capillary column (25 m $\times$ 0.55 mm $\times$ 10 μm). Column temperature was 40°C for 2 min, then raised to 160 °C at a rate of 6 °C/min and stayed at this value for 3 min. The detector temperature was set at 300 °C. Carbon monoxide (CO) and carbon dioxide (CO_2) were measured by a Perkin Elmer Clarus 500 with a thermal conductivity detector (TCD) and a Restek ShinCarbon ST packed column

(2 m × 1 mm × N/A). The column has the same temperature profile as above.

4.3 Results and Discussion

4.3.1 Product Yields

The product yields (wt.% based on raw biomass) of liquid, gas, char, and coke from the pyrolysis of pine wood particles at the temperature of 500 °C are shown in Figure 4.2. The run with catalyst from the first regeneration is denoted as R1, with subsequent cycles denoted as R2, R3, and R4. For the pyrolysis in the absence of catalyst (used as reference case and denoted as "NC"), the yield of liquid was 56.32%, with a char yield of 23.38% and gas yield of 20.29%.

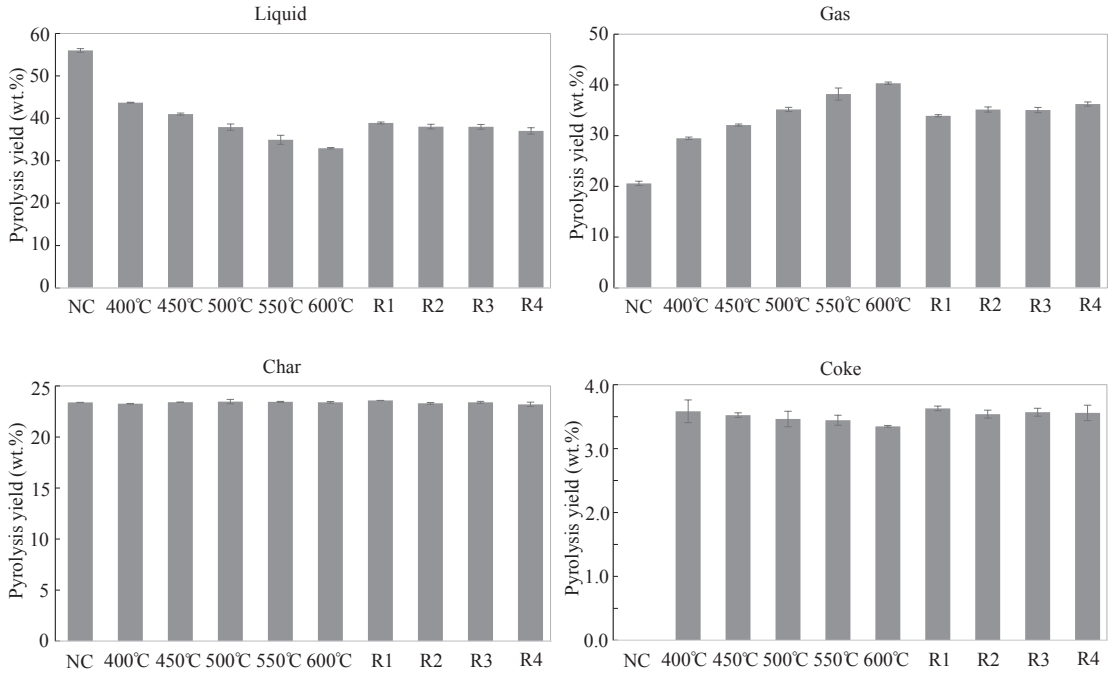

Figure 4.2: Effect of catalyst temperature (400 °C, 450 °C, 500 °C, 550 °C, and 600 °C) and catalyst regeneration on the product yields (wt.%) from the pyrolysis of pine wood at 500 °C. NC represents non-catalytic pyrolysis and is used as reference. R1 is the case with the first regeneration of catalyst, with subsequent regeneration represented by R2, R3, and R4.

As shown in Figure 4.2, in comparison to the case with no catalytic treatment,

there is an obvious change of the liquid and gas yields from catalytic pyrolysis. The increase of gaseous products is mainly caused by the secondary cracking of the pyrolysis vapors at high temperature, and the lower liquid yields can be attributed to the fact that oxygen is removed as water, CO_2, CO, and other species during catalytic upgrading. It is apparent that the catalyst temperature has a noteworthy effect on the product yields. Specifically, the total liquid yield falls from 43.69% to 32.94% and the yield of gaseous products rises from 29.49% to 40.34% as the catalyst bed temperature increases from 400 °C to 600 °C. The yield of char is not affected by the catalytic treatment due to the unchanged pyrolysis conditions for the fixed bed reactor. The coke formation on zeolite catalyst shows a marginal decrease with increasing catalyst temperature, from 3.5% at 400 °C to 3.3% at 600 °C. Overall, the coke formation is not significantly affected by catalyst temperature in the current study.

Figure 4.2 also shows the pyrolysis yields using regenerated catalyst. Zeolite ZSM-5 has a strong acidity and high activity to convert the oxygenated compounds in the bio-oil to small molecules by dehydration, deoxygenation, and cracking. Nevertheless, the catalyst is deactivated very soon due to carbon deposition during the zeolite cracking reactions. Regeneration of catalyst is achieved by heating the deactivated catalyst at 550 °C in the presence of air in order to remove the coke deposit and regain the surface area and activity. There is little change in gas, char, and coke yields for cases with regenerated catalyst in comparison to the case with fresh catalyst. There exists a small declining trend in liquid yield and an increasing trend in gas yield for progressive regenerations, which is mainly caused by the decline of organic content in the bio-oil (Table 4.1). The decrease of organic yields is consistent with the results of Yildiz et al. [58] who found that catalyst surface area decreases after the regeneration. Even though catalyst activity was recovered to a large extent, partial deactivation of the catalyst still occurs.

Table 4.1: Water and organic yields for non-catalytic and catalytic pyrolysis with different treatment (wt.% based on biomass).

	NC	400 °C	450 °C	500 °C	550 °C	600 °C	R1	R2	R3	R4
Water	22.14	27.67	27.16	28.09	27.34	27.41	28.61	28.69	28.79	28.72
Organic	33.88	16.02	13.83	9.83	7.59	5.53	10.29	9.34	9.21	8.30

Both the oil and aqueous phases in the bio-oil are analyzed by Karl Fischer Titration to determine the total organic and water contents in the liquid, as shown in Table 4.1. The yield of organic content drops from 33.88% to 16.02% after catalyst is introduced at 400 °C and is reduced further with the increasing catalyst temperature. This is an expected finding since the catalyst upgrades the bio-oil by removing the oxygen content of the organics, resulting in a low net organic yield. H_2O is one of the primary products of bio-oil oxygen removal, leading to a higher water content for cases with catalytic pyrolysis than the non-catalytic case. It is also interesting to note that the water yield remains almost constant for different catalyst treatments while the organic content varies, which leads to the conclusion that the water formation reactions during the catalytic upgrading process are not significantly affected by the catalyst temperature and regeneration in the above range.

4.3.2 Gas Analysis

Figure 4.3 shows the composition of gases from the pyrolysis of pine wood particles at 500 °C with and without ZSM-5 catalyst. The data is obtained by correlating the total gas yields as seen in Figure 4.2 and the relative mass fraction of each gas species measured by the GCs. Thus it represents the mass of gas produced per unit mass of biomass during the experiment. The presence of the catalyst results in a large increase of the gas yield (Figure 4.2), leading to a marked yield increase of all gas species compared to non-catalytic case. The gases consisted mainly of carbon monoxide (CO), carbon dioxide (CO_2), with lower concentrations of alkanes, methane (CH_4), ethane (C_2H_6), and propane (C_3H_8), and alkene species such as ethylene (C_2H_4) and

propene (C_3H_6). Due to equipment limitations, hydrogen is not detected, but its mass fraction is assumed to be very small as per findings of previous studies [55, 58].

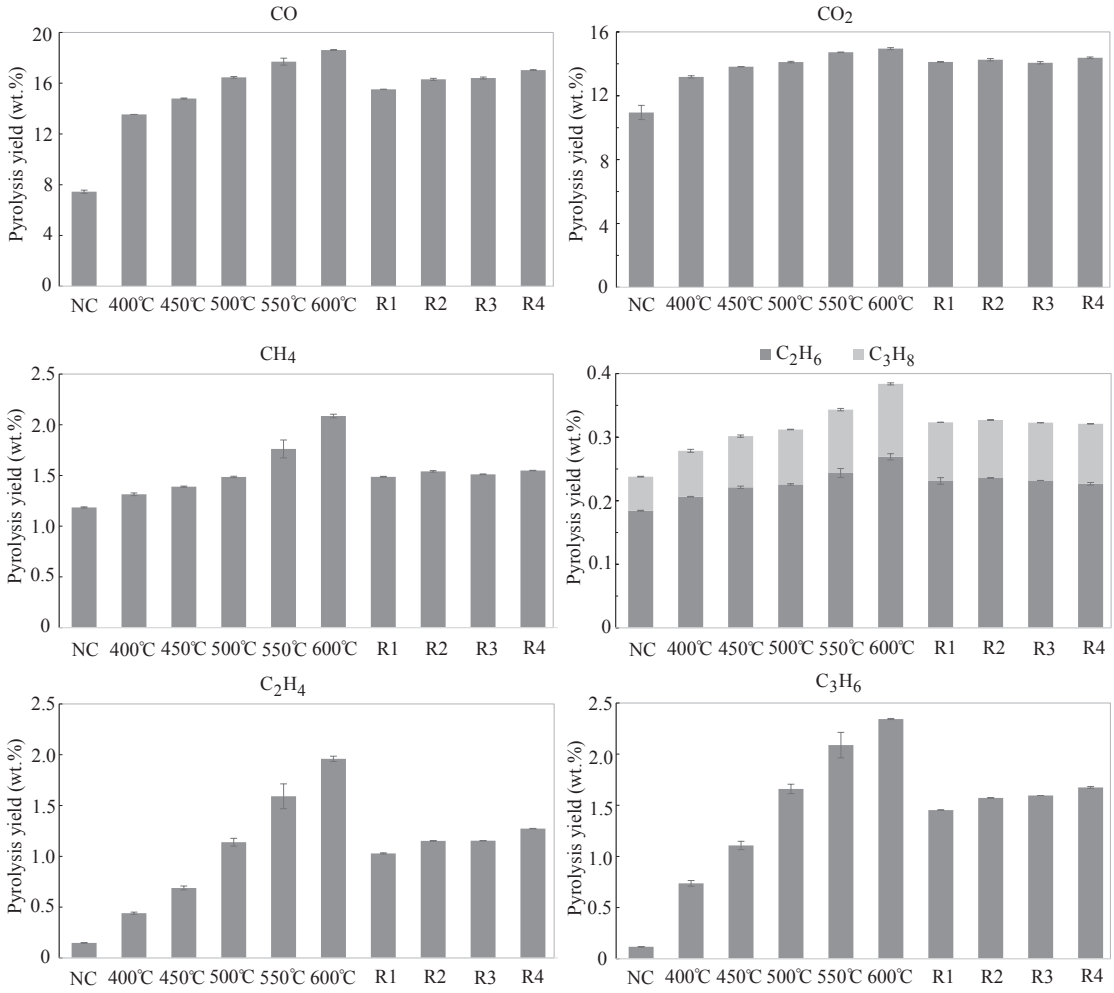

Figure 4.3: Gas composition for the non-catalytic and catalytic pyrolysis of pine wood particles at 500 °C (wt.%).

CO and CO_2 are the most abundant species in the gas products and there is an obvious increase in their yields with increasing catalyst temperatures. In the catalytic upgrading process, oxygen is removed from the pyrolysis vapors primarily in the form of CO, CO_2, and H_2O. The change in water content is very small in catalytic pyrolysis (Table 4.1), therefore, the conversion of the oxygen is mainly to CO and CO_2 as the catalyst temperature increases. The yield of CO is only 7.45% for non-catalytic pyrolysis case, while it increases dramatically to 13.54% for catalyst at

400 °C, and reaches 18.61% when the catalyst temperature is 600 °C. The increase in CO_2 production is relatively low as compared to CO. In catalytic bio-oil upgrading, decarbonylation (CO production) and decarboxylation (CO_2 production) are two of the most significant reaction mechanisms [53]. It appears that, in catalytic pyrolysis, decarbonylation reaction is more dominant than the decarboxylation. The alkene gas species experience a significant increase for the catalytic upgrading process. For instance, the yield of C_3H_6 increases by about 18 times from 0.12% (NC) to 2.34% (600°C). These small alkene molecules can be formed from the cracking, decarbonylation, decarboxylation of furan compounds and can further react on the strong acid sites of zeolite to form the aromatic hydrocarbons. On the other hand, the influence of catalyst regeneration on the gas yields is not very obvious. The changes of CO_2 and alkane species are negligible for successive regeneration cycles while the yields of CO, C_2H_4, and C_3H_6 undergo a marginal increase with after the catalyst is recycled.

4.3.3 Bio-oil Analysis

Figure 4.4 presents the relative chemical composition of the organic content in bio-oil. The organic compounds were identified and quantified using GC-MS and classified into 8 functional groups: aromatic hydrocarbons, PAH, phenols, ketones, acids, furans, acids, esters, and others. Appendix C shows the details of the most prevalent individual compounds including both hydrocarbon and oxygenated species characterized by GC-MS. After catalyst is introduced, many novel compounds are produced, including single ring aromatics and PAH which were not detected in the pyrolysis oil from torrefied biomass. The role of zeolite catalyst is to remove the oxygen contents in the bio-oil to produce hydrocarbon fuels. Thus, catalytic pyrolysis is a more effective technique than torrefaction in achieving hydrocarbon fuels from centimeter-scale biomass particles.

As shown in Figure 4.4, no hydrocarbon species were detected in the bio-oil from

non-catalytic pyrolysis of centimeter-scale pine wood particles. However, after catalysis, there was a marked increase in the concentration of single ring aromatic compounds and PAH. The single ring aromatic compounds mainly consist of toluene, o-Xylene, mesitylene, indane, indene, 1H-indene, etc. The majority of PAH are alkylated derivatives of naphthalene such as Naphthalene, 2, 3-dimethyl-, and Naphthalene, 2-methyl-. The relative content of PAH has an obvious increase as the catalyst temperature is increased from 400 °C to 600 °C, and the single ring compounds increase initially then decrease slightly. In comparison with temperature, the effect of catalyst regeneration on hydrocarbon species is not significant.

The aromatic hydrocarbons and PAH detected in the bio-oil from catalytic pyrolysis may be formed through two chemical mechanisms [57]. First, hydrocarbon products of low molecular weight are produced from catalytic pyrolysis and subsequently reacted to form aromatics via polymerization and aromatization. As depicted in Figure 4.3, an increasing amount of alkene gases such as C_2H_4 and C_3H_6 are produced as the catalyst temperature increases, which is consistent with the increasing relative concentration of hydrocarbon species; thus it is possible that a large amount of alkene gases are first produced from catalytic pyrolysis, then react to form aromatic hydrocarbons and PAH. Ono et al. [68] studied the conversion of propylene and 1-butene over ZSM-5 and found that a large quantity of aromatics were produced. Alternatively, the oxygenated compounds found in the pyrolysis vapor could be directly converted to aromatic compounds by de-oxygenation followed by aromatization when the vapor passes through the hot catalyst bed. The acid in the bio-oil is mainly acetic acid, and as depicted in Figure 4.4, the amount of acids in the bio-oil experiences a notable decrease after catalysis, and these acetic acids may convert to hydrocarbon species. Indeed, Chen et al. investigated the catalysis of acetic acids in a fluidized bed system and found aromatics in the products [69].

Even though catalytic pyrolysis of centimeter-scale pine wood particles signifi-

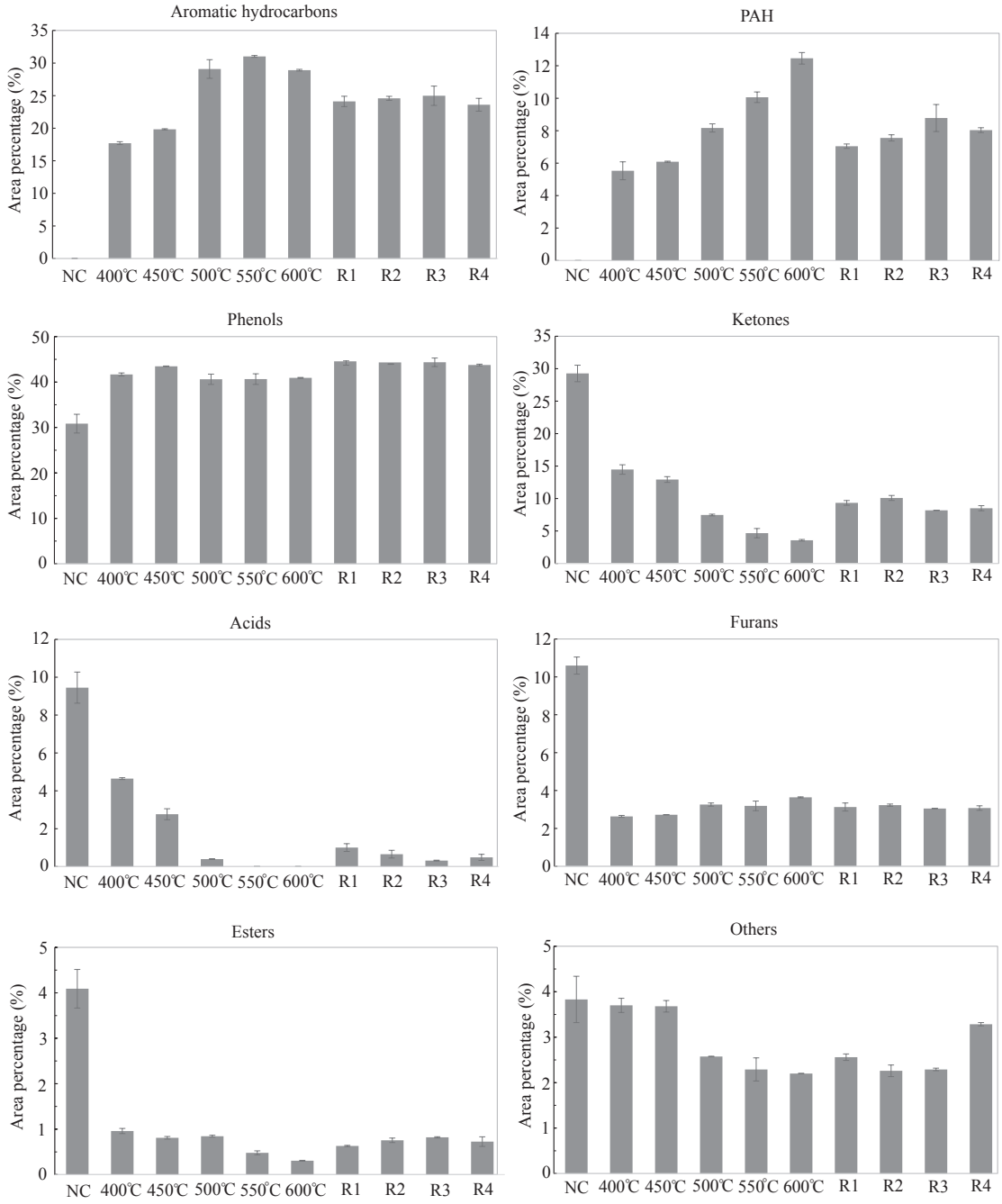

Figure 4.4: Chemical composition of the oil phase in bio-oil as determined by GC/MS peak areas (%). NC refers to non-catalytic pyrolysis.

cantly increases the hydrocarbon contents in the bio-oil, it is also necessary to mention that not all the hydrocarbon compounds are desirable. For example, the PAH found in current study are mainly naphthalene related compounds, and exposure to large amounts of naphthalene may damage or destroy red blood cells [70]. Oxygenated

species such as ketones will affect the bio-oil quality by aging reactions while acids will cause the bio-oil to be corrosive and make it difficult to be used in engines or transported via pipelines [59]. Apparent from Figure 4.4, bio-oil from non-catalytic pyrolysis contains a large composition of ketones and acids. However, after catalysis, the relative contents of ketones and acids in the organic phase of bio-oil are significantly reduced, and the acids content reduces to zero when the catalyst temperature exceeds 550 °C.

Furans are products from the dehydration of hemicellulose in the biomass and they can further react to form hydrocarbons and coke in the presence of catalyst [71]. The reduced content of furans after catalysis (Figure 4.4) may be due to the reason that furans are reacted to hydrocarbon gases which further react to form aromatic hydrocarbons. However, the effect of catalyst temperature and catalyst regeneration on the relative content of furans is not clear from the current study.

Phenols are the most abundant species in the organic part of the bio-oil and they consist of phenol, alkylated phenols, creosol etc. Phenols are high value chemicals and have been used as an adhesive or adhesive extender for waterproof plywood and exhibited excellent performance [6]. Phenols are formed from the non-catalytic depolymerization of the lignin in biomass. In catalytic pyrolysis, the concentration of phenols is determined by its production from lignin conversion and the consumption to single ring aromatics [72]. The relative concentration of phenols increases from 30% to about 40% after catalysis, and remains almost constant for different cases. It should be noted that as the catalyst temperature increases, the yield of the bio-oil from pine wood pyrolysis decreases, indicating that the absolute mass fraction of the phenols in the bio-oil also decreases. This is reasonable since increasing catalyst temperature facilitates the conversion of phenols to hydrocarbon species.

Overall, it is seen that there is a large increase in the content of hydrocarbon compounds and a decrease of acids and ketones after catalysis. Nevertheless, the

improved bio-oil product is obtained at the expense of the absolute yield of liquid. Considering that the fraction of acids in the organic phase is already very small when the catalyst temperature is 500 °C and there is also a relatively high aromatic hydrocarbon fraction, this work would suggest keeping catalyst temperature around 500 °C for the pyrolysis of centimeter-scale pine biomass particles.

4.4 Conclusion

Non-catalytic and catalytic pyrolysis of centimeter-scale pine wood particles have been investigated in a vertical tube furnace reactor to study the effects of catalyst temperature and regeneration. There is an obvious change of the liquid and gas yields from catalytic pyrolysis comparing to non-catalytic pyrolysis, while the yields of char and coke are not affected. Besides, the change in water yields is very small for different catalyst treatments while the organic yield varies. Gas analysis shows that CO and CO_2 are the most abundant species in the gas products and their yields increase with increasing catalyst temperatures. The amount of alkene gas species increases significantly for the catalytic upgrading process. The GC-MS analysis of the liquid products in the organic phase shows that a large amount of aromatic hydrocarbons and PAH are present after catalytic treatment, while no hydrocarbon species are detected in the bio-oil for the non-catalytic case. The ketones and acids contents in the bio-oil are also reduced after catalysis. Using regenerated catalyst, the pyrolysis products show no obvious difference comparing to the cases where fresh catalyst is used, indicating that the catalyst retains sufficient activity in producing the targeted chemical compounds.

CHAPTER V

Conclusions and Future Work

5.1 Conclusions

This thesis is about how to utilize the abundant biomass resources by investigating the pyrolysis of centimeter scale biomass particles. It leads to an improved understanding of pyrolysis of centimeter-scale biomass particles of various sizes and shapes and provides a unified predictive mathematical model to help design the biomass reactors. It also advances the understanding of de-oxygenating bio-oil by thermal and catalytic methods.

In Chapter II, a mathematical model was introduced to study the pyrolysis behavior of biomass particles of various shapes and sizes. Biomass particles commonly have irregular shapes and sizes, resulting in various particle surface area to volume ratios (SVR) which are critical to heat and mass transfer rates. In this chapter, the theory of prolate and oblate spheroids was applied to model the pyrolysis of biomass. A novel solution methodology was developed to accommodate for a wide variety of particle geometries. Prolate ellipsoids include shapes ranging from thin needles to spheres, whereas, oblate ellipsoids include shapes ranging from thin disks to spheres. The choice of these smooth shapes, while facilitating expedient computations also enables the coverage of wide ranges of SVR. Model simulations showed satisfactory agreement with relevant literature and experimental data. Particle aspect ratio, SVR,

and equivalent radius (R_e) were used to define the particle geometry. It was shown that with the decrease of aspect ratio, wood particle decomposed faster and the final char fraction became smaller. A power-law based correlation between the pyrolysis duration time and the SVR was derived and verified against experiments. This model can be used to predict the pyrolysis rate of wood particles having arbitrary shapes and sizes and help the development of biomass conversion system. Further, it was shown that an increase in the SVR enhanced the production of tar and decreased the yield of char while leaving the yield of gas mostly unaffected.

The bio-oil directly produced from biomass pyrolysis is essentially a complex mixture of oxygenated compounds and contains a large amount of oxygen. It does not have the necessary chemical and physical properties such that it can be readily processed further in a petroleum refinery into final renewable transportation fuels. In order to improve the bio-oil quality and get hydrocarbon species, treatments of pyrolysis are performed, including the pre-treatment of the biomass before it is used for pyrolysis and the post-treatment of the pyrolysis vapor immediately following the pyrolysis.

Torrefaction is the pre-treatment of biomass in a relatively low temperature range of 225–300°C. It changes the properties of biomass and subsequently affects the pyrolysis products. In Chapter III, the effect of torrefaction on pyrolysis of centimeter-scale pine wood was studied experimentally. It was found that torrefaction at 225 °C and 250 °C for 15, 25 and 35 min had little effect on the pyrolysis products. However, when wood was torrefied at 275 °C and 300 °C, significant char formation and transformation occurred. During the pyrolysis processes, lower weight loss rate and higher char fraction were observed for wood torrefied at 275 °C and 300 °C, but the center temperature profiles were not affected. Conversion time for pyrolysis was also not affected by the torrefaction conditions. Pyrolysis yields of liquid, gas and char were measured and found to be affected by the torrefaction conditions. GC-MS analysis

of bio-oil obtained from torrefied wood shows that the acid content decreases with increasing torrefaction intensity, implying improvement of bio-oil quality. Further, phenol content increases and guaiacols content decreases with the increase of torrefaction intensity. On the other hand, no novel species were detected and the overall effect of torrefaction was less remarkable than anticipated for the temperatures tested.

Catalysis can be utilized as a post-treatment of biomass pyrolysis vapor using a zeolite catalyst in high temperature. Chapter IV investigates pyrolysis of centimeter-scale biomass particles with and without catalysis. The pyrolysis oil before catalysis was homogeneous and highly oxygenated and no aromatic hydrocarbons or PAH were detected. Upon catalytic treatment, the yield of bio-oil was markedly reduced and decreased with increasing catalyst temperature; while oxygen containing species was increasingly converted to CO and CO_2. The change of water content was very small for different catalytic pyrolysis cases and experiment results indicated that conversion of oxygen was mainly to CO and CO_2 as the catalyst temperature increases. Chemical analysis of the bio-oil showed that aromatic hydrocarbons and PAH were formed in significant amounts upon catalytic treatment. Finally, the content of acids and ketones was reduced after catalysis, showing an improvement of the quality of bio-oil. The effect of the usage of regenerated catalyst on the pyrolysis products was not significant in the current study. Overall, using catalyst is beneficial in producing hydrocarbon species and reducing the acidity of the bio-oil product, but the improved pyrolysis product is obtained at the expense of the absolute yield of liquid. Based on the experiment results, a suggestion was made to keep catalyst temperature around 500 °C for the pyrolysis of centimeter-scale pine biomass particles.

5.2 Future Work

Future studies that may follow from the work presented in this thesis may include:: 1) Pyrolysis of an assemble of biomass particles of various sizes and shapes, 2) Reduce

catalyst coking during the pyrolysis process, 3) Kinetic mechanism development of zeolite cracking, 4) Co-feeding biomass with coals to produce combustible gases for power generation, etc.

5.2.1 Pyrolysis of Multiple Biomass Particles

The thesis focuses on the pyrolysis of single biomass particles, even though they have a variety of shapes and sizes. Mathematical modeling and experimental investigation of the pyrolysis of single biomass particle is beneficial for the understanding of the pyrolysis behavior since it allows the researchers to focus on the internal processes during the pyrolysis process, such as the heat and mass transfer which controls the product release. However, to produce renewable biofuels for the industrial applications, large scale biomass converters are required, which means biomass particles with a wide range of sizes and shapes are fed into the reactor simultaneously. Chapter II provides a numerical model and an experimental method to study the pyrolysis of single biomass particle, and it may be meaningful to extend the current work to further study the pyrolysis of an ensemble of these particles for various furnace settings.

5.2.2 Reduce Catalyst Coke

The catalysts deactivate very soon due to carbon deposition during zeolite cracking reactions. In a study of catalytic transformation of crude bio-oil into hydrocarbons, Gayubo et al. [73] found two types of coke deposited on the zeolite catalyst, with thermal coke formed mainly by polymerization of bio-oil phenolic components and catalytic coke from bio-oil oxygenate compounds by acid sites. Co-feeding of hydrogen has been investigated for catalytic cracking of single chemical components such as benzaldehyde [74] and anisole [75], and a decreased amount of carbon formation in the catalyst was observed in the presence of hydrogen. Horne [76] studied the catalytic co-processing of biomass-derived pyrolysis vapors and methanol and there was an overall

increase in hydrocarbon products. Sharypov [77] carried out catalytic pyrolysis of pine wood and polyolefinic polymers mixture in an atmosphere of hydrogen. Nevertheless, the deactivation of catalyst was not investigated in these two works. In general, co-feeding of H_2 or other hydrogen donors such as methanol can possibly improve bio-oil quality and decrease catalyst coking, but this subject is not yet examined completely and few reports are found to use centimeter-scale biomass particles as feedstock. Besides, in the experiments on oxidative pyrolysis, O_2 can help oxidize coke deposited on the catalyst and adding O_2 to reduce catalyst coking has seldom been investigated in the past. However, the oxygen content needs to be carefully controlled to prevent the oxidization of pyrolysis vapors. The following experiments are proposed to address these issues.

1. Catalytic pyrolysis of biomass particles by co-feeding H_2, CH_4 and methanol. Amount of deposited coke on the catalyst may depend on the fraction of hydrogen donor gases in the nitrogen stream and the operation conditions. Determining these variables is a topic of research. Careful operations will be required when conducting the experiments as these gases are highly combustible.

2. Recycling non-condensable gases such as CO, CO_2 into the furnace reactor to investigate the effect of non-condensable gases on the coke deposition on the catalyst as well as the properties of bio-oil. This is important for an industrial-scale reactor as it reduces the use of N_2.

3. Co-feeding O_2 to partially oxidize the coke in the catalyst. O_2 concentration needs to be adjusted to find the optimal value.

5.2.3 Development of zeolite cracking mechanism for catalytic pyrolysis

Zeolite cracking is an ex-situ catalytic process in which dried biomass is rapidly heated to produce pyrolysis vapors then these vapors are passed through hot catalyst

beds for further deoxygenation. This results in a stabilized bio-oil with an aqueous phase and an organic phase after condensation. The kinetic mechanism of zeolite cracking is not well understood as yet. Only a few studies report the zeolite cracking mechanism. Adjaye investigated kinetic modeling of the conversion of bio-oil over HZSM-5 catalyst in a fixed-bed micro-reactor and proposed a reaction pathway for the conversion of bio-oil [78]. In this model, bio-oil vapors were initially separated into non-volatiles and volatiles. The non-volatiles crack into residue, volatiles and coke. The volatile portion reacts through processes such as de-oxygenation, secondary cracking, oligomerization etc. to produce hydrocarbons, gases, residue, aqueous phases and coke. This model attributes the coke formation to the cracking of some non-volatile components and polymerization of the organic distillates. As discussed in [53], such a model succeeds in explaining the experimental data to some extent, but it becomes insufficient to describe the rate correlations in the broad context. Besides, the model does not give time-resolved species changes and the compositions of the non-volatiles. It is necessary to develop a time-dependent reaction network of zeolite cracking to describe the evolution of different species during the catalytic pyrolysis. Real-time gas analyzers can be used to measure the gas compositions and incorporate the data into the model to predict product yields.

5.2.4 Producing Power from Biomass

Biomass pyrolysis not only produces bio-oil, but also generates the combustible gases that may be used in a gas turbine, an engine, or a steam boiler to generate power with minimal pollutant formation. Coal consumption is the highest in developing countries such as China and India, which leads to severe pollutant emissions such as SO_x, NO_x, PM 2.5, soot, etc. Thus it is highly important to develop a cleaner method to utilize coal resources. Co-processing of coal with biomass offers a number of advantages: 1) Biomass is CO_2-neutral, 2) Biomass produces acetic acid that increases

SO_2 capture efficiency of sorbent such as lime, 3) The use of coal could help provide stable pyrolysis or gasification conditions as biomass may give rise to fluctuations in quality, availability, and chemical composition. Proposed tasks includes conducting experiments to determine the rate of formation of the pyrolysis products from the coal-biomass mixture, their chemical composition, heat of combustion and the rate of formation of char as a function of the reactor temperature.

APPENDICES

APPENDIX A

Oblate Spheroid

A.1 Oblate Coordinate System

An oblate spheroid solid is obtained by rotating an ellipse about its minor axis (Figure A.1). The oblate spheroidal coordinate system is related to the Cartesian coordinate system through the following transition.

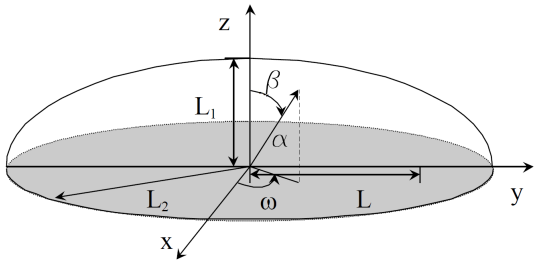

Figure A.1: Characteristic of an oblate spheroids.

$$
\begin{aligned}
x &= f \cosh\alpha \sin\beta \cos\omega \\
y &= f \cosh\alpha \sin\beta \sin\omega \\
z &= f \sinh\alpha \cos\beta
\end{aligned} \tag{A.1}
$$

Where, f is the focal length, $0 \leq \alpha \leq \infty, 0 \leq \beta \leq \pi, 0 \leq \omega \leq 2\pi$. Surfaces of constant α form oblate spheroids while those of constant β generate hyperboloids of revolution.

An alternative form is defined by:

$$\xi = \sinh\alpha, \eta = \cos\beta, \phi = \omega \tag{A.2}$$

Where, $0 \leq \xi \leq \infty, -1 \leq \eta \leq 1, 0 \leq \phi \leq 2\pi$. Then we have

$$\begin{aligned} x &= f\sqrt{(\xi^2+1)(1-\eta^2)}\cos\phi \\ y &= f\sqrt{(\xi^2+1)(1-\eta^2)}\sin\phi \\ z &= f\xi\eta \end{aligned} \tag{A.3}$$

Gradient and divergence are given by:

$$\vec{\nabla} = \frac{\hat{e}_\xi}{f}\sqrt{\frac{(\xi^2+1)}{(\xi^2+\eta^2)}}\frac{\partial}{\partial\xi} + \frac{\hat{e}_\eta}{f}\sqrt{\frac{(1-\eta^2)}{(\xi^2+\eta^2)}}\frac{\partial}{\partial\eta} + \frac{\hat{e}_\phi}{f\sqrt{(\xi^2+1)(1-\eta^2)}}\frac{\partial}{\partial\phi} \tag{A.4}$$

$$\begin{aligned} \vec{\nabla}\cdot\vec{V} = &\frac{1}{f(\xi^2+\eta^2)}\left[\frac{\partial}{\partial\xi}\left(V_\xi\sqrt{\frac{\xi^2+\eta^2}{\xi^2+1}}\right) + \frac{\partial}{\partial\eta}\left(V_\eta\sqrt{\frac{\xi^2+\eta^2}{1-\eta^2}}\right)\right] \\ &+ \frac{1}{f(\xi^2+\eta^2)}\left[\frac{\partial}{\partial\phi}\left(\frac{V_\phi(\xi^2+\eta^2)}{\sqrt{(\xi^2+1)(1-\eta^2)}}\right)\right] \end{aligned} \tag{A.5}$$

A.2 Conservation Equations in Oblate Coordinate System

Conservation equations for gas and tar are:

$$\frac{\partial}{\partial t}\left(\frac{\varepsilon P_t}{T}\right) = \vec{\nabla}\cdot\left(\frac{BP_t}{\mu T}\vec{\nabla}P\right) + \frac{R}{M_t}S_t \tag{A.6}$$

$$\frac{\partial}{\partial t}\left(\frac{\varepsilon P_g}{T}\right) = \vec{\nabla}\cdot\left(\frac{BP_g}{\mu T}\vec{\nabla}P\right) + \frac{R}{M_g}S_g \tag{A.7}$$

In oblate coordinate system, the Equation A.6 and Equation A.7 become

$$\frac{\partial}{\partial t}\left(\frac{\varepsilon P_t}{T}\right) = \frac{1}{f^2(\xi^2+\eta^2)}\left[\frac{\partial}{\partial\xi}\left(\frac{BP_t}{\mu T}(\xi^2+1)\frac{\partial P}{\partial\xi}\right) + \frac{\partial}{\partial\eta}\left(\frac{BP_t}{\mu T}(1-\eta^2)\frac{\partial P}{\partial\eta}\right)\right] + \frac{R}{M_t}S_t \tag{A.8}$$

$$\frac{\partial}{\partial t}\left(\frac{\varepsilon P_g}{T}\right) = \frac{1}{f^2(\xi^2+\eta^2)}\left[\frac{\partial}{\partial\xi}\left(\frac{BP_g}{\mu T}(\xi^2+1)\frac{\partial P}{\partial\xi}\right) + \frac{\partial}{\partial\eta}\left(\frac{BP_g}{\mu T}(1-\eta^2)\frac{\partial P}{\partial\eta}\right)\right] + \frac{R}{M_g}S_g \tag{A.9}$$

The balance of energy is governed by

$$(\rho_s C_s + \varepsilon\rho_v C_v)\frac{\partial T}{\partial t} + \rho_v C_v \vec{V}\cdot\vec{\nabla}T = \vec{\nabla}\cdot(\lambda\vec{\nabla}T) + Q \tag{A.10}$$

or,

$$\begin{aligned}(\rho_s C_s + \varepsilon\rho_v C_v)\frac{\partial T}{\partial t} = {} & \frac{1}{f^2(\xi^2+\eta^2)}\left[\frac{\partial}{\partial\xi}\left(\lambda(\xi^2+1)\frac{\partial T}{\partial\xi}\right) + \frac{\partial}{\partial\eta}\left(\lambda(1-\eta^2)\frac{\partial T}{\partial\eta}\right)\right] \\ & + \rho_v C_v \frac{B}{\mu}\frac{1}{f^2(\xi^2+\eta^2)}\left[\frac{\partial}{\partial\xi}(\xi^2+1)\frac{\partial P}{\partial\xi}\frac{\partial T}{\partial\xi} + \frac{\partial T}{\partial\eta}(1-\eta^2)\frac{\partial P}{\partial\eta}\frac{\partial T}{\partial\eta}\right] \\ & + Q\end{aligned} \tag{A.11}$$

Initial conditions at $t = 0$ are:

$$\begin{aligned} & T(\xi,\eta,0) = T_0, \quad P(\xi,\eta,0) = P_0 \\ & \rho_a(\xi,\eta,0) = \rho_0, \quad \rho_{is}(\xi,\eta,0) = 0, \quad \rho_c(\xi,\eta,0) = 0 \end{aligned} \tag{A.12}$$

Further, the following symmetry conditions are used,

$$\begin{aligned}
&\frac{\partial T(\xi,\eta=1,t)}{\partial \eta}=0, \quad \frac{\partial T(\xi,\eta=0,t)}{\partial \eta}=0, \quad \frac{\partial T(\xi=0,\eta,t)}{\partial \xi}=0 \\
&\frac{\partial P(\xi,\eta=1,t)}{\partial \eta}=0, \quad \frac{\partial P(\xi,\eta=0,t)}{\partial \eta}=0, \quad \frac{\partial P(\xi=0,\eta,t)}{\partial \xi}=0
\end{aligned} \tag{A.13}$$

The pressure at the particle surface is atmospheric. The thermal flux through the boundary is determined by convective and radiative heat transfer.

$$\begin{aligned}
&P(\xi=\xi_s,\eta,t)=P_0 \\
&\frac{\lambda}{f}\sqrt{\frac{\xi^2+1}{\xi^2+\eta^2}}\frac{\partial T_s}{\partial \xi_s}=h(T_g-T_s)+\sigma\varepsilon(T_f^4-T_s^4)
\end{aligned} \tag{A.14}$$

where, T_s, T_g and T_f are the temperatures of the particle surface, gas and furnace wall respectively.

A.3 Simulation Results for Oblate Particles

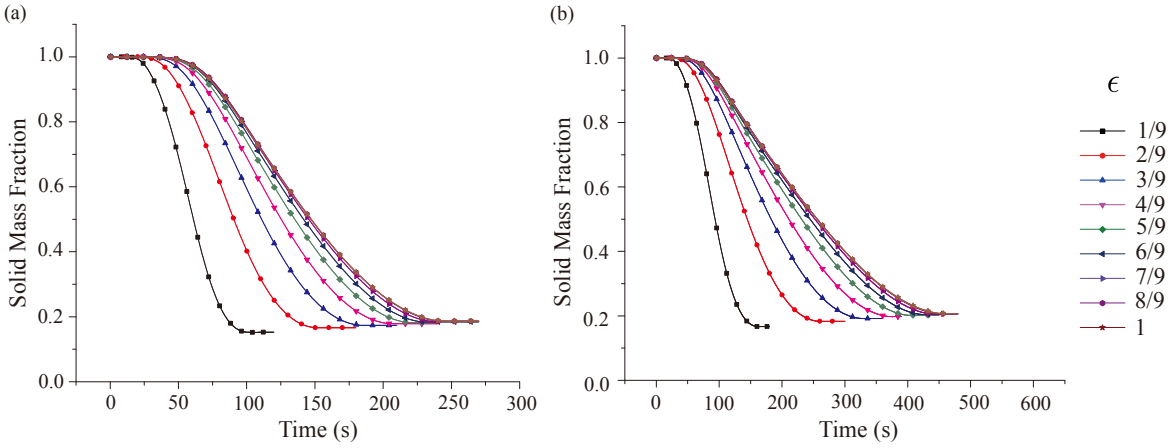

Figure A.2: Mass loss profiles for different oblate particles. (a):R_e = 1.0 cm; (b):R_e = 1.5 cm.

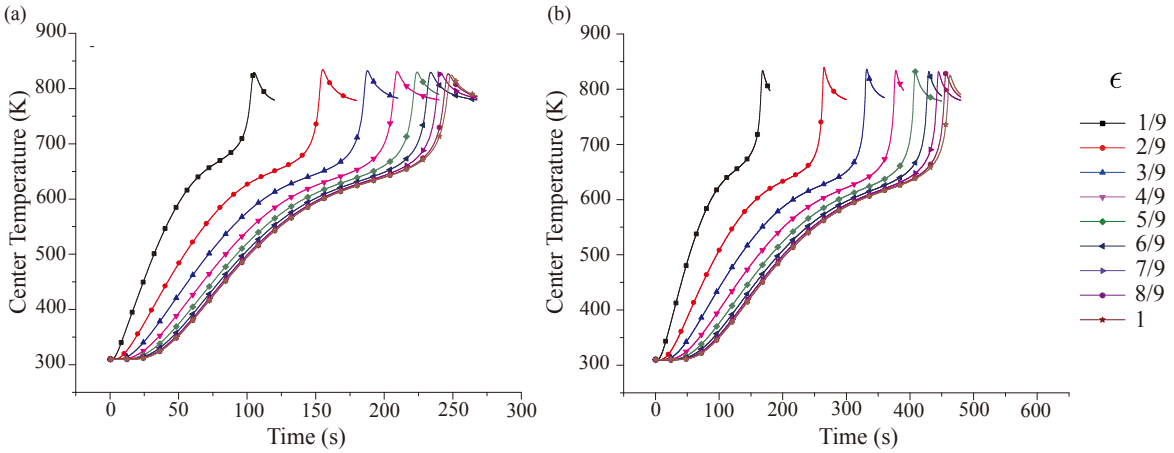

Figure A.3: Center temperature profiles for different oblate particles. (a):R_e = 1.0 cm; (b):R_e = 1.5 cm.

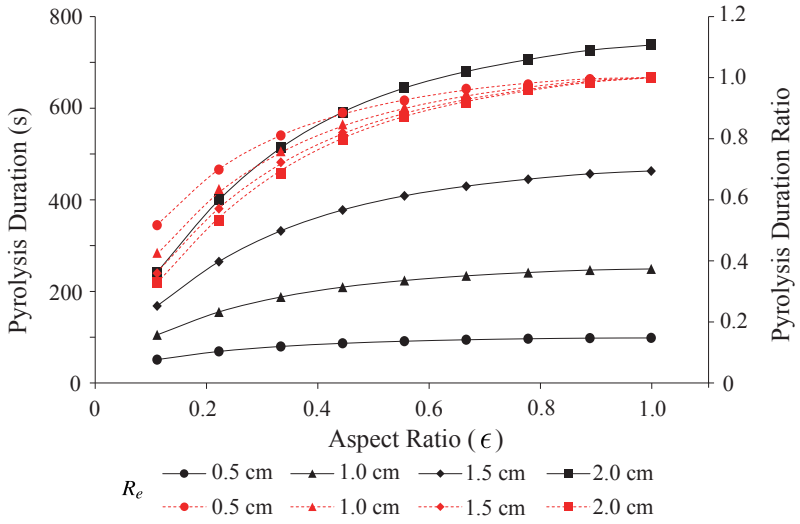

Figure A.4: Effect of aspect ratio on the pyrolysis duration of oblate wood particles. $R_e = 0.5$ cm, 1.0 cm, 1.5 cm and 2.0 cm. Line: pyrolysis duration; Dashes: pyrolysis duration ratio.

APPENDIX B

Numerical Discretization of Energy and Mass Conservation Equations

B.1 Governing Equations

B.1.1 Energy

$$(\rho_s C_s + \varepsilon\rho_v C_v)\frac{\partial T}{\partial t} = \vec{\nabla}\cdot(\lambda\vec{\nabla}T) + \rho_v C_v \frac{B}{\mu}\vec{\nabla}P\cdot\vec{\nabla}T + Q \tag{B.1}$$

In prolate coordinate system (symmetry along z axis),

For$\vec{\nabla}\cdot(\lambda\vec{\nabla}T)$, we have

$$\begin{aligned}\vec{\nabla}\cdot(\lambda\vec{\nabla}T) &= \frac{1}{f^2(\xi^2-\eta^2)}\left[\frac{\partial}{\partial\xi}\left(\lambda(\xi^2-1)\frac{\partial T}{\partial\xi}\right) + \frac{\partial}{\partial\eta}\left(\lambda(1-\eta^2)\frac{\partial T}{\partial\eta}\right) + \cancel{\frac{\partial}{\partial\phi}\left(\lambda\frac{\xi^2-\eta^2}{(\xi^2-1)(1-\eta^2)}\frac{\partial T}{\partial\phi}\right)}\right] \\ &= \frac{1}{f^2(\xi^2-\eta^2)}\left[\frac{\partial}{\partial\xi}\left(\lambda(\xi^2-1)\right)\frac{\partial T}{\partial\xi} + \lambda(\xi^2-1)\frac{\partial^2 T}{\partial\xi^2} + \frac{\partial}{\partial\eta}\left(\lambda(1-\eta^2)\right)\frac{\partial T}{\partial\eta} + \lambda(1-\eta^2)\frac{\partial^2 T}{\partial\eta^2}\right]\end{aligned} \tag{B.2}$$

For $\vec{\nabla}P \cdot \vec{\nabla}T$, we have

$$\begin{aligned}\vec{\nabla}P \cdot \vec{\nabla}T &= \frac{\xi^2-1}{f^2(\xi^2-\eta^2)}\frac{\partial P}{\partial \xi}\frac{\partial T}{\partial \xi} + \frac{1-\eta^2}{f^2(\xi^2-\eta^2)}\frac{\partial P}{\partial \eta}\frac{\partial T}{\partial \eta} + \cancel{\frac{1}{f^2(\xi^2-1)(1-\eta^2)}\frac{\partial P}{\partial \phi}\frac{\partial T}{\partial \phi}} \\ &= \frac{1}{f^2(\xi^2-\eta^2)}\left[(\xi^2-1)\frac{\partial P}{\partial \xi}\frac{\partial T}{\partial \xi} + (1-\eta^2)\frac{\partial P}{\partial \eta}\frac{\partial T}{\partial \eta}\right] \end{aligned} \tag{B.3}$$

Then the governing equation becomes,

$$\begin{aligned}(\rho_s C_s + \varepsilon\rho_v C_v)\frac{\partial T}{\partial t} = &\frac{1}{f^2(\xi^2-\eta^2)}\left[\frac{\partial}{\partial \xi}\left(\lambda(\xi^2-1)\right)\frac{\partial T}{\partial \xi} + \lambda(\xi^2-1)\frac{\partial^2 T}{\partial \xi^2} + \frac{\partial}{\partial \eta}\left(\lambda(1-\eta^2)\right)\frac{\partial T}{\partial \eta} + \lambda(1-\eta^2)\frac{\partial^2 T}{\partial \eta^2}\right] \\ &+ \rho_v C_v \frac{B}{\mu}\frac{1}{f^2(\xi^2-\eta^2)}\left[(\xi^2-1)\frac{\partial P}{\partial \xi}\frac{\partial T}{\partial \xi} + (1-\eta^2)\frac{\partial P}{\partial \eta}\frac{\partial T}{\partial \eta}\right] \\ &+ Q \end{aligned} \tag{B.4}$$

B.1.2 Mass Conservation for Gas and Tar

$$\frac{\partial}{\partial t}\left(\frac{\varepsilon P_g}{T}\right) = \vec{\nabla}\cdot\left(\frac{BP_g}{\mu T}\vec{\nabla}(P_g+P_t)\right) + \frac{R}{M_g}S_g \tag{B.5}$$

$$\frac{\partial}{\partial t}\left(\frac{\varepsilon P_t}{T}\right) = \vec{\nabla}\cdot\left(\frac{BP_t}{\mu T}\vec{\nabla}(P_g+P_t)\right) + \frac{R}{M_t}S_t \tag{B.6}$$

In prolate coordinate system, we have

$$\frac{\partial}{\partial t}\left(\frac{\varepsilon P_g}{T}\right) = \frac{1}{f^2(\xi^2-\eta^2)}\left[\frac{\partial}{\partial \xi}\left(\frac{BP_g}{\mu T}(\xi^2-1)\frac{\partial(P_g+P_t)}{\partial \xi}\right) + \frac{\partial}{\partial \eta}\left(\frac{BP_g}{\mu T}(1-\eta^2)\frac{\partial(P_g+P_t)}{\partial \eta}\right)\right] + \frac{R}{M_g}S_g \tag{B.7}$$

$$\frac{\partial}{\partial t}\left(\frac{\varepsilon P_t}{T}\right) = \frac{1}{f^2(\xi^2-\eta^2)}\left[\frac{\partial}{\partial \xi}\left(\frac{BP_t}{\mu T}(\xi^2-1)\frac{\partial(P_g+P_t)}{\partial \xi}\right) + \frac{\partial}{\partial \eta}\left(\frac{BP_t}{\mu T}(1-\eta^2)\frac{\partial(P_g+P_t)}{\partial \eta}\right)\right] + \frac{R}{M_t}S_t \tag{B.8}$$

B.1.3 Boundary Conditions

The angular and radical gradient of temperature and pressure equals to 0 at the planes of symmetry. That is:

$$\begin{aligned} &\frac{\partial T(\xi,\eta=1,t)}{\partial \eta}=0, \quad \frac{\partial T(\xi,\eta=0,t)}{\partial \eta}=0, \quad \frac{\partial T(\xi=1,\eta,t)}{\partial \xi}=0 \\ &\frac{\partial P(\xi,\eta=1,t)}{\partial \eta}=0, \quad \frac{\partial P(\xi,\eta=0,t)}{\partial \eta}=0, \quad \frac{\partial P(\xi=1,\eta,t)}{\partial \xi}=0 \end{aligned} \tag{B.9}$$

B.2 Discretization

Governing equations are discretized to be numerically solved. Finite volume method (FVM) is used. The cell-centered approach is shown in Figure B.1

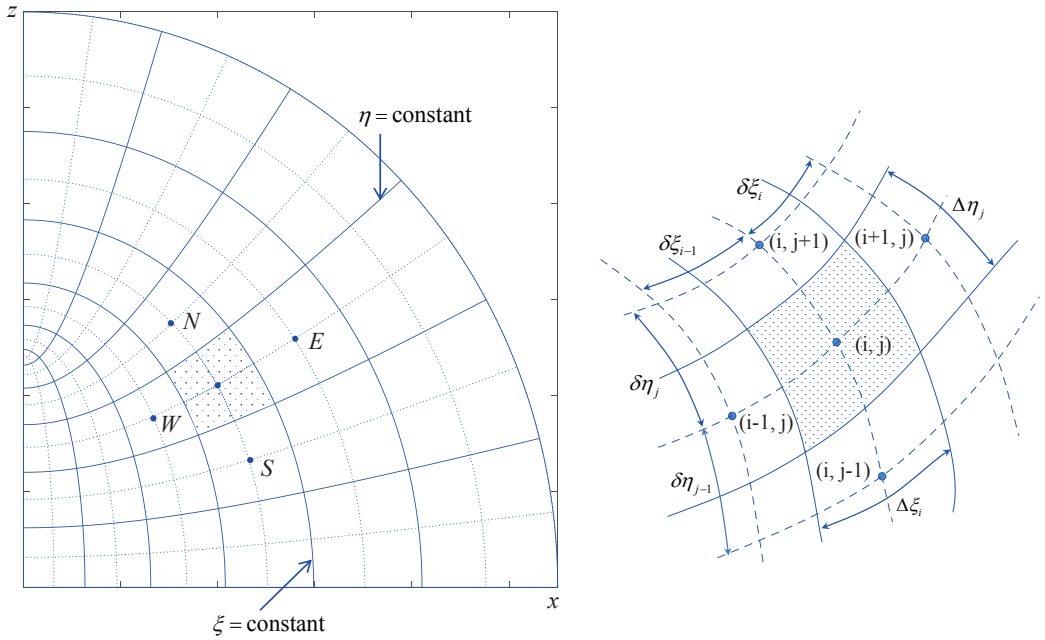

Figure B.1: Geometrical configuration of the physical problem.

B.2.1 Energy

Discretize the above Equation B.4 as below, where, n and $n+1$ represent old and new time steps; m and $m+1$ correspond to iteration steps.

$$\frac{\partial T}{\partial t} = \frac{T_{i,j}^{n+1,m+1} - T_{i,j}^{n}}{\Delta t}$$

$$\frac{\partial}{\partial \xi}\left(\lambda(\xi^2-1)\frac{\partial T}{\partial \xi}\right) = \frac{1}{\Delta \xi_i}\left(\lambda_{i+1/2,j}(\xi_{i+1/2}^2-1)\frac{T_{i+1,j}^{n+1,m} - T_{i,j}^{n+1,m+1}}{\delta \xi_i} - \lambda_{i-1/2,j}(\xi_{i-1/2}^2-1)\frac{T_{i,j}^{n+1,m+1} - T_{i-1,j}^{n+1,m}}{\delta \xi_{i-1}}\right)$$

$$\frac{\partial}{\partial \eta}\left(\lambda(1-\eta^2)\frac{\partial T}{\partial \eta}\right) = \frac{1}{\Delta \eta_j}\left(\lambda_{i,j+1/2}(1-\eta_{i+1/2}^2)\frac{T_{i,j+1}^{n+1,m} - T_{i,j}^{n+1,m+1}}{\delta \eta_j} - \lambda_{i,j-1/2}(1-\eta_{j-1/2}^2)\frac{T_{i,j}^{n+1,m+1} - T_{i,j-1}^{n+1,m}}{\delta \eta_{j-1}}\right)$$

where, interface thermal conductivity is calculated by weight average:

$$\lambda_{i+1/2,j} = \frac{\delta\xi_{i^+}}{\delta\xi_i}\lambda_{i,j} + \frac{\delta\xi_{i^-}}{\delta\xi_i}\lambda_{i+1,j}$$

$$\lambda_{i,j+1/2} = \frac{\delta\eta_{j^+}}{\delta\eta_j}\lambda_{i,j} + \frac{\delta\eta_{j^-}}{\delta\eta_j}\lambda_{i,j+1}$$

Convective terms are discretized by upwind scheme to increase stability of the solution, thus we have:

$$\frac{\partial P}{\partial \xi}\frac{\partial T}{\partial \xi} = \frac{1}{\delta\xi}\left[\max\left(-\frac{\partial P}{\partial \xi}, 0\right)T_{i-1,j}^{n+1,m} - \left|\frac{\partial P}{\partial \xi}\right|T_{i,j}^{n+1,m+1} + \max\left(\frac{\partial P}{\partial \xi}, 0\right)T_{i+1,j}^{n+1,m}\right]$$

where, $\delta\xi = \delta\xi_i$ if $\dfrac{\partial P}{\partial \xi} > 0$ and $\delta\xi = \delta\xi_{i-1}$ if $\dfrac{\partial P}{\partial \xi} < 0$.

$$\frac{\partial P}{\partial \eta}\frac{\partial T}{\partial \eta} = \frac{1}{\delta\eta}\left[\max\left(-\frac{\partial P}{\partial \eta}, 0\right)T_{i,j-1}^{n+1,m} - \left|\frac{\partial P}{\partial \xi}\right|T_{i,j}^{n+1,m+1} + \max\left(\frac{\partial P}{\partial \eta}, 0\right)T_{i,j-1}^{n+1,m}\right]$$

where, $\delta\eta = \delta\eta_j$ if $\dfrac{\partial P}{\partial \eta} > 0$ and $\delta\eta = \delta\eta_{j-1}$ if $\dfrac{\partial P}{\partial \eta} < 0$.
Spatial discretization of pressure is given by:

$$\frac{\partial P}{\partial \xi} = \frac{1}{\delta\xi_i + \delta\xi_{i-1}}(P_{i+1,j}^{n+1,m} - P_{i-1,j}^{n+1,m})$$

$$\frac{\partial P}{\partial \eta} = \frac{1}{\delta\eta_j + \delta\eta_{j-1}}(P_{i,j+1}^{n+1,m} - P_{i,j-1}^{n+1,m})$$

After rearrangement, the new time step temperature is obtained by the following equation.

$$\boxed{A_P T_{i,j}^{n+1,m+1} = A_W T_{i-1,j}^{n+1,m} + A_E T_{i+1,j}^{n+1,m} + A_S T_{i,j-1}^{n+1,m} + A_N T_{i,j+1}^{n+1,m+1} + F}$$

where,

$$A_P = A_W + A_E + A_S + A_N + \frac{(\rho_s C_s + \varepsilon \rho_v C_v)_{i,j}}{\Delta t}$$

$$A_W = J\frac{\lambda_{i-1/2,j}(\xi^2_{i-1/2}-1)}{\Delta\xi_i \delta\xi_{i-1}} + J\frac{\xi^2-1}{\delta\xi}\max\left(-\frac{\partial P}{\partial \xi}, 0\right)$$

$$A_E = J\frac{\lambda_{i+1/2,j}(\xi^2_{i+1/2}-1)}{\Delta\xi_i \delta\xi_{i}} + J\frac{\xi^2-1}{\delta\xi}\max\left(\frac{\partial P}{\partial \xi}, 0\right)$$

$$A_S = J\frac{\lambda_{i,j-1/2}(1-\eta^2_{j-1/2})}{\Delta\eta_j \delta\eta_{j-1}} + J\frac{1-\eta^2}{\delta\eta}\max\left(-\frac{\partial P}{\partial \eta}, 0\right)$$

$$A_N = J\frac{\lambda_{i,j+1/2}(1-\eta^2_{j+1/2})}{\Delta\eta_j \delta\eta_{j}} + J\frac{1-\eta^2}{\delta\eta}\max\left(\frac{\partial P}{\partial \eta}, 0\right)$$

$$K = \rho_v C_v \frac{B}{\mu} J$$

$$J = \frac{1}{f^2(\xi^2-\eta^2)}$$

$$F = Q + \frac{(\rho_s C_s + \varepsilon \rho_v C_v)_{i,j}}{\Delta t} T^n_{i,j}$$

B.2.2 Mass Conservation for Gas and Tar

B.2.2.1 Gas

The above Equation B.7 is discretized as below, where, n and $n+1$ represent old and new time steps; m and $m+1$ correspond to iteration steps.

$$\frac{\partial}{\partial t}\left(\frac{\varepsilon P_g}{T}\right) = \frac{1}{\Delta t}\left(\frac{\varepsilon^{n+1,m}_{i,j}}{T^{n+1,m}_{i,j}} P^{n+1,m+1}_{g,i,j} - \frac{\varepsilon^{n}_{i,j}}{T^{n}_{i,j}} P^{n}_{g,i,j}\right)$$

$$\begin{aligned}\frac{\partial}{\partial \xi}\left(\frac{BP_g}{\mu T}(\xi^2-1)\frac{\partial(P_g+P_t)}{\partial \xi}\right) = &\frac{1}{\Delta\xi_i}\left(\frac{BP_g}{\mu T}\bigg|^{n+1,m}_{i+1/2,j}(\xi^2_{i+1/2}-1)\frac{P^{n+1,m}_{g,i+1,j}+P^{n+1,m}_{t,i+1,j}-P^{n+1,m+1}_{g,i,j}-P^{n+1,m}_{t,i,j}}{\delta\xi_i}\right)\\ &-\frac{1}{\Delta\xi_i}\left(\frac{BP_g}{\mu T}\bigg|^{n+1,m}_{i-1/2,j}(\xi^2_{i-1/2}-1)\frac{P^{n+1,m+1}_{g,i,j}+P^{n+1,m}_{t,i,j}-P^{n+1,m}_{g,i-1,j}-P^{n+1,m}_{t,i-1,j}}{\delta\xi_{i-1}}\right)\end{aligned}$$

where,

$$\left.\frac{BP_g}{\mu T}\right|_{i+1/2,j}^{n+1,m} = \frac{\delta\xi_{i^+}}{\delta\xi_i}\left(\frac{BP_g}{\mu T}\right)_{i,j} + \frac{\delta\xi_{i^-}}{\delta\xi_i}\left(\frac{BP_g}{\mu T}\right)_{i+1,j}$$

$$\left.\frac{BP_g}{\mu T}\right|_{i,j+1/2}^{n+1,m} = \frac{\delta\eta_{j^+}}{\delta\eta_j}\left(\frac{BP_g}{\mu T}\right)_{i,j} + \frac{\delta\eta_{j^-}}{\delta\eta_j}\left(\frac{BP_g}{\mu T}\right)_{i,j+1}$$

After rearrangement, the new time step gas partial pressure is obtained by the following equation.

$$\boxed{A_P P_{g,i,j}^{n+1,m+1} = A_W P_{g,i-1,j}^{n+1,m} + A_E P_{g,i+1,j}^{n+1,m} + A_S P_{g,i,j-1}^{n+1,m} + A_N P_{g,i,j+1}^{n+1,m+1} + F}$$

where,

$$A_P = A_W + A_E + A_S + A_N + \frac{\varepsilon_{i,j}^{n+1,m}}{\Delta t T_{i,j}^{n+1,m}}$$

$$A_W = J\frac{\xi_{i-1/2}^2 - 1}{\Delta\xi_i \delta\xi_{i-1}} \left.\frac{BP_g}{\mu T}\right|_{i-1/2,j}^{n+1,m}$$

$$A_E = J\frac{\xi_{i+1/2}^2 - 1}{\Delta\xi_i \delta\xi_i} \left.\frac{BP_g}{\mu T}\right|_{i+1/2,j}^{n+1,m}$$

$$A_S = J\frac{1 - \eta_{j-1/2}^2}{\Delta\eta_j \delta\eta_{j-1}} \left.\frac{BP_g}{\mu T}\right|_{i,j-1/2}^{n+1,m}$$

$$A_N = J\frac{1 - \eta_{j+1/2}^2}{\Delta\eta_j \delta\eta_j} \left.\frac{BP_g}{\mu T}\right|_{i,j+1/2}^{n+1,m}$$

$$\begin{aligned} F = {} & \frac{J}{\Delta\xi_i}\left(\left.\frac{BP_g}{\mu T}\right|_{i+1/2,j}^{n+1,m}(\xi_{i+1/2}^2 - 1)\frac{P_{t,i+1,j}^{n+1,m} - P_{t,i,j}^{n+1,m}}{\delta\xi_i} - \left.\frac{BP_g}{\mu T}\right|_{i-1/2,j}^{n+1,m}(\xi_{i-1/2}^2 - 1)\frac{P_{t,i,j}^{n+1,m} - P_{t,i-1,j}^{n+1,m}}{\delta\xi_{i-1}}\right) \\ & + \frac{J}{\Delta\eta_j}\left(\left.\frac{BP_g}{\mu T}\right|_{i,j+1/2}^{n+1,m}(1 - \eta_{j+1/2}^2)\frac{P_{t,i,j+1}^{n+1,m} - P_{t,i,j}^{n+1,m}}{\delta\eta_j} - \left.\frac{BP_g}{\mu T}\right|_{i,j-1/2}^{n+1,m}(1 - \eta_{j-1/2}^2)\frac{P_{t,i,j}^{n+1,m} - P_{t,i,j-1}^{n+1,m}}{\delta\eta_{j-1}}\right) \\ & + \frac{R}{M_g}S_g + \frac{\varepsilon_{i,j}^n}{\delta t T_{i,j}^n}P_{g,i,j}^n \end{aligned}$$

$$J = \frac{1}{f^2(\xi^2 - \eta^2)}$$

B.2.2.2 Tar

Similarly, discretize the above Equation B.8, and the new time step tar partial pressure is obtained by the following equation.

$$A_P P_{t,i,j}^{n+1,m+1} = A_W P_{t,i-1,j}^{n+1,m} + A_E P_{t,i+1,j}^{n+1,m} + A_S P_{t,i,j-1}^{n+1,m} + A_N P_{t,i,j+1}^{n+1,m+1} + F$$

where,

$$A_P = A_W + A_E + A_S + A_N + \frac{\varepsilon_{i,j}^{n+1,m}}{\Delta t T_{i,j}^{n+1,m}}$$

$$A_W = J\frac{\xi_{i-1/2}^2 - 1}{\Delta\xi_i \delta\xi_{i-1}} \left.\frac{BP_t}{\mu T}\right|_{i-1/2,j}^{n+1,m}$$

$$A_E = J\frac{\xi_{i+1/2}^2 - 1}{\Delta\xi_i \delta\xi_i} \left.\frac{BP_t}{\mu T}\right|_{i+1/2,j}^{n+1,m}$$

$$A_S = J\frac{1 - \eta_{j-1/2}^2}{\Delta\eta_j \delta\eta_{j-1}} \left.\frac{BP_t}{\mu T}\right|_{i,j-1/2}^{n+1,m}$$

$$A_N = J\frac{1 - \eta_{j+1/2}^2}{\Delta\eta_j \delta\eta_j} \left.\frac{BP_t}{\mu T}\right|_{i,j+1/2}^{n+1,m}$$

$$\begin{aligned} F = {} & \frac{J}{\Delta\xi_i}\left(\left.\frac{BP_t}{\mu T}\right|_{i+1/2,j}^{n+1,m}(\xi_{i+1/2}^2 - 1)\frac{P_{g,i+1,j}^{n+1,m} - P_{g,i,j}^{n+1,m}}{\delta\xi_i} - \left.\frac{BP_t}{\mu T}\right|_{i-1/2,j}^{n+1,m}(\xi_{i-1/2}^2 - 1)\frac{P_{g,i,j}^{n+1,m} - P_{g,i-1,j}^{n+1,m}}{\delta\xi_{i-1}}\right) \\ & + \frac{J}{\Delta\eta_j}\left(\left.\frac{BP_t}{\mu T}\right|_{i,j+1/2}^{n+1,m}(1 - \eta_{j+1/2}^2)\frac{P_{g,i,j+1}^{n+1,m} - P_{g,i,j}^{n+1,m}}{\delta\eta_j} - \left.\frac{BP_t}{\mu T}\right|_{i,j-1/2}^{n+1,m}(1 - \eta_{j-1/2}^2)\frac{P_{g,i,j}^{n+1,m} - P_{g,i,j-1}^{n+1,m}}{\delta\eta_{j-1}}\right) \\ & + \frac{R}{M_t}S_t + \frac{\varepsilon_{i,j}^n}{\delta t T_{i,j}^n}P_{t,i,j}^n \end{aligned}$$

$$J = \frac{1}{f^2(\xi^2 - \eta^2)}$$

B.2.3 Boundary Conditions

Use parabolic interpolation for boundary nodes. At the boundary of symmetry, we have

$$\phi_1 = \frac{\phi_2(dx_1 + dx_2)^2 - \phi_3(dx_1)^2}{2dx_1dx_2 + (dx_2)^2}$$

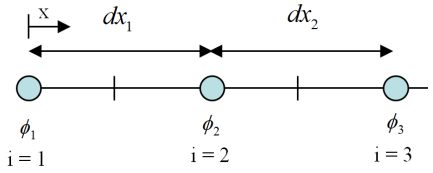

Figure B.2: Boundary nodes at the beginning of the grid.

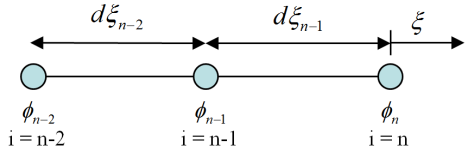

Figure B.3: Boundary nodes at the end of the grid.

For instance, for temperature at the plane of $\xi = 1$, we have

$$T_1 = \frac{T_2(d\xi_1 + d\xi_2)^2 - T_3(d\xi_1)^2}{2d\xi_1d\xi_2 + (d\xi_2)^2}$$

For the symmetric boundary at the end of grid, like Figure B.3, we have

$$\frac{\partial T}{\partial \xi} = -(T_{n-1} - T_n)\frac{d\xi_{n-2} + d\xi_{n-1}}{d\xi_{n-2}d\xi_{n-1}} + (T_{n-2} - T_n)\frac{d\xi_{n-1}}{(d\xi_{n-2} + d\xi_{n-1})d\xi_{n-2}}$$

Since$\frac{\partial T}{\partial \xi} = 0$ at the plane of symmetry, we have

$$T_n = \frac{T_{n-1}(d\xi_{n-1} + d\xi_{n-2})^2 - T_{n-2}d\xi_{n-2}^2}{2d\xi_{n-1}d\xi_{n-2} + d\xi_{n-2}^2}$$

For the boundary nodes at the surface, remember we have

$$\vec{\nabla} = \hat{e}_\xi \frac{(\xi^2-1)^{1/2}}{f(\xi^2-\eta^2)^{1/2}} \frac{\partial}{\partial \xi} + \hat{e}_\eta \frac{(1-\eta^2)^{1/2}}{f(\xi^2-\eta^2)^{1/2}} \frac{\partial}{\partial \eta} + \hat{e}_\phi \frac{1}{f(\xi^2-\eta^2)^{1/2}(1-\eta^2)^{1/2}} \frac{\partial}{\partial \phi}$$

Thus

$$\frac{\lambda}{f}\sqrt{\frac{\xi^2-1}{\xi^2-\eta^2}}\frac{\partial T}{\partial \xi} = \sigma\varepsilon(T_s^4 - T_n^4) + h(T_g - T_n)$$

Apply parabolic interpolation for surface nodes, we have

$$A = \frac{d\xi_{n-2} + d\xi_{n-1}}{d\xi_{n-2} d\xi_{n-1}}, \quad B = \frac{d\xi_{n-1}}{(d\xi_{n-2} + d\xi_{n-1}) d\xi_{n-2}}, \quad C = \frac{\lambda}{f}\sqrt{\frac{\xi^2-1}{\xi^2-\eta^2}}$$

And

$$T_n = \frac{1}{A-B}\left[\frac{1}{C}\left(\sigma\varepsilon(T_s^4 - T_n^4) + h(T_g - T_n)\right) + AT_{n-1} - BT_{n-2}\right]$$

Pressure at the surface nodes are calculated as follows,

$$\gamma = \frac{P_g(\xi_{n-1}, \eta, 2)}{P_g(\xi_{n-1}, \eta, 2) + P_t(\xi_{n-1}, \eta, 2)}$$

$$P_t(\xi_n) = P_0(1-\gamma), \qquad P_g(\xi_n) = P_0\gamma$$

APPENDIX C

Chemical Analysis

C.1 Detailed Chemistry of the Organic Phases in Bio-oil

The chemical compounds in the organic phases of the bio-oil were identified and quantified using GC-MS. Only the species with relative content larger than 0.35% were reported in Table C.1.

Table C.1: Major chemical compounds in the organic phase of the bio-oil as determined by GC/MS peak areas (%).

Compounds	Molecular formula	NC	400 °C	450 °C	500 °C	550 °C	600 °C	R1	R2	R3	R4
Aromatic Hydrocarbons											
Toluene	C7H8		0.835	1.265	2.475	3.47	2.65	1.995	1.995	2.15	1.55
Ethylbenzene	C8H10		0.425	0.565	0.875	0.72	0.435	0.665	0.7	0.71	0.63
o-Xylene	C8H10		2.725	3.675	6.04	5.72	3.96	4.745	4.865	4.915	4.355
o-Xylene	C8H10		0.92	1.18	1.98	2.01	1.625	1.43	1.52	1.63	1.385
Benzene, 1,2,4-trimethyl-	C9H12		0.445	0.47	0.505	0.385	0.505	0.39	0.425	0.42	0.45
Benzene, 1,2,3-trimethyl-	C9H12		1.355	1.185	1.155	0.79	0.215	1.09	1.03	0.995	0.86
Mesitylene	C9H12		1.895	2.02	2.845	2.32	1.77	2.395	2.24	2.63	2.13
Benzene, 1-ethenyl-2-methyl-	C9H10		0.445	0.415	0.655	0.855	0.805	0.55	0.58	0.56	0.59
Indane	C9H10		1.375	1.7	2.36	2.02	1.505	2.08	2.04	2.07	2.08
Indene	C9H8		1.75	1.985	3.235	4.725	5.77	2.625	2.9	2.69	2.95
3-Phenylbut-1-ene	C10H12		0.905	0.855	0.9	0.82	0.705	0.845	0.83	0.775	0.735
p-Cymene	C10H14		0.55	0.45	0.26	0.24		0.325	0.33	0.265	0.305
Indan, 1-methyl-	C10H12		1.34	1.395	1.52	1.27	0.97	1.42	1.39	1.325	1.37
Benzene, 1-butynyl-	C10H10		1.23	1.025	1.85	2.4	2.7	1.42	1.41	1.625	1.71
Azulene	C10H8		1.935	1.65	2.435	3.395	5.295	2.46	2.33	2.225	2.505
PAH											
Naphthalene, 1,2-dihydro-6-methyl-	C11H12		1.205	1.31	1.495	1.275	1.33	1.315	1.44	1.375	1.395
Naphthalene, 2-methyl-	C11H10		1.71	2.365	3.6	5.035	6.815	3.31	3.595	3.605	3.795
Naphthalene, 1-methyl-	C11H10				0.425	0.61	0.995				
Naphthalene, 2-ethyl-	C12H12		0.605	0.565	0.505	0.59	0.47	0.53	0.48	0.79	0.595
Naphthalene, 2,3-dimethyl-	C12H12		1.125	0.82	2.145	0.985	1.005	1.355	0.94	2.075	1.91
Naphthalene, 2,3-dimethyl-	C12H12		0.885	1.025		1.185	1.35	1.07	1.1	0.81	0.34

Continue on the next page

Table C.1 – continued

Compounds	Molecular formula	NC	400 °C	450 °C	500 °C	550 °C	600 °C	R1	R2	R3	R4
Naphthalene, 1,3-dimethyl-	C12H12					0.38	0.495			0.25	
Phenols											
Phenol	C6H6O	1.2	2.605	3.535	4.725	6.85	8.01	4.625	5.465	4.975	5.505
Phenol, 2-methyl-	C7H8O	0.83	2.14	2.785	3.71	4.285	4.67	3.445	3.865	3.645	3.69
Phenol, 3-methyl-	C7H8O	1.3	3.055	4.05	5.585	6.865	7.89	5.03	5.715	5.41	5.405
Phenol, 2-methoxy-	C7H8O2	4.48	3.31	2.905	2.305	1.41	1	2.5	2.57	2.32	2.07
Phenol, 2,5-dimethyl-	C8H10O	0.705	1.33	1.345	1.89	1.72	1.85	1.655	1.585	1.605	1.675
Phenol, 2,6-dimethyl-	C8H10O		3.04	3.82	6.2	5.86	6.085	4.745	5.1	5.255	5.23
Phenol, 2,3-dimethyl-	C8H10O		0.285	0.35	0.44	0.46	0.56	0.5	0.52	0.475	0.51
Phenol, 2,6-dimethyl-	C8H10O2	0.35	0.575	0.505	0.68	0.38	0.475	0.675	0.52	0.75	0.8
Creosol	C8H10O2	8.205	6.205	5.6	4.355	3.4	1.825	5.065	5.29	5.36	4.74
Catechol	C6H6O2	0.33	2.53	2.62	1.44	0.76	1.135	2.275	1.705	1.43	1.935
Phenol, 2,3,6-trimethyl-	C9H12O		0.5	0.51	0.55	0.36	0.26	0.605	0.415	0.535	0.42
1,2-Benzenediol, 3-methyl-	C7H8O2		1.585	1.645	0.455	0.525	0.78	1.465	0.96	0.655	1.04
Phenol, 2,4,5-trimethyl-	C9H12O		0.59	0.45	0.39	0.425	0.41	0.46	0.44	0.47	0.715
Phenol, 4-ethyl-2-methoxy-	C9H12O2	2.51	2.685	2.41	1.81	1.38	0.78	2.045	2.15	2.195	1.905
1,2-Benzenediol, 4-methyl-	C7H8O2		1.84	1.885	0.515	0.415	1.01	1.505	0.825	1.005	1.19
2-Methoxy-4-vinylphenol	C9H10O2	2.485	1.55	1.39	1.13	1.015	0.635	1.25	1.145	1.69	1.425
Phenol, 4-allyl-2-methoxy-	C12H14O3	1.005									
1,3-Benzenediol, 4,5-dimethyl-	C8H12O2		0.935	0.955	0.355	0.255	0.46	0.875	0.39	0.485	0.575
Phenol, 2-methoxy-3-(2-propenyl)-	C10H12O2	0.37	0.63	0.545	0.445	0.35	0.215	0.5	0.525	0.57	0.445
1H-Indenol	C9H8O		0.78	1.065	1.315	1.285	1.255	1.16	1.2	1.37	1.21
Phenol, 2-methoxy-4-propyl-	C10H14O2	0.625	0.74	0.67	0.54	0.41	0.265	0.62	0.61	0.59	0.515
4-Ethylcatechol	C8H10O2		0.97	0.92	0.24	0.17	0.505	0.735	0.305	0.415	0.49
Phenol, 2-methoxy-4-(1-propenyl)-	C10H12O2	0.625									
Phenol, 2-methoxy-5-propenyl-, (E)-	C10H12O2		0.81	0.745	0.49	0.485		0.645	0.55	0.68	0.55

Continue on the next page

Table C.1 – continued

Compounds	Molecular formula	NC	400 °C	450 °C	500 °C	550 °C	600 °C	R1	R2	R3	R4
Phenol, 2-methoxy-4-(1-propenyl)-	C10H12O2	3.825	2.46	2.245	1.745	1.4	0.84	1.985	2.06	2.055	1.23
2-Hydroxy-6-methoxyacetophenone	C9H10O3	0.54	0.515	0.51	0.37	0.27		0.4	0.41	0.415	0.48
4-Hydroxy-3-methoxyphenylacetone	C10H12O3	0.72									
Coniferaldehyde	C10H10O3	0.91									
Ketones											
Methyl vinyl ketone	C4H6O	1.45	2.115	2.275	1.605	1.27	1.26	1.815	2.03	1.495	1.73
2-Butanone	C4H8O	0.84	1.1	1.115	0.965	0.49		1.055	1.105	0.85	1.05
2-Propanone, 1-hydroxy-	C3H6O2	6.705	1.625	1.165				0.56	0.4	0.27	0.35
3-Buten-2-one	C4H6O	0.71	0.635	0.59	0.415	0.37		0.475	0.495	0.41	0.365
N-Methoxy-N-methylacetamide	C4H9NO2	2.42	1.015	0.68	0.205			0.415	0.4	0.275	0.365
Succindialdehyde	C4H6O2	0.615									
Acetic anhydride	C4H6O3	4.295									
2-Cyclopenten-1-one	C5H6O	4.535	3.55	3.315	2.18	1.485	1.07	2.415	2.9	2.26	2.385
2-Propanone, 1-(acetyloxy)-	C5H8O3	2									
2-Cyclopenten-1-one, 2-methyl-	C6H8O	0.655	0.845	0.995	0.825	0.45	0.32	0.725	0.9	0.86	0.795
2-Cyclopenten-1-one, 2-hydroxy-	C6H8O2	2.82	1.385	1	0.29			0.43	0.45	0.37	0.33
Cyclotene	C6H8O2	2.225	1.74	1.345	0.745	0.715	0.615	1.07	1.01	1.02	0.945
2-Cyclopenten-1-one, 2,3-dimethyl-	C7H10O		0.465	0.45	0.38	0.32	0.31	0.37	0.4	0.37	0.37
Propane, 2,2-dimethoxy-	C5H12O2	0.25	0.49	0.505							0.515
Acids											
Acetic acid	C2H4O2	8.57	4.645	2.765	0.395			1.005	0.655	0.315	0.485
4-Pentenoic acid	C5H8O2	0.31									
4-Hydroxy-2-methoxybenaldehyde	C8H8O3	0.57									
Furans											
2-furanmethanol	C5H6O2	2.75									
2(5H)-Furanone	C4H4O2	2.525									

Continue on the next page

Table C.1 – continued

Compounds	Molecular formula	NC	400 °C	450 °C	500 °C	550 °C	600 °C	R1	R2	R3	R4
Furan, 2,5-dihydro-2,5-dimethyl-	C6H10O3	0.495									
2-Furancarboxaldehyde, 5-methyl-	C6H6O2	2.01									
2(5H)-Furanone, 3-methyl-	C5H6O2	0.54									
Benzofuran	C8H6O		0.54	0.455	0.65	0.83	1.015	0.63	0.655	0.595	0.645
2-Furanone, 2,5-dihydro-3,5-dimethyl	C6H8O2	0.465									
4-Methyl-5H-furan-2-one	C5H6O2	0.635									
Benzofuran, 7-methyl-	C9H8O		0.33	0.34	0.445	0.4	0.47	0.365	0.415	0.385	0.345
Benzofuran, 2-methyl-	C9H8O		1.05	1.17	1.33	1.27	1.52	1.315	1.405	1.285	1.28
Benzofuran, 4,7-dimethyl-	C10H10O		0.715	0.755	0.835	0.69	0.635	0.82	0.755	0.785	0.805
5-Hydroxymethylfurfural	C6H6O3	1.18									
Esters											
Propanoic acid, propyl ester	C6H12O2	0.57									
Acetic acid, methyl ester	C3H6O2	1.695									
Carbonocyanidic acid, ethyl ester	C4H5NO2	0.64									
Carbamic acid, phenyl ester	C7H7NO2		0.96	0.81	0.845	0.48	0.305	0.63	0.755	0.82	0.725
2-Butanone, 1-(acetyloxy)-	C6H10O3	1.185									
Others											
2-Butene, 1,1-dimethoxy-	C6H12O2	0.37	1.045	0.84	0.36			0.445			0.485
3-Aminopyrazine 1-oxide	C4H5N3O	0.575									
4(1H)-Pyrimidinone, 6-methyl-	C5H6NO2		0.94	0.825	0.76	0.405	0.3	0.645	0.735	0.705	0.635
Cyclopropyl carbinol	C5H6O2	1.39									
Maltol	C6H6O3	0.285									
6-Methyl-1,4-dioxaspiro[2.4]heptan-5-one	C6H8O3	0.96									
1-Naphthalenol	C10H8O		0.885	1.1	1.17	1.35	1.415	1.065	1.09	1.185	1.135
7-Methyl-1-naphthol	C11H10O		0.34	0.41	0.465	0.535	0.485	0.405	0.435	0.4	0.515

BIBLIOGRAPHY

BIBLIOGRAPHY

[1] RB Gupta and A Demirbas. *Gasoline, diesel and ethanol from grasses and plants*. Cambridge (UK): Cambridge University Press, 2010.

[2] World Nuclear Association. *World Nuclear Performance Report 2017*. 2017.

[3] U.S. Energy Information Administration. *Monthly Energy Review*. April 2017, Table 2.1.

[4] George W Huber. *Breaking the chemical and engineering barriers to lignocellulosic biofuels: next generation hydrocarbon biorefineries*. 2008.

[5] Robert D Perlack et al. *US billion-ton update: biomass supply for a bioenergy and bioproducts industry*. 2011.

[6] Dinesh Mohan, Charles U Pittman, and Philip H Steele. "Pyrolysis of wood/biomass for bio-oil: a critical review". *Energy & fuels* 20.3 (2006), pp. 848–889.

[7] Alex D Paulsen, Matthew S Mettler, and Paul J Dauenhauer. "The role of sample dimension and temperature in cellulose pyrolysis". *Energy & Fuels* 27.4 (2013), pp. 2126–2134.

[8] Michele Corbetta et al. "Pyrolysis of centimeter-scale woody biomass particles: Kinetic modeling and experimental validation". *Energy & Fuels* 28.6 (2014), pp. 3884–3898.

[9] Phillip C Badger and Peter Fransham. "Use of mobile fast pyrolysis plants to densify biomass and reduce biomass handling costs—A preliminary assessment". *Biomass and bioenergy* 30.4 (2006), pp. 321–325.

[10] AV Bridgwater and GVC Peacocke. "Fast pyrolysis processes for biomass". *Renewable and sustainable energy reviews* 4.1 (2000), pp. 1–73.

[11] Mohammad I Jahirul et al. "Biofuels production through biomass pyrolysis—a technological review". *Energies* 5.12 (2012), pp. 4952–5001.

[12] Jun Shen et al. "Effects of particle size on the fast pyrolysis of oil mallee woody biomass". *Fuel* 88.10 (2009), pp. 1810–1817.

[13] C Di Blasi et al. "Effects of particle size and density on the packed-bed pyrolysis of wood". *Energy & Fuels* 27.11 (2013), pp. 6781–6791.

[14] JM Encinar et al. "Pyrolysis of two agricultural residues: olive and grape bagasse. Influence of particle size and temperature". *Biomass and Bioenergy* 11.5 (1996), pp. 397–409.

[15] Hong Lu et al. "Effects of particle shape and size on devolatilization of biomass particle". *Fuel* 89.5 (2010), pp. 1156–1168.

[16] Pious O Okekunle et al. "Effect of biomass size and aspect ratio on intra-particle tar decomposition during wood cylinder pyrolysis". *Journal of Thermal Science and Technology* 7.1 (2012), pp. 1–15.

[17] AMC Janse, RWJ Westerhout, and W Prins. "Modelling of flash pyrolysis of a single wood particle". *Chemical Engineering and Processing: Process Intensification* 39.3 (2000), pp. 239–252.

[18] S Şensöz, D Angın, and S Yorgun. "Influence of particle size on the pyrolysis of rapeseed (Brassica napus L.): fuel properties of bio-oil". *Biomass and Bioenergy* 19.4 (2000), pp. 271–279.

[19] L Aguiar et al. "Influence of temperature and particle size on the fixed bed pyrolysis of orange peel residues". *Journal of Analytical and Applied Pyrolysis* 83.1 (2008), pp. 124–130.

[20] Howard R Baum and Arvind Atreya. "A Model for Combustion of Firebrands of Various Shapes". *Fire Safety Science* 11 (2014), pp. 1353–1367.

[21] JEF Carmo and AGB Lima. "Mass transfer inside oblate spheroidal solids: modelling and simulation". *Brazilian Journal of Chemical Engineering* 25.1 (2008), pp. 19–26.

[22] Kai-Yuan Li et al. "Pyrolysis of medium-density fiberboard: optimized search for kinetics scheme and parameters via a genetic algorithm driven by Kissinger's method". *Energy & Fuels* 28.9 (2014), pp. 6130–6139.

[23] BM Wagenaar, W Prins, and WPM Van Swaaij. "Flash pyrolysis kinetics of pine wood". *Fuel processing technology* 36.1-3 (1993), pp. 291–298.

[24] Antonio Galgano and Colomba Di Blasi. "Modeling wood degradation by the unreacted-core-shrinking approximation". *Industrial & Engineering Chemistry Research* 42.10 (2003), pp. 2101–2111.

[25] Colomba Di Blasi. "Modeling chemical and physical processes of wood and biomass pyrolysis". *Progress in Energy and Combustion Science* 34.1 (2008), pp. 47–90.

[26] Won Chan Park, Arvind Atreya, and Howard R Baum. "Experimental and theoretical investigation of heat and mass transfer processes during wood pyrolysis". *Combustion and Flame* 157.3 (2010), pp. 481–494.

[27] Morten Willatzen, Lew Yan Voon, and C Lok. "Prolate Spheroidal Coordinates". *Separable Boundary-Value Problems in Physics* (2011), pp. 139–154.

[28] Morten G Grønli and Morten C Melaaen. "Mathematical model for wood pyrolysis comparison of experimental measurements with model predictions". *Energy & Fuels* 14.4 (2000), pp. 791–800.

[29] Arvind Atreya et al. "The effect of size, shape and pyrolysis conditions on the thermal decomposition of wood particles and firebrands". *International Journal of Heat and Mass Transfer* 107 (2017), pp. 319–328.

[30] James P Diebold. *A review of the chemical and physical mechanisms of the storage stability of fast pyrolysis bio-oils*. Tech. rep. National Renewable Energy Lab., Golden, CO (US), 1999.

[31] Qi Zhang et al. "Upgrading bio-oil over different solid catalysts". *Energy & Fuels* 20.6 (2006), pp. 2717–2720.

[32] Wei-Hsin Chen and Po-Chih Kuo. "Torrefaction and co-torrefaction characterization of hemicellulose, cellulose and lignin as well as torrefaction of some basic constituents in biomass". *Energy* 36.2 (2011), pp. 803–811.

[33] Wei-Hsin Chen and Po-Chih Kuo. "A study on torrefaction of various biomass materials and its impact on lignocellulosic structure simulated by a thermogravimetry". *Energy* 35.6 (2010), pp. 2580–2586.

[34] Mark J Prins, Krzysztof J Ptasinski, and Frans JJG Janssen. "Torrefaction of wood: Part 1. Weight loss kinetics". *Journal of analytical and applied pyrolysis* 77.1 (2006), pp. 28–34.

[35] J Prins Mark, KJ Ptasinski, and FJJG Janssen. "Torrefaction of wood Part 2. Analysis of products J". *Anal. Appl. Pyrolysis* 77 (2006), pp. 35–40.

[36] Carole Couhert, Sylvain Salvador, and Jean-Michel Commandre. "Impact of torrefaction on syngas production from wood". *Fuel* 88.11 (2009), pp. 2286–2290.

[37] MJC Van der Stelt et al. "Biomass upgrading by torrefaction for the production of biofuels: A review". *Biomass and bioenergy* 35.9 (2011), pp. 3748–3762.

[38] Mohammed Hakkou et al. "Investigations of the reasons for fungal durability of heat-treated beech wood". *Polymer degradation and stability* 91.2 (2006), pp. 393–397.

[39] B Arias et al. "Influence of torrefaction on the grindability and reactivity of woody biomass". *Fuel Processing Technology* 89.2 (2008), pp. 169–175.

[40] Manunya Phanphanich and Sudhagar Mani. "Impact of torrefaction on the grindability and fuel characteristics of forest biomass". *Bioresource technology* 102.2 (2011), pp. 1246–1253.

[41] Jiajia Meng et al. "The effect of torrefaction on the chemistry of fast-pyrolysis bio-oil". *Bioresource technology* 111 (2012), pp. 439–446.

[42] Shoujie Ren et al. "The effects of torrefaction on compositions of bio-oil and syngas from biomass pyrolysis by microwave heating". *Bioresource technology* 135 (2013), pp. 659–664.

[43] Shi-Shen Liaw et al. "Effect of pretreatment temperature on the yield and properties of bio-oils obtained from the auger pyrolysis of Douglas fir wood". *Fuel* 103 (2013), pp. 672–682.

[44] AA Boateng and CA Mullen. "Fast pyrolysis of biomass thermally pretreated by torrefaction". *Journal of Analytical and Applied Pyrolysis* 100 (2013), pp. 95–102.

[45] National Insititute of Standards and Technology (NIST). "The NIST 11 Mass Spectral Library" (2011).

[46] Sheng Chang et al. "Characterization of products from torrefaction of sprucewood and bagasse in an auger reactor". *Energy & Fuels* 26.11 (2012), pp. 7009–7017.

[47] Guillaume Gauthier et al. "Pyrolysis of centimetre-scale wood particles: New experimental developments and results". *Journal of Analytical and Applied Pyrolysis* 104 (2013), pp. 521–530.

[48] Lucia Basile et al. "Thermal effects during biomass pyrolysis". *Thermochimica Acta* 636 (2016), pp. 63–70.

[49] Lars PH Jeurgens, Zumin Wang, and Eric J Mittemeijer. "Thermodynamics of reactions and phase transformations at interfaces and surfaces". *International Journal of Materials Research* 100.10 (2009), pp. 1281–1307.

[50] G Foti. "Silicon carbide: from amorphous to crystalline material". *Applied Surface Science* 184.1 (2001), pp. 20–26.

[51] Hsiang-Cheng Kung and Ashok S Kalelkar. "On the heat of reaction in wood pyrolysis". *Combustion and flame* 20.1 (1973), pp. 91–103.

[52] Won Chan Park. *A study of pyrolysis of charring materials and its application to fire safety and biomass utilization*. University of Michigan, 2008.

[53] Peter Mølgaard Mortensen et al. "A review of catalytic upgrading of bio-oil to engine fuels". *Applied Catalysis A: General* 407.1-2 (2011), pp. 1–19.

[54] Theodore Dickerson and Juan Soria. "Catalytic fast pyrolysis: a review". *Energies* 6.1 (2013), pp. 514–538.

[55] Yinbin Huang et al. "Converting pine sawdust to advanced biofuel over HZSM-5 using a two-stage catalytic pyrolysis reactor". *Journal of Analytical and Applied Pyrolysis* 111 (2015), pp. 148–155.

[56] Pranjali D Muley et al. "Pyrolysis and Catalytic Upgrading of Pinewood Sawdust Using an Induction Heating Reactor". *Energy & Fuels* 29.11 (2015), pp. 7375–7385.

[57] Paul T Williams and Nittaya Nugranad. "Comparison of products from the pyrolysis and catalytic pyrolysis of rice husks". *Energy* 25.6 (2000), pp. 493–513.

[58] Güray Yildiz et al. "Catalytic fast pyrolysis of pine wood: effect of successive catalyst regeneration". *Energy & fuels* 28.7 (2014), pp. 4560–4572.

[59] SD Stefanidis et al. "In-situ upgrading of biomass pyrolysis vapors: catalyst screening on a fixed bed reactor". *Bioresource technology* 102.17 (2011), pp. 8261–8267.

[60] Ersan Pütün. "Catalytic pyrolysis of biomass: Effects of pyrolysis temperature, sweeping gas flow rate and MgO catalyst". *Energy* 35.7 (2010), pp. 2761–2766.

[61] Jun Tao et al. "Catalytic cracking of biomass high-temperature pyrolysis tar using NiO/AC catalysts". *International journal of green energy* 12.8 (2015), pp. 773–779.

[62] M Auta, LM Ern, and BH Hameed. "Fixed-bed catalytic and non-catalytic empty fruit bunch biomass pyrolysis". *Journal of Analytical and Applied Pyrolysis* 107 (2014), pp. 67–72.

[63] M Azuara et al. "Catalytic post-treatment of the vapors from sewage sludge pyrolysis by means of γ-Al2O3: Effect on the liquid product properties". *Fuel Processing Technology* 130 (2015), pp. 252–262.

[64] Leiyu Zhou et al. "Catalytic pyrolysis of rice husk by mixing with zinc oxide: characterization of bio-oil and its rheological behavior". *Fuel processing technology* 106 (2013), pp. 385–391.

[65] A Veses et al. "Catalytic pyrolysis of wood biomass in an auger reactor using calcium-based catalysts". *Bioresource technology* 162 (2014), pp. 250–258.

[66] Eleni F Iliopoulou et al. "Catalytic upgrading of biomass pyrolysis vapors using transition metal-modified ZSM-5 zeolite". *Applied Catalysis B: Environmental* 127 (2012), pp. 281–290.

[67] Michaël Becidan, Øyvind Skreiberg, and Johan E Hustad. "Products distribution and gas release in pyrolysis of thermally thick biomass residues samples". *Journal of Analytical and Applied Pyrolysis* 78.1 (2007), pp. 207–213.

[68] Yoshio Ono. "Transformation of lower alkanes into aromatic hydrocarbons over ZSM-5 zeolites". *Catalysis Reviews* 34.3 (1992), pp. 179–226.

[69] NY Chen, DE Walsh, and LR Koenig. "Fluidized-Bed upgrading of wood pyrolysis liquids and related compounds". ACS Publications, 1988.

[70] Karen Sanctucci and Binita Shah. "Association of naphthalene with acute hemolytic anemia". *Academic Emergency Medicine* 7.1 (2000), pp. 42–47.

[71] Tan Shun et al. "Recent progress of catalytic pyrolysis of biomass by HZSM-5". *Chinese Journal of Catalysis* 34.4 (2013), pp. 641–650.

[72] Eleni Antonakou et al. "Evaluation of various types of Al-MCM-41 materials as catalysts in biomass pyrolysis for the production of bio-fuels and chemicals". *Fuel* 85.14-15 (2006), pp. 2202–2212.

[73] Ana G Gayubo et al. "Attenuation of catalyst deactivation by cofeeding methanol for enhancing the valorisation of crude bio-oil". *Energy & Fuels* 23.8 (2009), pp. 4129–4136.

[74] Maria A Peralta et al. "Deoxygenation of benzaldehyde over CsNaX zeolites". *Journal of Molecular Catalysis A: Chemical* 312.1-2 (2009), pp. 78–86.

[75] Xinli Zhu, Richard G Mallinson, and Daniel E Resasco. "Role of transalkylation reactions in the conversion of anisole over HZSM-5". *Applied Catalysis A: General* 379.1-2 (2010), pp. 172–181.

[76] Patrick A Horne, Nittaya Nugranad, and Paul T Williams. "Catalytic coprocessing of biomass-derived pyrolysis vapours and methanol". *Journal of analytical and applied pyrolysis* 34.1 (1995), pp. 87–108.

[77] VI Sharypov et al. "Co-pyrolysis of wood biomass and synthetic polymers mixtures: Part IV: Catalytic pyrolysis of pine wood and polyolefinic polymers mixtures in hydrogen atmosphere". *Journal of analytical and applied pyrolysis* 76.1-2 (2006), pp. 265–270.

[78] John D Adjaye and NN Bakhshi. "Catalytic conversion of a biomass-derived oil to fuels and chemicals II: Chemical kinetics, parameter estimation and model predictions". *Biomass and Bioenergy* 8.4 (1995), pp. 265–277.